

The finite operator model for step index fibres

Das Soumitra Kumar

Supervisors: Stephen C Creagh, Slawomir Sujecki, Trevor M Benson

Thesis submitted to the University of Nottingham for the degree of Doctor of Philosophy, November 2018.

Abstract

A ray-based dynamical model is developed to propagate light in passive optical fibres. The developed model provides an efficient way to investigate light propagation in the presence of boundary deformations in optical fibre waveguides using concepts of ray billiards and wave-chaos theory. The light propagation is modelled using the phase space transport, where the phase space method is a standard tool of tracing rays in enclosed cross-sectional boundaries. In the developed model, the light propagation is achieved using coarse-grained phase spaces and Ulam's method is adopted for the numerical discretisation. The phase space is divided into rectangular regions or pixels, and a bundle of rays are traced as ensembles from one pixel to the next. The coarse-graining transforms the process of tracing individual light trajectories into a probabilistic way of mapping power from one region of the phase space to another. On this basis, a finite operator model, a form of Frobenius-Perron operator, is developed to propagate light in 3D fibres. The finite operator deterministically distributes power in the pixelated phase space.

The aim of this work is to investigate chaotic and regular ray propagation deformed optical fibres primarily for applications in mid-infrared (MIR) photonics using MIR transparent glasses. However, the model developed here is generally applicable to any deformed unstructured and step-index fibres. The finite operator method enables the calculation of the net accumulation of power in the core in the step index fibres due to the propagation of any arbitrary input light distributions. Using the model, it is possible to investigate the variation of the accumulated power in the core with the variations in any structural deformations of the fibre, variations in the refractive indices of core and cladding media, and the variations in any input light distribution. The study sheds light on ways in which pump power absorption in rare-earth (RE) doped active fibres can be improved. In this thesis, the investigation is carried out to find ways of improving the captured power in an undoped core in passive fibres, and the variations in the propagation mechanisms are characterised from a given input light distribution by varying the structural features of the step index fibre. On the basis of the results, the future extension of the method to study pump power absorption in active fibres is briefly discussed. The finite operator method overcomes previous limitations of light propagation models in asymmetric optical fibres.

Acknowledgements

I am tremendously grateful to everyone who provided me the opportunity to undertake this PhD and allowed it to come to fruition. First, and foremost, I would like to express my sincerest gratitude to my supervisor Dr Stephen Creagh for his continued support of my research, and for his patience and enthusiasm. Thank you for the knowledge and insight you provided me over the years without which the completion of this work would not have been possible. I would then like to thank my main supervisor, Professor Trevor Benson for his tireless support in the preparation of my publications and thesis. Professor Benson has been very kind and supportive during the difficult times, and suggested valuable improvements to the work which provided much needed clarity and scholarship. I would also like to thank Dr Slawomir Sujecki for inspiring me into this project.

Next, I would like to thank my fellow researchers in the GGIEMR for all the wonderful experiences and making my time here very memorable. Thank you Zhang Zhewen (Edward) for the late evening conversations, Latifa Abdul Aziz for inspiring me to be more active, Ahmed Elkalsh for always taking it upon yourself to put together socialising events, Xuesong Meng (Vicky) for being so caring, Daniel Simmons for inspiring me to be more organised, and Sendy Phang for being so much fun and lively. I would also thank all the new-comers during my time to the group including Nazri, Joju, and Luke. You have all been such a splendid company.

I would like to thank my mum and dad for their unwavering support, without which arriving at this juncture in my life would have been unimaginable. I owe my dad an unpayable debt for all the life lessons he taught me, and my mum's undying love and warmth for me has kept me on track throughout all the challenging times.

I am also eternally grateful to my partner, Priyanka, who has been so compassionate and understanding during my years as a PhD student. Thank you for all your love and support; I am extremely fortunate to have you by my side.

Lastly, I would like to acknowledge, with thanks, the financial support of my PhD studies received from the Faculty of Engineering (Deans Scholarship) and School of Mathematical Sciences, University of Nottingham, UK.

List of publications

Journal

[1] D. S. Kumar, S.C. Creagh, S. Sujecki, and T. M. Benson, 'Modeling propagation in deformed step-index fiber using the finite operator method', **accepted for publication in JOSA-B**.

Conference papers

[1] D. S. Kumar, S. C. Creagh, S. Sujecki, and T. M. Benson, 'The effects of deformation in large step index optical fibres', International Conference on Transparent Optical Networks (ICTON), July,2018, Bucharest, Romania.

[2] D. S. Kumar, S. C. Creagh, S. Sujecki, and T. M. Benson, 'Modelling capture of pump power in the core using deformed step index fibre', Optical Wave and waveguide Theory and Numerical Modelling (OWTNM), April 2018, Germany.

[3] D. S. Kumar, S. C. Creagh, S. Sujecki, and T. M. Benson, 'Modelling chaos in asymmetric optical fibres', International Conference on Transparent Optical Networks (ICTON), July 2017, Girona, Spain.

List of symbols

- f_0 = an initial light distribution in the phase space
- $\bar{f}_0$ = an initial light distribution in the Laplace domain
- f_m = a light distribution in the m^{th} reflection
- $\bar{f}_m$ = a light distribution in the m^{th} reflection in the Laplace domain
- $g(s, p, z)$ = a function that transforms the 3D coordinates after one reflection
- $h(s, p)$ = a function that transforms the 2D coordinates in the phase space after one reflection
- I_j = the intensity in the j^{th} pixel
- l_{2D} = distance traversed by a ray in a 2D cross-sectional plane of the fibre after 1 reflection
- m = reflection number
- M = total number of reflections
- $\hat{n}$ = a unit vector in the direction normal to the boundary
- n_i = refractive index of an incident medium i
- n_t = refractive index of a transmitted medium t
- n_c = refractive index of the core
- n_{cl} = refractive index of the cladding
- N = number of pixels along horizontal and vertical axes of the phase space of an unstructured fibre. In the case of the step index fibre, it is the number of pixels along an axis in the phase space for the cladding boundary.
- N_e = number of pixels along an axis in the core exterior phase space of the step index fibre.

- N_i = number of pixels along an axis in the core interior phase space of the step index fibre.
- p = momentum of a ray at the point where the ray hits the fibre boundary
- p_x = component of the ray momentum along the x-axis
- p_y = component of the ray momentum along the y-axis
- p_z = component of the ray momentum along the z-axis
- $\hat{\mathbf{p}}$ = a unit vector in the direction of the 2D cross-sectional component of a 3D ray
- $\bar{\mathbf{p}}_\mathbf{i}$ = direction vector of a 3D ray in a medium with refractive index n_i
- $\mathbf{p_i}$ = direction vector of the 2D cross-sectional component of a ray in a medium with refractive index n_i
- $\bar{p}_{\text{clad}}$ = momentum of a 3D ray in the cladding medium
- $\bar{p}_{\text{core}}$ = momentum of a 3D ray in the core medium
- p_{clad} = momentum of a 2D ray in the cladding medium
- p_{core} = momentum of a 2D ray in the core medium
- r = scaling factor for the boundary
- r_{TE} = Fresnel's reflection coefficient for TE polarisation
- R_{TE} = Fresnel's reflectance at the core-cladding dielectric boundary for TE polarisation
- $\mathcal{R}$ = reflection and transmission matrix at the boundaries of the fibre
- s = position defined by the arc length at the boundary
- s_{max} = circumference of the boundary of the unstructured fibre; in the case of the step index fibre, it is the circumference of the cladding boundary
- s_{core} = position defined by the arc length in the core boundary
- $S_r(\phi)$ = radius of the boundary

- t_{ij} = the mapping probability of power from pixel j to pixel i
- $\hat{t}$ = a unit vector in the direction tangential to the boundary
- T_{TE} = Transmittance for TE polarisation
- T_{2D} = 2D finite operator for a light distribution in the phase space
- $\bar{T}_{2D}$ = 2D finite operator in the Laplace domain
- T_{3D} = 3D finite operator for light distribution in the fibre
- $\bar{T}_{3D}$ = 3D finite operator in the Laplace domain
- $\bar{T}_{\beta}$ = the finite operator for the simplified toy model in the Laplace domain.
- $\bar{T}_{tr}$ = a 2D transport operator in the Laplace domain in the phase space for transferring (s, p) coordinates
- $w(s, \bar{p}_i)$ = a weighting function at the core boundaries of the fibre
- $\hat{z}$ = unit vector along the axial direction of the fibre
- Δz = distance of propagation of a ray along axial direction the fibre after each reflection.
- ϕ = polar angle from the origin
- ϵ = degree of deformation in the boundary
- χ = angle between $\hat{\mathbf{p}}$ and the unit vector $\hat{n}$
- θ = angle of the ray direction vector with the axial direction of the fibre
- $\varphi(s, p)$ = a 2D phase space transformation after one reflection
- β = a variable in the Laplace domain corresponding to z
- $\mu(I_j)$ = the power in the j^{th} pixel
- $\rho(x, y, p_x, p_y)$ = a light distribution at the input face of the fibre
- $\sigma_{x,y}$ = variance of a Gaussian distribution along x or y direction at the input face of the fibre

- Φ_{2D} = the net transfer of flux in the core in 2D as $M \to \infty$ reflections in the step index fibre.
- Φ_{3D} = the net transfer of flux in the core in 3D as $M \to \infty$.
- $\bar{\Phi}_{3D}^{M}$ = the net power accumulation in the core in 3D after M reflections

Glossary

- 2D two dimensional
- 3D three dimensional
- ARC Asymmetric resonant cavity
- IC Invariant curve
- MIR Mid-infrared
- NA Numerical aperture
- PL Photoluminescence
- RT Ray tracing
- SIF Step index fibre
- SOS Surface of section
- TIR Total internal reflection
- WG Whispering gallery

Contents

Abstract **i**

Acknowledgements **iii**

List of publications **iii**

List of symbols **v**

Glossary **ix**

1 Overview **1**

1.1 Introduction 1

1.2 Aims and Objectives 3

1.3 Thesis layout 3

2 Background **7**

2.1 Introduction 7

2.2 Mid-infrared photonics 8

2.3 Chaotic ray dynamics 10

2.3.1 Chaos analysis in deformed optical microcavities 12

2.3.2 Chaos analysis in deformed optical fibres 12

2.4 Operators of the Frobenius-Perron type 14

2.5 Chapter summary 15

3 Ray-tracing in mixed phase spaces 17

3.1 Introduction 17

3.2 Investigation of phase space patterns 20

3.2.1 Relationship between s and ϕ for the quadrupolar equation 21

3.2.2 The phase space of a circular boundary 22

3.2.3 Phase space with 5% deformation 24

3.2.4 Phase space with 12% deformation 28

3.2.5 Variation of the phase space with the boundary deformation 29

3.3 Chapter summary 31

4 The finite operator model 33

4.1 Introduction 33

4.2 Formation of the light propagating operator 33

4.3 The pixelation of the phase space 38

4.3.1 Calculation of the 2D finite operator 39

4.3.2 Eigen-analysis of the finite operator 46

4.4 A comparison of the pixelated phase space with the ray-traced one 50

4.4.1 Evolution of the intensity from a pixel 53

4.4.2 Evolution of a Gaussian spot 57

4.4.3 Calculation of the power distribution by altering the pixel area . . . 57

4.5 Chapter summary 58

5 Formation of the pixelated phase space for step-index fibres 62

5.1 Introduction 62

5.2 Representation of 3D rays in the phase space for step index fibres 64

5.2.1 Representation of position and momentum in 3D 64

5.2.2 Division of power at the core-cladding interface 68

5.3 Formation of the coarse-grained phase spaces for step index fibres 69

5.3.1 Formation of the extended finite operator 72

5.4 Excitation at the input face of the fibre 74

5.4.1 A uniform light source model at the fibre input face 78

5.4.2 Gaussian distributions at the fibre input face 81

5.5 Chapter summary 84

6 Properties of the 2D finite operator for step-index fibres 86

6.1 Introduction 86

6.2 The phase space transport 87

6.2.1 Leaky resonance 88

6.2.2 Eigen-decomposition of the 2D finite operator 92

6.3 Variation of the phase space resolution and refractive indices of the fibre . 100

6.3.1 The effect of a finer resolution in the coarse-grained phase space . . 102

6.3.2 Controlling the leaky resonances by changing the cladding refractive index of the fibre 103

6.4 Chapter summary 109

7 The net power accumulation in the core in step-index fibres 115

7.1 Introduction 115

7.2 Diffusion measurement 116

7.2.1 Propagation in a step-index fibre with circular core and cladding boundaries. 119

7.2.2 Propagation in a deformed step-index fibre 121

7.2.3 2D net power accumulation in the core 123

7.3 The net power accumulation in the core in 3D 125

7.3.1 A toy model 126

7.3.2 Step index fibres with circular core and cladding boundaries 130

7.3.3 Step index fibres with deformed core and cladding boundaries . . . 131

7.4 Chapter summary 133

8 Optimisation of step-index fibres for better power accumulation in the core. 135

8.1 Introduction 135

8.2 Input excitations in the phase spaces 136

8.3 The net power accumulation in the core in the SIF 137

8.3.1 Calculations in 2D 137

8.3.2 Calculations in 3D 138

8.3.3 Dependence on the cross-sectional area of the core 142

8.4 Chapter summary 149

9 Conclusions and suggestions for future work **150**

9.1 Summary of thesis achievements 150

9.2 Applications 151

9.3 Future work with active optical fibres 152

References **152**

Chapter 1

Overview

1.1 Introduction

An efficient ray-based dynamical model, termed as the finite operator model, is developed to investigate the propagation of light in deformed step index fibres (SIF). The model incorporates aspects of wave chaos theory in optical billiard systems to develop a novel numerical method to propagate light distributions through 3D SIF. This research was motivated from the use of these optical fibres for applications in mid-infrared (MIR) photonics, where better simulation methods are required to study the mechanism of light propagation in non-standard optical structures. Optical fibres transparent to MIR frequencies are investigated extensively in the author's research group, and the model developed in this thesis can be applied to the design and fabrication of deformed active and passive optical fibres. The developed optical fibres will be used for applications in remote sensing, spectroscopy, and the generation, transmission, and amplification of MIR light [1].

The propagation of light through deformed fibres is modelled using phase space transport. The phase space used, also known as the Poincaré surface of sections (SOS) [2], is a standard tool for the investigation of billiard-like ray dynamical systems. This phase space is a portrayal of all possible states of a dynamical system and is a convenient tool

to study the behaviour of rays trapped inside deformed boundaries. Various calculations can be undertaken on this multidimensional space and this method is widely used in the investigation of quantum mechanical phenomena in classically chaotic systems.

The propagation of light in optical fibres is studied usually in terms of modes. In cylindrical optical fibres, or any symmetrical waveguides, the modes of propagation are very well-defined with smooth wave-functions and whose intensity profiles are also very well-understood. When asymmetries are introduced in the fibre, the wave functions are not so distinct, and form speckled intensity patterns due to interference of many wavefronts propagating from different qausi-random directions. In this thesis, the investigation is carried out on large multimode fibres where it is assumed that $\lambda \to 0$ for all operating wavelengths concerned. The analysis of modes in the speckle regime can be analysed using methods like Gaussian statistics for ergodically guided modes using concepts like local density of states [3]. The spectral and spatial properties of modes in speckle regime can be found in the imprints of their intensity patterns. However, mode analysis of complex chaotic wavelets are beyond the scope of the model described here. Instead, the focus is given on properties that have been averaged over many modes (or frequencies) and these averaged quantities free of interference effects are well described by ray-tracing in the limit $\lambda \to 0$.

In this thesis, a finite operator method is developed that involves the coarse-graining of a two-dimensional phase space. The process allows an ensemble of rays to be propagated in SIFs in the presence of a core-cladding dielectric boundary that separates the two dielectric media. Simply ray-tracing in such structures is an inefficient process because the number of rays increases exponentially with the number of reflections upon hitting the dielectric boundary; the power in each ray is split between a transmitted ray and a reflected ray, and this causes an exponential rise in the number of rays needed to be traced. The finite operator model developed here provides an efficient numerical solution to this problem without running out of computing memory.

In addition, this method allows the net accumulation of power in the core to be measured

at the end of propagation for any light distribution in the fibre. The difference in the power entering the core, and the power leaving the core can be measured after each reflection using the finite operator method and the total power accumulating in the core can be obtained after the transmission of light through a fibre with infinite length. In this thesis, this measurement is done for SIFs with various boundary deformations, various input distributions, and after changes in the refractive indices of the core and cladding media. Using the finite operator model, non-standard optical step index fibres can be designed, and the input excitations can be modified to excite specific regions in the fibre to maximise the net power accumulation in the core. The explicit calculations are for loss-less, no-gain SIFs but the underlying approach also applies to fibers with gain and loss in the propagation.

1.2 Aims and Objectives

The aim of the work described in this thesis is to develop a ray-based model to propagate light through deformed optical step index fibres for applications in MIR photonics using MIR transparent glasses.

The objective is to obtain a measurement for the net accumulated power in the core after light propagation through the fibre. Investigations are carried out by introducing various deformations in the fibre boundaries and input light distribution to see the changes in the net accumulation of power in the core.

1.3 Thesis layout

The thesis consists of nine chapters. This first chapter gives an overview of the project, the aims and objectives, and the layout of the thesis. In chapter 2, the background behind the concepts used to build the finite operator model is presented. Chapter 2 will explore the field of ray-dynamical systems, and survey the devices investigated in the past

that exploited ray-based analysis. It will discuss the motivations behind investigating appropriate ray-dynamical analysis for modelling classical chaotic phenomena because wave-based approaches find such systems too complex to solve. In addition, the chapter will also indicate other forms of the finite operator being applied to dynamical systems to study wave chaos.

In chapter 3, the analysis of this thesis is started with the investigation of the phase space, or surface of section (SOS) patterns of rays in deformed boundaries. The patterns formed by ray-tracing inside an enclosed boundary, or cavity, can be classified as either regular or chaotic in the phase space. The variation of these patterns and the rise of chaotic trajectories as the boundary deformation is increased are investigated.

In chapter 4, the model to propagate light through 3D optical fibres using the finite operator method is introduced. The operator is discretised by coarse-graining the phase space. Ulam's method is adopted to coarse-grain the phase space, and the finite operator is formed that is able to transport any arbitrary light distribution through a fibre having any deformed cross-sectional boundary. The finite operator is applied to unstructured optical fibres in chapter 4, and a comparison is made between the finite operator method and the ray-tracing method in illustrating the SOS light distribution. Due to the SOS being coarse-grained, a numerical artefact is introduced in the dynamical model called diffusion. The SOS obtained by the ray-tracing method, where there is no diffusion, and that obtained by the finite operator method are compared with each other in an unstructured fibre to investigate the effect of diffusion artefacts in the system.

In chapter 5, the finite operator is extended to the case of SIFs. SIFs consists of the core and cladding cross-sectional boundaries each of which can be deformed to increase the chaotic propagation of light. Separate SOSs are created for each boundary and the finite operator is expanded to take account of the light propagating in different dielectric media and reflecting at different dielectric boundaries. The ray-tracing method is numerically intractable in the SIF owing to the exponential rise in the number of rays to be traced. The finite operator method provides an efficient solution to this problem, and makes

modelling the propagation of light through a deformed SIF tractable.

In chapter 6, pixlated light distributions in the SOS are propagated in the SIF in a 2D setting using the finite operator model. The properties of the constructed finite operator is investigated in relation to the changes in various modelling parameters. Diffusion artefacts introduced by the discretisation limits the number of reflections that can be carried out by the finite operator. The diffusion over successive bounces can be minimised by finer pixelation and the analysis of identifying a steady state that adheres to the physical phenomenon is explored.

In chapter 7, a method to calculate the net accumulation of power in the core in SIF is introduced by using the finite operator model. The model allows the power going into and coming out of the core to be monitored after each reflection, and enables the measurement of the net power accumulated in the core after light propagation through the fibre. In this chapter, the procedure to calculate the net power accumulation in the core is presented with the help of a simplified "toy model". The procedure is then extended to SIFs with circular core and circular cladding boundaries. These structures are chosen because the propagated light distribution in their SOSs does not suffer from diffusion artefacts. The results obtained in these diffusion-free dynamical systems are then extended to systems with diffusion, such as the propagation of light in deformed SIFs. The net accumulation of power is estimated by considering the limiting conditions imposed by diffusion.

In chapter 8, a survey is done by changing the various modelling parameters and the design of the fibre to investigate the relationship between those changes and the net accumulation of power in the core. The investigation also includes variations in the input excitation to the fibre, that is then propagated using the developed method. These modelling parameters will be useful for the design of optical fibres and investigation highlights how they can be potentially used to optimise the net power accumulation in the core of non-standard SIFs.

The explicit calculations in this thesis are limited to passive optical fibres. However, the method of calculating the power accumulation in the core can be extended to model light

propagation in optical media with gain. The optical fibre can be made active, and the propagation of amplified light can be modelled using the finite operator method. The scope for further research on this and other topics using the finite operator method is briefly discussed in chapter 8, where concluding remarks are also made on the achievements described in this thesis.

Chapter 2

Background

2.1 Introduction

A finite operator model is developed in this thesis to propagate light in deformed optical fibres. Light is modelled as rays and ray-dynamical systems are explored to develop an efficient numerical method of propagating light through optical fibres, independent of the operational wavelength. The model incorporates chaotic ray behaviour, introduced due to deformations in the cross-sectional boundaries of the fibre. The finite operator model allows for the propagation of both regular and chaotic light through any deformed unstructured or step index fibre (SIF).

The investigation is aimed towards modelling the transmission of light in rare-earth (RE) ion doped active optical fibres for the potential development of bright mid-infrared (MIR) light sources, and MIR sensors. A brief outline of the relevant on-going MIR photonics research, specifically using MIR transparent chalcogenide glasses, is discussed in section 2.2. Analysis of deformed optical fibres incorporates aspects of quantum and wave chaos theory, and the on-going research in the field is discussed in section 2.3. An operator based approach is adopted in the model to propagate a given light distribution in the fibre after successive reflection, called the Frobenius Perron operator (FPO). The application of such operators numerically, after discretisation, in other dynamical systems is discussed

in section 2.4.

2.2 Mid-infrared photonics

The emerging field of mid-infrared (MIR) photonics for spectroscopy and sensing motivates the investigation of deformed optical fibres in this thesis. At MIR frequencies, the vibrational states of various molecular species can be detected using MIR spectroscopy. Identification of the "fingerprint" response of the vibrational states enables the sensing of materials for applications in explosives and narcotics detection for security purposes, pollutants detection in the environment for maintaining air quality [4, 5], and MIR radar for air collision avoidance systems [6].

Towards the development of all-optical MIR transparent systems for spectroscopy, new optical fibres have been developed that are transparent at MIR wavelengths, based on the chalcogenide glasses (ChGs) [7–9]. These optical fibres can be used, for example, for delivering light from a source to a sample containing the MIR-active molecular species, and collecting MIR signal from the sample and delivering it to a dectector. In addition, optical systems based exclusively on MIR operational frequencies also need to be compact and robust for remote and non-intrusive sensing applications. Standard silica glass fibres are unsuitable for MIR transmission because the propagation losses in these fibres are prohibitively large at these wavelengths [10]. Alternative methods such as Raman spectroscopy, which is currently the industrial standard, provide compact silica based optical systems for spectroscopic applications, but suffer from low power, scattered signals, and require very sensitive detection. MIR spectroscopy can provide manifold improvements from the existing standard because the signals coming from the sample are potentially much stronger compared to those used in Raman spectroscopy. However, bright MIR light sources and amplifiers are still in the developemental phase, and this presently creates a limitation in building compact and/or remote MIR light delivery systems that are essential for robust and versatile measurements. Therefore, optical systems operating entirely

at MIR wavelengths are highly desirable, and could potentially give rise to a myriad of new MIR photonic applications. A perspective into the state of the art research and development being caried out in MIR photonics, and the possibilities of MIR spectroscopy in imaging and remote sensing has been discussed in detail by Seddon [1].

At the author's university, the Advanced Materials Research (AMR) group, in collaboration with George Green Institute for Electromagnetics Research (GGIEMR), has been engaged in testing and developing very high purity, active and passive, ChG optical fibres for applications in MIR spectroscopy. One targeted use of ChG fibres in MIR spectroscopy is in the detection of biological samples [11], and MIR multispectral imaging can be used for effective real-time screening of early stage cancer, which can pontentially open up a new chapter in MIR healthcare photonics [12]. The ChGs are stable chemically, and can be drawn into fibres. The optical loss performance depends on the purity of the extruded fibres. Passive ChG optical fibres have been demonstrated to have low loss owing to the development of advanced purification processes within the AMR group [13–15]. The ChGs are amorphous glasses that are transparent in the $2.5 \sim 25\mu m$ wavelength range depending on their compositions. They are based on selenium (Se), sulfur (S) and tellurium (Te) which are in the group 6 in the periodic table; various compositions of glass are possible with one or more of these three chalcogens covalently bonded with elements such as As, Ge, Ga, Sb, and P [16].

Figure 2.1 shows a comparison of the transmission spectrum in the infrared region between various bulk ChG glasses, SiO_2 and fluoride (ZBLAN) glasses. It shows a cut-off in transmission above $4\mu m$ for SiO_2 and $8\mu m$ for ZBLAN. ChGs based on sulfides, selenides, and tellurides have a wide transmission range for IR. It should be noted that each peak transmittance shown in figure 2.1 is limited by the loss due to Fresnel reflections at the surfaces of the glass which are large for the ChGs owing to their high refractive indices [17].

ChGs not only exhibit a high refractive index but are also highly non-linear optical materials. A particularly fertile ground for research and development in ChGs is in their highly non-linear optical properties, and most prominently, the non-linearity was exploited re-

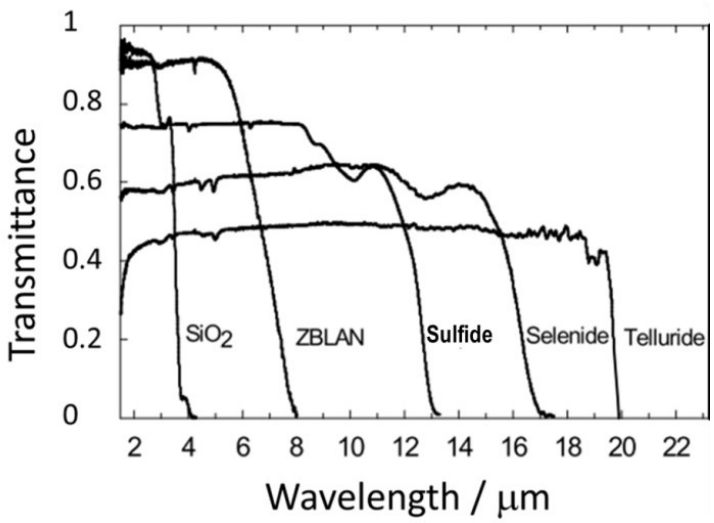


Figure 2.1: Figure from Sanghera *et al.* [8], comparing the transmittance of bulk glass samples of silica, ZBLAN (a heavy metal fluoride glass), with chalcogenide glasses based on sulfides, selenides,and tellurides.

cently to make a wide supercontinuum (SC) generator [18]. The SC generation of MIR spectra in ChGs has enabled ultra-wide band light sources that are brighter, more efficient, and more compact than hitherto attainable MIR sources [19–22]. Apart from non-linearity, ChGs also have a low multi-phonon relaxation rate which enables them to host rare-earth (RE) ions for use as fibre lasers [23]. The model developed in this thesis is aimed at helping the development of more efficient RE-ion doped active fibres for MIR signal sensing, and amplification. Although only passive fibres are modelled in this thesis, the finite operator model can be easily extended to active optical fibres with deformed boundaries. The deformation introduces chaotic light propagation that improves fibre performance, and is dealt with using concepts from quantum-wave theory. Investigations of chaotic waves are undertaken using ray-dynamical models, and a few concepts and devices relating to this research field are introduced in the following section.

2.3 Chaotic ray dynamics

Dynamical modelling of, billiard-like, rays confined within prescribed boundaries originates from the field of quantum and wave chaos theory [24–26]. Chaotic light trajectories

in deformed cavities or boundaries behave analogously to point masses following the rules of classical mechanics. Quantum chaos is the study of the wave-like motion of subatomic particles, electromagnetic light, and acoustic waves etc, which exhibit chaotic behaviour, and aspects of these systems can be very well described by modelling ray-billiards. The aim of the study of quantum chaos is to understand the interference behaviour of waves in the geometrical limit (wavelength $\lambda \to 0$). In this project, light propagating chaotically in deformed optical fibres is investigated, where concepts from the study of quantum and wave chaos systems are applied.

The research in quantum chaos has led to the emergence of various sub-fields such as periodic orbit theory [27], random matrix theory [28], and dynamical localization [29,30]. The origins of this type of investigation can be related to experiments done by Chladni who, as described by Rees [31], in order to visualise sound waves, set up grains of sand on vibrating plates and used high-amplitude sound waves to form nodal lines on the plates. He documented this work in his book *Die Akustic*, published in 1802, and after two centuries, modern studies of the equivalent of nodal lines in wavefunctions were set up on microwave resonators [24], dielectric optical cavity resonators [32], and electrons trapped in the potential well of atomic nuclei [33]. Light trapped in optical cavities produce similar patterns as Chladni plates and microwave cavities, and are commonly used as dynamical systems for the study of various wave-chaos phenomena. Applications in the field of quantum and wave chaos include the design of optical cavities [32], modelling complex atomic nuclei [33], quantum dots [34], Rydberg atoms [35], cold atoms [36], acoustics [37], microwaves [38], surface waves [39], and elastodynamics [40].

In the following subsection, the application of quantum and wave chaos theory in 2D asymmetric resonant optical cavities is briefly discussed, where investigation of ray-dynamical systems has enabled the implementation of directional emitting devices. In this thesis, the method of applying a smooth deformation to the fibre boundary has been adopted from such studies. In subsection 2.3.2, the ongoing research being carried out on deformed active optical fibres is discussed where concepts from wave-chaos theory have been applied to fibre propagation in an attempt to improve pump power absorption in fibre lasers.

2.3.1 Chaos analysis in deformed optical microcavities

A particularly rich field in quantum chaos research is in the development of devices related to optical microcavities [41]. Like a tuning fork, these have a size-dependent resonant frequency spectrum. Because of the microscale volume the resonant frequencies are distributed more sparsely than macroscale resonators. Two parameters for measuring the performance of these resonators are their Q factor (which can be related to loss) and volume [32].

An optical cavity resonator has a set of modes each with its own resonant frequency ω_i with resonance width $\delta\omega = 1/\tau$, where τ is the lifetime of photons in the mode. Substantial deformation of the resonator shape results in partially chaotic dynamics, and causes frequency-independent broadening of the so-called whispering gallery resonances and highly directional emission. Solutions of the wave equation for asymmetric cavity resonators (ARCs) have been developed by Nöckel *et al.* [42] that relate to the ray optics model, and also reveal a frequency-dependent effect of the chaos characteristics of quantum chaos systems. With small deformations of the ARC, the lifetime of the resonance is significantly shortened, but for larger deformations ($\sim 10\%$) there are some resonances which have longer lifetimes than predicted by the ray-chaos model because of a phenomenon called dynamical localization [29, 43]. Directional emission from ARCs has been studied extensively [44–46], and has applications in optical WDM systems for filtering, switching, lasing [47], modulation, and spectroscopy [44, 48, 49].

2.3.2 Chaos analysis in deformed optical fibres

Experimental analysis done on erbium doped fibre amplifiers (EDFAs) by Doya *et al.* [3, 50–52] suggests that light is absorbed more effectively from side-pumping in deformed optical fibres than in symmetric ones. This is because the chaotic rays are able to uniformly distribute the pump power inside the fibre through chaotic propagation, and fill up any caustic regions that would otherwise have remained in a circular geometry. Side-

pumping in double-clad fibres (DCFs), with core doped in Er^{3+}, has the advantage that it leaves the fibre end open for splicing. In geometries investigated by Leproux *et al.* [51], gain in deformed EDFAs after propagation along a 40cm length of the fibre of 17dB was observed at $1530nm$, as opposed to just 2dB observed in the circular counterpart. Modelling results by Kouznetsov *et al* [53,54] indicate that a break from the circular symmetry in the inner cladding of double-clad fibres results in a significant increase in the the pump power coupling efficiency.

Optical fibre amplifiers (specifically EDFAs) are widely used in long-haul optical links to restore power in the transmitted signals. Snitzer *et al.* [55] proposed fibres with double cladding to overcome the challenges of coupling of high pump power into a doped core. To reduce the high pump power required in such fibre amplifiers, the inner cladding is required to be designed to allow the optimum pump power absorption. Towards that end, the inner cladding shape was deliberately made asymmetrical, and the pump power propagation and absorption were modelled by invoking principles from wave and quantum chaos theory. The light was modelled as rays and the absorption of pump power in such deformed multimode fibres was investigated within the framework of wave chaos.

The interference of chaotic rays uniformly scattered around the fibre due to boundary deformations form speckled-patterns or scars [56]. Scarring was first discovered in a quantum chaos problem [57] and scarred modes have been investigated in rectangular and semi-stadium like resonant cavities. Scars have been found in light propagation in many deformed cavities, except for elliptical boundaries which do not show such scarring [58]. Analysis of scars has other applications such as in semiconductor ballistic quantum dots [59, 60], photoionization of Rydberg atoms [61], and microwave systems. In fibre amplifiers, these scar-like modes can be selectively amplified to enhance the performance of the fibre amplifier [62–64], and also to study mode behaviour using mixed dynamical systems [65]. Deformations studied in their analysis included modelling fibre cross-sections as truncated disks, inducing abrupt asymmetries in the light propagation. The investigation reported in [65] focused on the statistical and spatial characteristics of scar modes in the propagation.

The deformations introduced in the optical fibres studied in this thesis are smooth, where a deformation parameter is defined which can introduce a gradually increasing chaotic behaviour in the light propagation, similar to what was used in the study of ARCs discussed in the previous subsection. In addition, the analyses carried out here are geared towards obtaining the accumulation of power in the core after propagating a given input excitation, rather than the investigation of the modal distribution of scars. Although only passive optical fibres are considered in this thesis, such calculations can easily be extended to active optical fibres doped with RE ions in the fibre core.

2.4 Operators of the Frobenius-Perron type

The phase space method is used to analyse the rays in the fibre and classify them by regular or chaotic motion, similar to the analysis done for asymmetric microcavities discussed in subsection 2.3.1. In a SIF, there are multiple boundaries and phase spaces are constructed for each boundary, and each dielectric media, to track rays propagating through the fibre. The SIF confines the light by total internal reflection (TIR). It consists of a core medium with refractive index n_c that is surrounded by a less dense cladding medium with refractive index n_{cl}. The phase space registers the rays as they hit these boundaries after each reflection, and distributes the propagated power through the available phase space.

However, ray tracing in the SIF becomes intractable very quickly because of the ray splitting of power between refracted and reflected rays upon hitting the core-cladding dielectric boundary; thus the total number of rays to be traced increases exponentially. A large number of rays must be traced for many reflections in order to see the propagated light distribution along the fibre reaching a steady state, and the exponential growth in the number of rays due to the dielectric boundary creates a significant computational burden. Therefore, in order to analyze the ray distribution for many reflections, a method called the Ulam's method is explored which involves the construction of a finite Frobenius-Perron operator (FPO) [66], which is termed here as the finite operator, based on Ulam's

conjecture [67]. The Frobenius-Perron theorem [68] applies to this operator which has positive and real elements, and is a square dimensional matrix.

According to Ulam's method, the SOS is divided into separate regions and a probabilistic approach is adopted to the measurement of the dynamics. On this basis, a finite approximation of the operator is used iteratively to distribute the power in the SOS. The SOSs of other maps such as the Chirikov standard map [69], random interval map [70], and the Arnold cat map [71] have been investigated using the finite approximation of the FPO. The eigenvalue spectrum of the finite FPO has also been investigated extensively [72–79] to analyze the dominant characteristics of the distribution. The spectral decomposition of a finite operator formed by making rectangular grids in the phase space of an optical microcavity was invesigated recently by Kullig *et al.* [80]. In the work described in this thesis, this approach was being developed independently for the analysis of deformed SIFs since 2014.

2.5 Chapter summary

In this chapter, the background of the research relevant to this thesis has been discussed. The research was motivated by the experimental programme at Nottingham for the development of optical fibre amplifiers and sensors for aiding MIR photonic applications. A ray-based model is explored in this thesis for deformed fibres, where concepts from quantum-wave chaos theory are investigated to develop efficient numerical methods to propagate light in deformed optical fibres. Other applications of such ray-based modelling concepts were highlighted in this chapter, such as asymmetric optical resonators for making directional micro-emitting devices and deformed EDFAs for improved pump power absorption. Lastly, the light is propagated in this thesis using a type of operator, called the Frobenius-Perron operator, and the application of such operators was discussed in section 2.4. The operator developed in this thesis will be discretised by modelling propagation numerically using a finite number of rays in the fibre. In the following chapter, this

analysis is initiated with the investigation of mixed chaotic and regular SOS patterns in deformed unstructured optical fibres. The finite operator model based on coarse-graining the SOS will then be discussed in chapter 4.

Chapter 3

Ray-tracing in mixed phase spaces

3.1 Introduction

A ray optical method of analysis is used throughout this thesis to model light propagation in optical fibres. The ray-tracing method is a tool for modelling the billiard-like dynamics of rays inside a boundary. In this chapter, the investigation of light in mixed phase spaces are carried out in two dimensional, perfectly reflecting, deformed boundaries. The analysis is undertaken to model light in the cross-section of unstructured optical fibres, and is relevant to the development of the finite operator model introduced in the following chapter. The patterns in the phase space investigated in this chapter classify the propagation of rays into regular and chaotic motion. A phase space showing these two types of motion simultaneously is called a mixed phase space. The efficacy of the finite operator model will be determined by the interplay between the chaotic and regular ray motion in deformed optical fibres.

Rays bouncing around in symmetrical boundaries would show a regular motion in the phase space. Examples of symmetric boundaries include circles, ellipses, and equilateral triangles. Any deformation introduced in the boundary, resulting in the breakdown of symmetry, causes rays to bounce around chaotically, and rays appear in the phase space as random patterns. An example of a highly asymmetric enclosed boundary is a stadium-

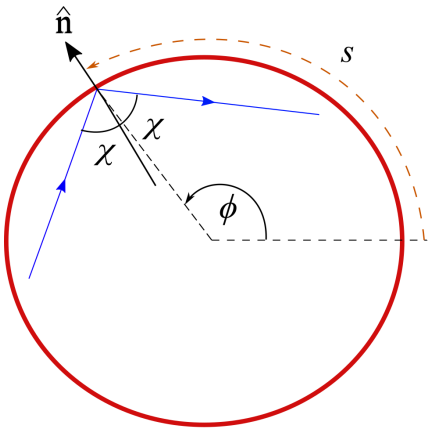


Figure 3.1: Tracing a ray in a unstructured fibre cross-section. The position is tracked by the arc length s, and the direction is measured by measuring the angle of incidence χ at the boundary.

like shape, also known as a Bunimovich stadium [57], and it consists of parallel straight lines closed off by semicircles at the ends. The phase space of the Bunimovich stadium is entirely chaotic. The phase space of most generic shapes, however, is mixed and consists of partly regular and partly chaotic motion. The reason for the motion of rays to be classified in this way is because only the regular motion in the phase space is *integrable*, i.e. it is possible to determine symmetries in the regular motion. Determining symmetries of motion allows for conventional Eikonal or Gaussian optical methods of analysis to be applied to determine exact wave solutions to these motions. Chaotic rays in the phase space, on the other hand, are not integrable and wave solutions are difficult to find. This has prompted in the past the requirement for dynamical methods to be applied to determine a measure of these motions [71, 81].

In this chapter, the ray-tracing method is applied to propagation of light in unstructured optical fibres. A ray of light undergoes many reflection as it propagates through the fibre. In the ray-tracing method, the ray is tracked using the boundary phase space. It involves tracking the position and direction of the ray when it hits the boundary of the fibre. Figure 3.1 shows the cross-section of an unstructured fibre where a ray is specularly reflected at the boundary. The incident angle is given by χ, and it can be used to indicate the direction of the ray. The momentum of the ray is given by $\sin\chi$, and in a specular reflection, since the incident angle is equal to the reflected angle, the momentum

is conserved. The position of the ray at the point of reflection is tracked by the boundary arc length s. As shown in figure 3.1, this arc length is measured by finding the angle ϕ counter clockwise from the origin. As ϕ varies from 0 to 2π, the arc length s also varies from 0 to the total circumference $s_{\max}$. The relationship between ϕ and s is determined by using the equation defining the boundary.

The position and momentum of the ray can be represented together in the phase space. The phase space is represented using the area-preserving Birkhoff coordinates (s, p) [82], where $p = \sin\chi$. It is also known in literature as the Poincaré surface of section (SOS), and it is a space created to capture a snapshot of the rays as they pass through a section in space. In general, the position and momentum coordinates can be quantities other than s and $\sin\chi$ respectively for other dynamical systems [69, 71]. In the case of ray-dynamical systems, the phase space is used to track rays in an enclosed boundary, and this allows various investigations to be made on the trapped light distribution [32,80]. The phase space with $(s, \sin\chi)$ coordinates serves as a map from which it can be determined whether a particular trajectory is regular or chaotic. Deformations are introduced in the boundary which allows a subset of rays to reflect on the boundary in a chaotic manner. The analysis of ray trajectories with the phase space method has been used extensively in the past [83–85] for investigating 2D asymmetric cavity resonators.

The rays are registered in the phase space when they are reflected at the boundary of the fibre. Figure 3.2 shows the $(s, \sin\chi)$ coordinates being registered in the phase space as a ray reflects in a clockwise manner in the fibre cross-section. Note that $\sin\chi$ is taken to be positive for rays reflecting in a counter-clockwise manner in the fibre cross-section, and this convention is followed throughout this thesis.

In the following section, various phase space patterns of mixed trajectories in deformed unstructured fibre are investigated. First, the phase space of a circular cross-section is analysed. Then, the cross-section is gradually deformed to see the emergence of the chaotic motion among rays. The phase spaces shown in the following section are obtained simply by ray-tracing from different initial conditions within a 2D enclosed boundary.

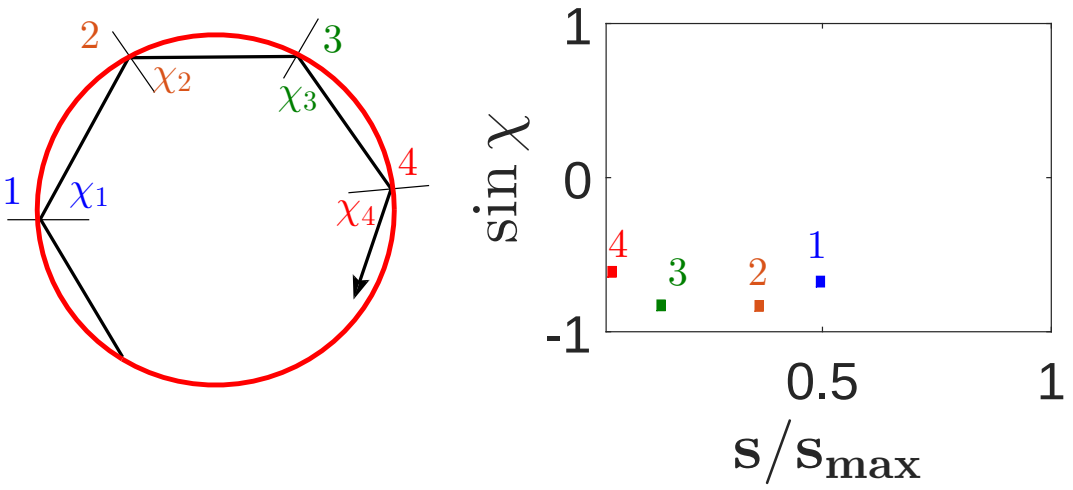


Figure 3.2: Registering the motion of a ray in the phase space. The phase space consists of the normalised arc length $s/s_{\max}$ as the horizontal axis, and $\sin\chi$ as the vertical axis. The phase space points are shown for a ray undergoing four successive clockwise reflections in the fibre cross-section.

3.2 Investigation of phase space patterns

An investigation is carried out in this section on the mixed phase spaces of deformed boundaries described using the quadrupolar equation. The 2D case of billiard-like ray trajectories in a deformed boundary will describe the cross-section of a dielectric rod with the momentum in the z-direction decoupled. The boundary is deformed here using the quadrupolar equation [86] and is given by

$$S_r(\phi) = \frac{r}{\sqrt{1+\frac{\epsilon^2}{2}}}(1+\epsilon\cos 2\phi) \tag{3.1}$$

where, S_r is the radius at ϕ, ϵ is the deformation factor, r is the scaling factor, and (ϕ) is the polar angle from the origin. The pre-factor is inserted so that the area of the cavity remains constant and equal to π, when the value of ϵ is varied. While using the quadrupolar equation, an important assumption in considering the shape is its convexity. A convex enclosed boundary means that there is only one boundary point for each angle, i.e. there is a one-to-one correspondence between ϕ and s. The quadrupole equation becomes non-convex for $\epsilon > 0.2$.

In this chapter, the pre-factor to normalise the cross-sectional area is suppressed as there is just one medium when modelling the cross-section of the unstructured fibre. In chapters 5, 6, and 7, the pre-factor to normalise the cross-sectional area is re-applied and it is further assumed that $r = 1$ when investigating SIFs where there are different core and cladding dielectic media present.

3.2.1 Relationship between s and ϕ for the quadrupolar equation

As shown in figure 3.1, ϕ is the polar angle from the origin and s is the corresponding arc length of the boundary. Equation 3.1, after suppressing the prefactor, is given by

$$S_r = 1 + \epsilon \cos(2\phi) \tag{3.2}$$

Setting $\epsilon = 0$, in equation 3.2 reduces the boundary to a circular billiard. In Cartesian coordinates equation 3.2 breaks down to,

$$x = S_r \cos(\phi) \tag{3.3}$$

and,

$$y = S_r \sin(\phi) \tag{3.4}$$

After substituting equation 3.2 into equations 3.3 and 3.4, and then differentiating equations 3.3 and 3.4 with respect to ϕ, one obtains

$$\frac{dx}{d\phi} = -(1 + \frac{\epsilon}{2}) \sin\phi - \frac{3\epsilon}{2} \sin 3\phi, \tag{3.5}$$

and

$$\frac{dy}{d\phi} = (1 - \frac{\epsilon}{2}) \cos\phi + \frac{3\epsilon}{2} \cos 3\phi. \tag{3.6}$$

The relationship between s and ϕ is given by the following differential equation

$$\frac{ds}{d\phi} = \sqrt{(\frac{dx}{d\phi})^2 + (\frac{dy}{d\phi})^2}. \tag{3.7}$$

After substituting equation 3.5 and 3.6 into equation 3.7 and integrating with respect to ϕ, one obtains

$$s = \int_0^{\phi} \sqrt{(\frac{5\epsilon^2}{2} + 1 + 2\epsilon\cos(2\phi) - \frac{3\epsilon^2}{2}\cos 4\phi)}d\phi. \tag{3.8}$$

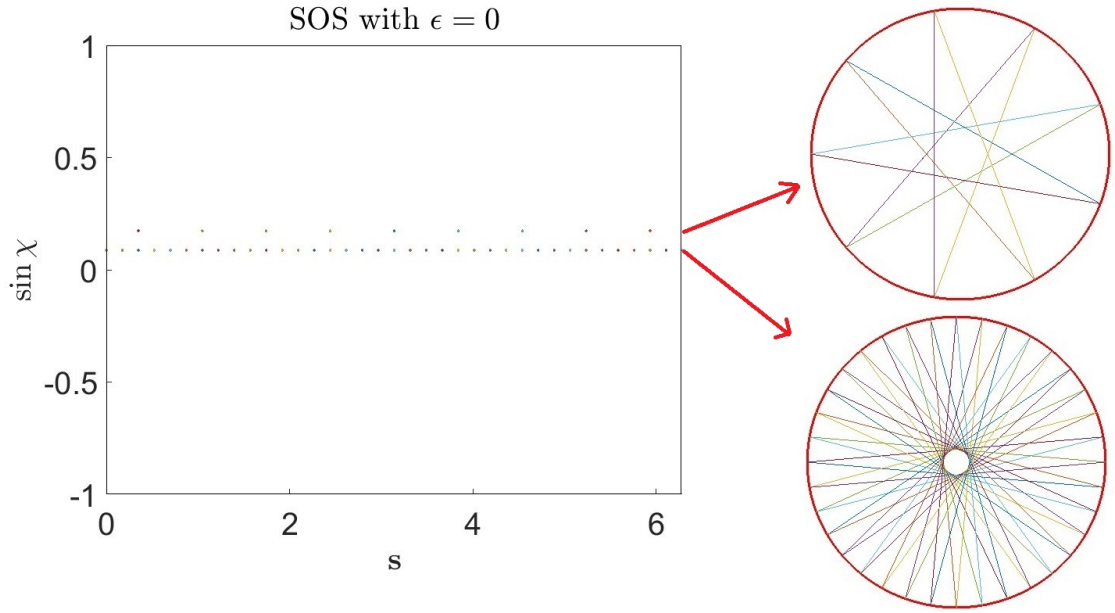
The equation 3.8 may be integrated numerically to find the s value for every ϕ.

The axes of the phase space are now defined in relation to the quadrupolar equation. In the following sections, the phase space of boundaries defined by the quadrupolar equation is investigated with different values of ϵ. With $\epsilon = 0$, the boundary is circular. As the value of ϵ increases the boundary becomes more deformed and the phase space becomes more chaotic. The various regular and chaotic patterns in the phase space are investigated and the expansion of the chaotic region replacing the regular regions, as ϵ increases, is observed.

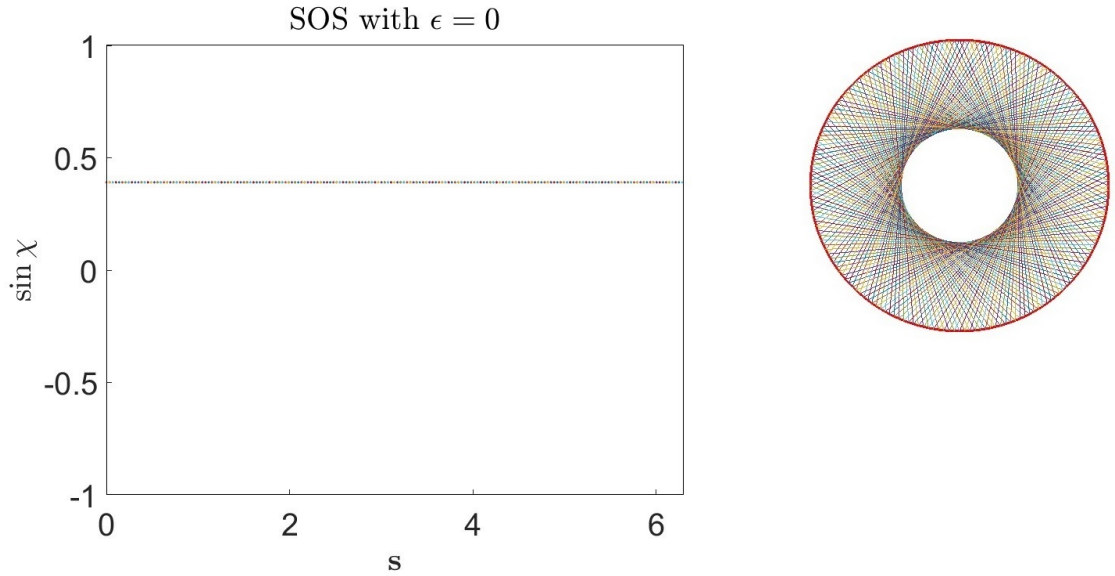
3.2.2 The phase space of a circular boundary

The phase space, or surface-of-section (SOS), of a circular boundary consists of $\sin\chi$ preserving horizontal straight lines. These straight line regular motions consist of periodic and quasi-periodic paths around the boundary. Periodic motions are registered in the phase space as fixed points with period number N_p, whose value signifies the number of bounces before which the ray returns to the same coordinates again in the phase space. Two examples of periodic motion are shown in figure 3.3(a).

Another regular motion of the rays involves a quasi-periodic motion around the boundary. The line formed in the phase space for quasi-periodic motion consists of an infinite number of points. In this type of motion, the rays return back in close vicinity to the initial starting coordinates and trace out a continuous horizontal line in the phase space as shown in figure



(a)



(b)

Figure 3.3: (a)Periodic motion, and (b) quasi-periodic motion of rays in a circular boundary and the corresponding state representation in the phase space (SOS).

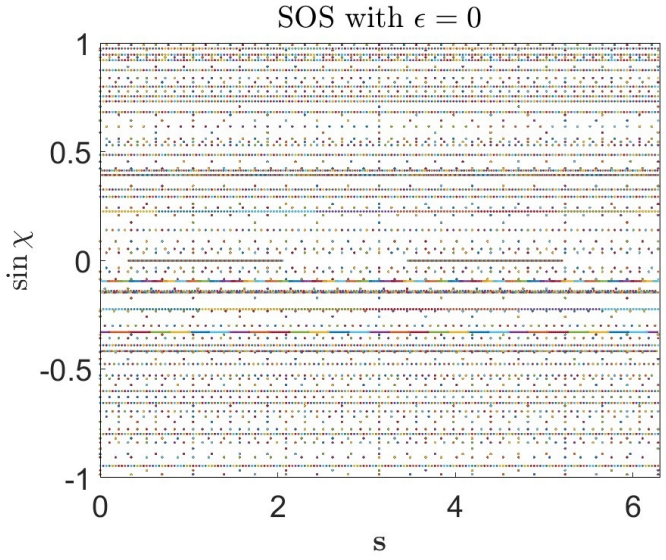


Figure 3.4: The phase space of a circular boundary for various initial conditions. It consists of momentum preserving regular motion.

3.3(b). When $\sin\chi = 0$, the rays are at normal incidence with the boundary and $N_p = 2$. Except for normal incidence, leading to Fabry-Pérot type 2-bounce reflections, the rays always form a caustic region in the middle as they go around the boundary. The caustic region is an empty circular envelope at the centre formed by rays tangentially crossing by.

Figure 3.4 shows the total phase space of a circular boundary for various initial conditions. It has a series of horizontal lines some of which have discrete points along them for periodic motion, and others of which have an infinite number of points for quasi-periodic motion.

3.2.3 Phase space with 5% deformation

With $\epsilon = 0.05$, in equation 3.2, the phase space is mostly regular with the emergence of a small chaotic region. Figure 3.5 shows the fixed points for reflections corresponding to a period of $N_p = 2$. Unlike the circular boundary, there are only a finite number of fixed points for rays with zero momentum ($\sin\chi = 0$). There is a stable fixed point at s for the value of $\phi = \frac{\pi}{2}, \frac{3\pi}{2}$ and $\sin\chi = 0$, which corresponds to a periodic vertical 2-bounce by the trajectories in the boundary as shown in red in figure 3.5. The reason that this point is termed as "stable" is because it hosts the largest amount of regular trajectories in its

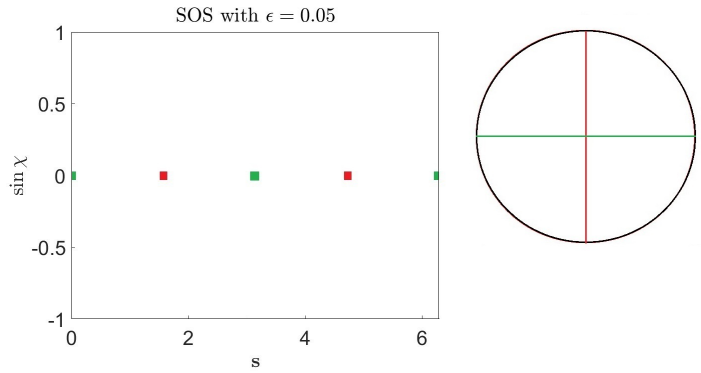
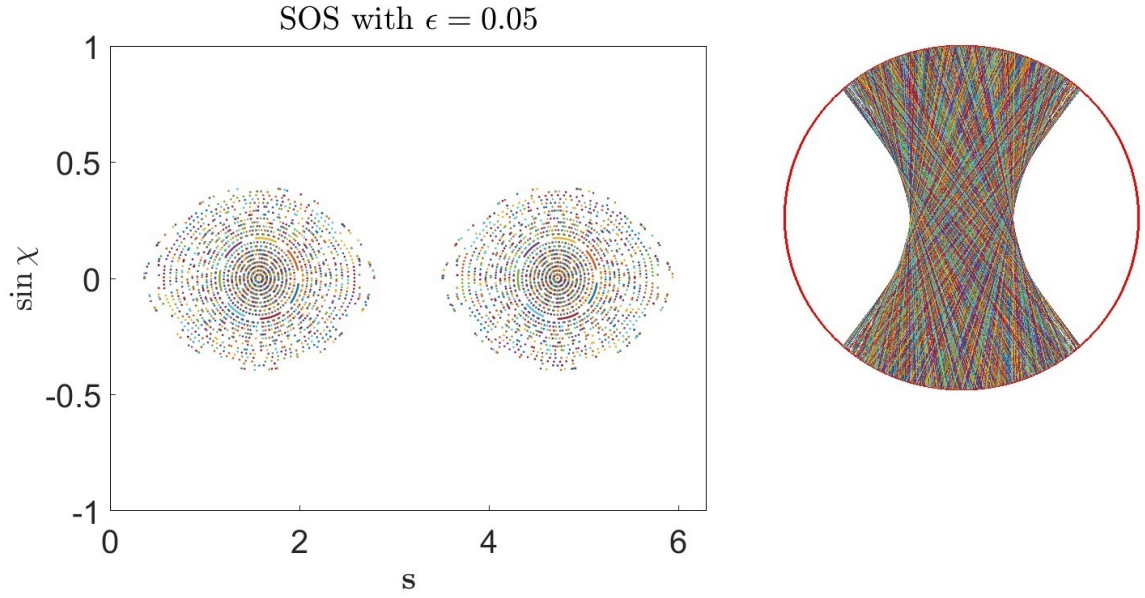


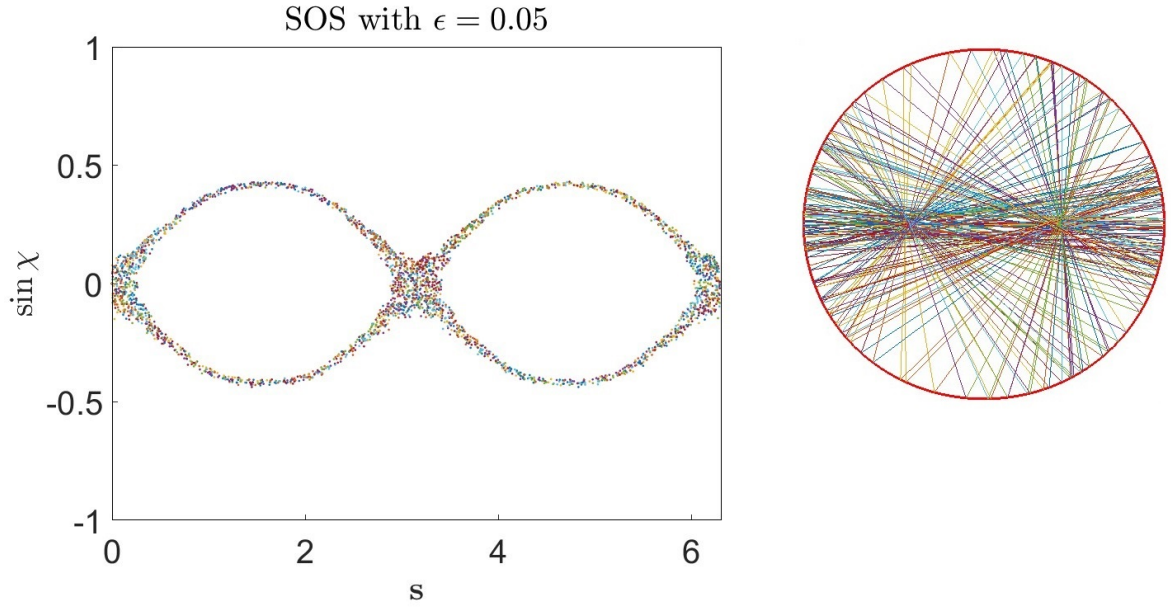
Figure 3.5: Stable (red) and unstable (green) fixed points corresponding to periodic vertical and horizontal bounce ($N_p = 2$) respectively inside the boundary at normal incidence.

vicinity, as shown in figure 3.6(a). On the other hand, there is an unstable periodic fixed point at $s(\phi = 0, \pi); \sin\chi = 0$ corresponding to a horizontal 2-bounce as shown in green in figure 3.5. Trajectories near the unstable fixed point are chaotic and fill a 2D region in the phase space as shown in figure 3.6(b). The chaotic region for $\epsilon = 0.05$ forms a thin layer in-between a continuum of regular region, and covers a finite area in the phase space. The quasi-periodic curves that encircle the fixed points in a concentric manner are also termed as invariant curves (ICs). As one moves further away from the fixed points, the ICs, instead of encircling one fixed point start to span the phase space horizontally with all possible s values enveloping more than one fixed point in the phase space. Various quasi-periodic regular motions are illustrated in figure 3.7.

Since the deformation is very small with $\epsilon = 0.05$ there are a lot of fixed points in the phase space still remaining. In contrast, there is an infinite number of fixed points in the phase space of the circular boundary. Some of the fixed points that host a relatively large number of periodic and quasi-periodic trajectories around them are shown in figure 3.7. The stable periodic fixed points at $s(\phi = \pi/2, 3\pi/2); \sin\chi = 0$ host the largest family of regular motion around them, the collection of which looks like an island in the phase space. There is always a fixed point at the centre of each island. Figure 3.7(a) shows the largest island around the stable fixed point. There are other fixed points in the phase space such as the one shown for $N_p = 4$ in figure 3.7(b). Islands are formed around the fixed points and consist of the quasi-periodic motions that encircle them. As one probes



(a)



(b)

Figure 3.6: (a) Various quasi-periodic trajectories around the stable fixed points at $s(\phi = \pi/2, 3\pi/2), \sin\chi = 0$. (b) Chaotic region around the unstable fixed point at $(s(\phi = 0, \pi), \sin\chi = 0)$.

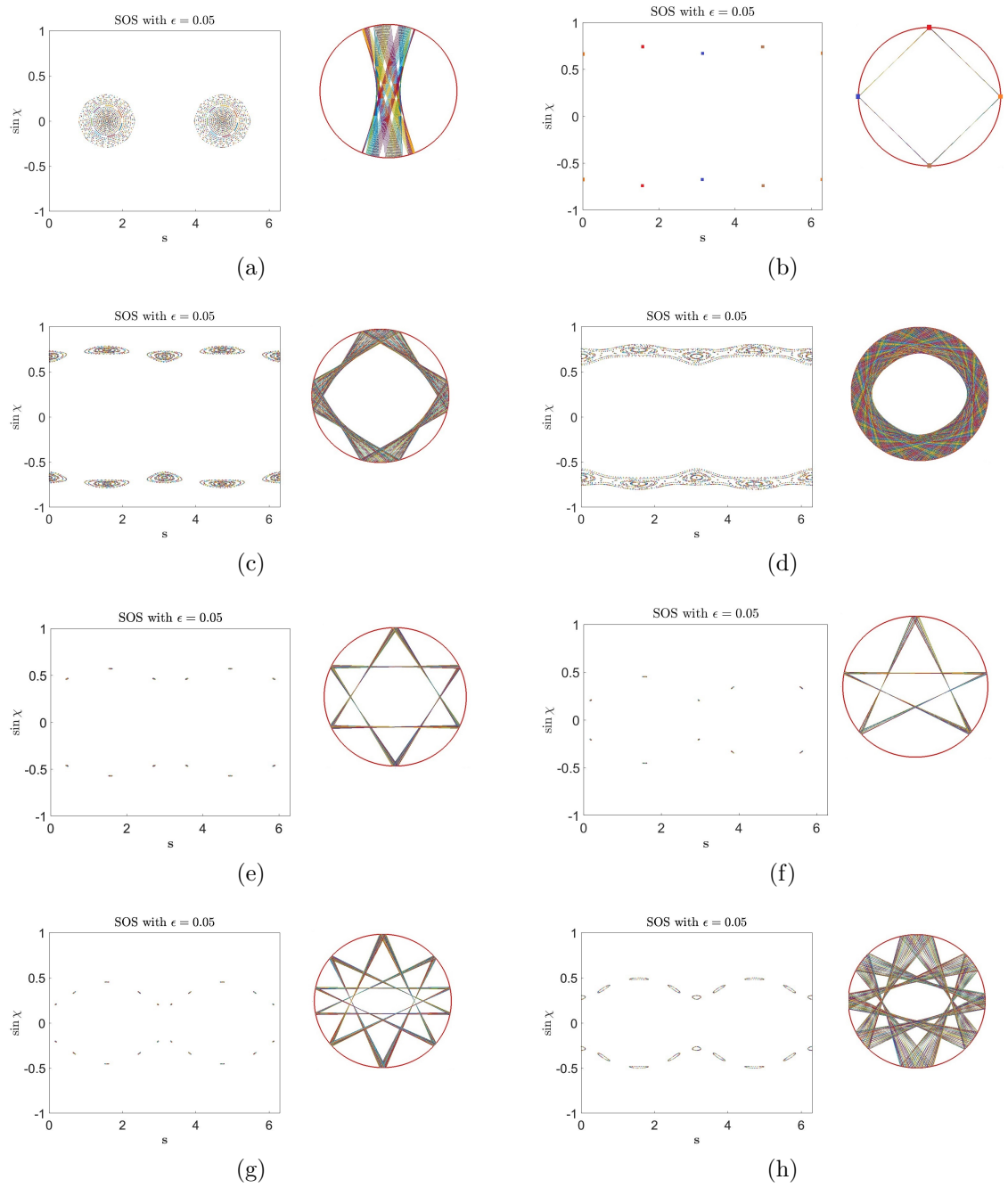


Figure 3.7: (a) Quasi-periodic regions around the stable fixed point at $s(\phi = \pi/2, 3\pi/2); \sin\chi = 0$ that form the largest island of concentric rings. (b) Fixed point at $s(\phi = \pi/4, 3\pi/4); \sin\chi = \pm 0.67, 0.5..$ with $N_p = 4$. (c) Quasi-periodic islands are formed around the fixed points of (b).(d) As trajectories move further away from the fixed points, ICs are formed which envelope multiple islands and the trajectories span all around the boundary with all possible values of s, but within a finite range of $\sin\chi$. (e) Triangular (CCW) and inverted triangular (CW) fixed points with $N_p = 3$. (f) Fixed points in the form of star (CCW) with $N_p = 5$ (g) Quasi-periodic star (CCW) and inverted start (CW) around fixed points (h) Quasi-periodic (star-like) trajectories that form islands in the phase space.

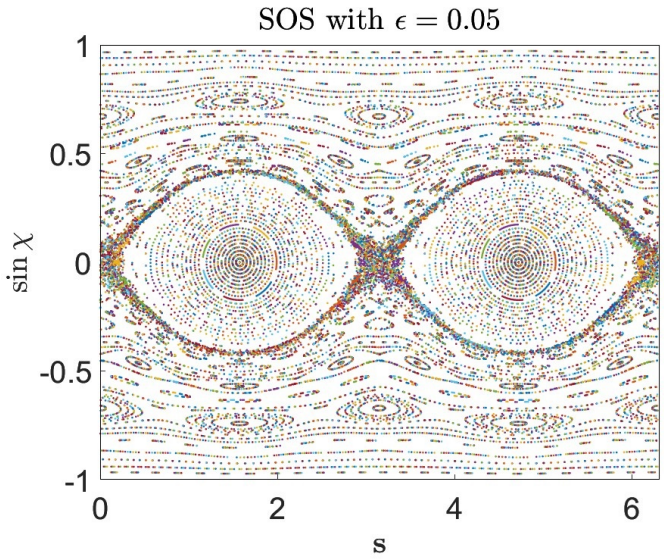
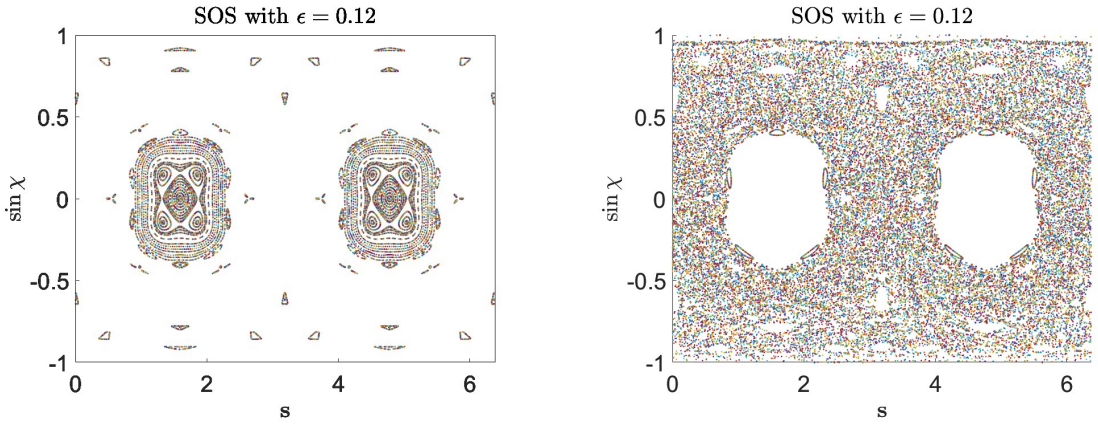


Figure 3.8: The phase space of all the trajectories with boundary deformation of $\epsilon = 0.05$

further away from the fixed points the quasi-periodic motion starts having a complete set of s values and envelope multiple islands as shown in figure 3.7(d). Other fixed points such as triangular motion with $N_p = 3$ in figure 3.7(e), and star-like motion with $N_p = 5$ in figure 3.7(f) and (g) can be found which have a conjugate nature to them (i.e. they can also form in an inverted manner around the boundary). Quasi-periodic islands are also formed in their vicinity, as shown in figure 3.7(h) for the star-like periodic motion. In figure 3.8, the complete phase space pattern is shown for the boundary, and it shows that only the chaotic region in the vicinity of the unstable fixed point covers a 2D area, whereas the rest of the phase space is covered with a continuum of 1D regular patterns formed by periodic and quasi-periodic trajectories.

3.2.4 Phase space with 12% deformation

As the boundary deformation increases, the area of the 2D-chaotic region expands. The regular regions always originate from fixed points at the centre of the islands and show periodic ray motion in the boundary. A series of quasi-periodic motion encircles the fixed points and it degenerates to the chaotic sea as the distance from the fixed point becomes too large. With the increase in ϵ island regions shrink and the fixed points can host a



(a) (b)

Figure 3.9: The phase space of all the trajectories with boundary deformation of $\epsilon = 0.12$

smaller range of quasi-periodic motion in their vicinity.

The fixed point that hosts the largest family of quasi-periodic motion, and hence the largest island of regular motion is termed as the stable fixed point. Various other fixed points can be found scattered in the chaotic sea, but as ϵ increases their number and the size of the islands they can host decreases. For $\epsilon = 0.12$, there is no IC among the regular motion that spans for all s. All the regular integrable regions in the phase space are shown in figure 3.9(a). Figure 3.9(b) shows the complement of figure 3.9(a) which is the chaotic sea.

3.2.5 Variation of the phase space with the boundary deformation

This section summaries the analyses of sections 3.2.3, and 3.2.4 and presents the mixed phase spaces of the deformed boundary for different values of ϵ. Figure 3.10 shows the variation of the SOS patterns with the change in the boundary deformation of a quadrupolar boundary. With no deformation the phase space shows a series of momentum preserving straight lines for different initial condition and consists of only regular motion as shown in figure 3.4. With a slight deformation of 1%, the phase space changes dramatically as shown in figure 3.10(a). The change is mainly for small values of $|\sin\chi|$ with the

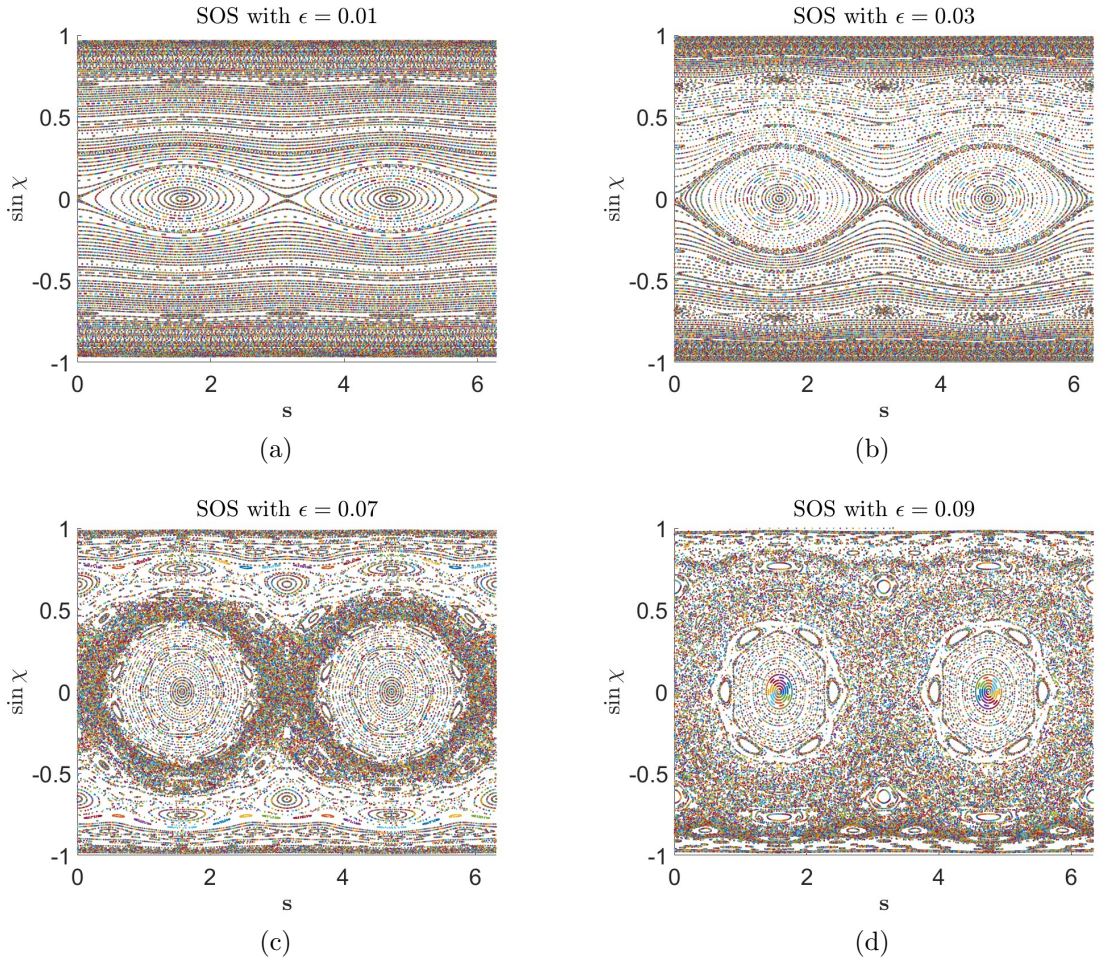


Figure 3.10: The phase space of the quadrupolar equation for various deformations. The chaotic region expands as the deformation increases.

emergence of islands around the stable fixed points for $s(\phi = \pi/2, 3\pi/2); \sin\chi = 0$ as identified in the previous section. Thus with the introduction of a very small deformation, the infinite number of fixed points for $\sin\chi = 0$ is reduced to just the stable ones at $s(\phi = \pi/2, 3\pi/2)$ and the unstable ones at $s(\phi = 0, \pi)$. The phase space is still very regular with a few other islands emerging for higher value of $|\sin\chi|$. For $|\sin\chi| > 0.75$, the ICs become denser as they form whispering galleries, and the reflecting rays closely follow the curvature of the boundary.

For $\epsilon = 0.03$, the islands hosted by the stable fixed points expand. More island structures emerge around other fixed points in the phase space and the ICs close to the whispering gallery are pushed outwards. The chaotic region originating from the vicinity of the

unstable fixed point is still not visible, and the phase space is still dominated by regular motion. With $\epsilon = 0.05$, a thin layer of chaotic region emerges as was shown in figure 3.8. Figure 3.10(c) shows the phase space with $\epsilon = 0.07$, where the chaotic region has expanded to occupy a larger area in the phase space. The chaotic region pushes the ICs towards the extreme values of $|\sin\chi|$ and causes them to disintegrate into islands. There are more islands now that envelope the fixed points than there are ICs with a continuous values of s.

With $\epsilon = 0.09$, the chaotic region have expanded substantially and occupy a larger area of the phase space than regular regions. Even the islands have started to shrink and degenerate into the chaotic region, and there are no ICs that span for all s. The regular region and the chaotic region in the phase space for $\epsilon = 0.12$ were shown in figures 3.9(a) and 3.9(b) respectively. They further confirm the trend of increasing deformation resulting in an expansion of the chaotic region by the degeneration of regular region in the phase spaces.

3.3 Chapter summary

In this chapter, the fibre cross-sectional boundary was modelled using quadrupolar equation, where the deformation parameter, ϵ was used to produce smooth deformations in the fibre boundary. Light distribution in the fibre cross-section was modelled as a ray-billiard system, and the 2D phase space was constructed to monitor ray movement inside the boundary after each reflection. The deformations in the fibre boundary allowed some rays to take chaotic paths, while others remained in various types of regular motion. These paths can be distinguished from each other in the constructed 2D phase space.

Various mixed phase spaces using the quadrupolar boundary distortions have been investigated in this chapter. The various phase space patterns of the deformed boundary were related to their corresponding paths inside the boundary. The chaotic region is formed by rays having random momenta in the phase space and occupies a 2D region of the phase

space with a finite area. This area expands as the boundary deformation increases. The regular regions are confined to 1D fixed points and invariant curves (ICs) for periodic and quasi-periodic trajectories respectively and some sub-set of these regular motions form islands embedded in the chaotic sea. The regular regions in the mixed phase space diminish as the boundary deformation increases.

In the following chapter, the finite operator model will be developed based on coarse-graining mixed phase spaces. The operator model provides a more efficient way of tracking a large number of rays inside the cross-sectional boundary for many reflections than brute force ray-tracing. The finite operator model will also enable the propagation of rays in 3D in both unstructured and step index fibres.

Chapter 4

The finite operator model

4.1 Introduction

In this chapter, a finite operator model is developed that is able to efficiently propagate light through deformed optical fibres. The model is a more numerically efficient method of ray-tracing, where a light distribution can be tracked after each reflection as it propagates along the fibre, and for a large number of reflections. The model is applied, in this chapter, to unstructured fibres with both circular and deformed cross-sectional boundaries. In chapter 5, the finite operator model developed here is extended to deformed step index fibres.

4.2 Formation of the light propagating operator

In this section, an operator method based on ray-dynamical method is developed to propagate light in deformed optical fibres. The formulation discussed here describes how the analysis of a light distribution propagating in the fibre in 3D can be reduced to a 2D cross-section of the fibre, so that it can be represented in the phase space. The propagation of the light can then be visualised as an evolution of an intensity distribution in the phase

space. In this chapter, the analysis is developed for deformed unstructured fibres but the operator method can equally be applied to circular or deformed step index fibres as will be discussed in chapter 5, and 7.

In this section, 3D rays are propagated using the phase space transport, and for now, only a single boundary of the unstructured fibre is sufficient. Let the direction vector of a ray be given by normalized Cartesian components p_x, p_y, and p_z, and let the axis of the fibre be along the z-axis. Rays are confined in the fibre by total internal reflection (TIR) above a certain value of p_z, and so the outer boundary can be treated as perfectly reflecting (ignoring evanescent fields in this ray analysis). Figure 4.1 shows a three-dimensional ray path in the fibre cavity, which travels a distance of Δz along the z-axis and traverses a distance of l_{2D} in the cross-sectional plane. Here,

$$p_z = \cos\theta, \tag{4.1}$$

and above the critical incident angle, θ_{critical}, the rays are confined in the fibre by TIR. Let another unit vector, $\hat{\mathbf{p}}$, be defined in the cross-sectional plane of the fibre which represents the transverse component of the 3D ray. The momentum of the ray in 2D when it hits the boundary is then defined as

$$p = \hat{t}.\hat{\mathbf{p}} = \sin\chi. \tag{4.2}$$

3D ray dynamics in any circular or deformed optical fibre can be simplified to the analysis of 2D phase space transport, as shall now be described.

Let a power distribution of a beam of light arriving directly from the input face of the fibre to the curved boundary be denoted by

$$f_0(s, p, z, p_z), \tag{4.3}$$

where $f_0 = 0$ for $z < 0$. Let

$$(s, p) \to \varphi(s, p) \tag{4.4}$$

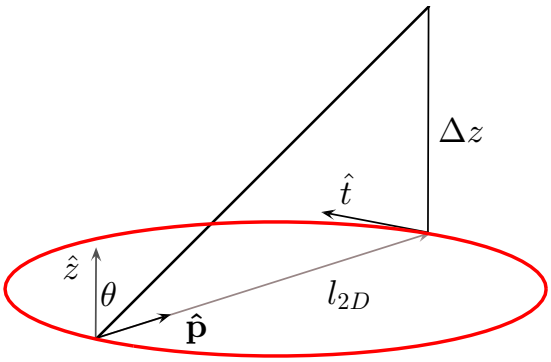


Figure 4.1: A ray in 3D in an unstructured fibre. The ray makes an angle of θ with the z-axis and travels a distance of Δz along the fibre after one bounce. $\hat{\mathbf{p}}$ is a vector along the direction of the 2D component of the ray and $\hat{t}$ denotes an unit vector tangential to the boundary.

be a transformation of the phase space coordinates after tracing a ray for one reflection. The four variable phase space mapping from one boundary point to the next, between m^{th} and $(m+1)^{th}$ reflection, is given by

$$\begin{pmatrix} (s_m, p_m) \\ z_m \\ (p_z)_m \end{pmatrix} \rightarrow \begin{pmatrix} (s_{m+1}, p_{m+1}) \\ z_{m+1} \\ (p_z)_{m+1} \end{pmatrix} = \begin{pmatrix} \varphi(s_m, p_m) \\ z_m + \Delta z(s_{m+1}, p_{m+1}) \\ (p_z)_m \end{pmatrix}. \tag{4.5}$$

p_z is conserved between each reflection, and the dynamics along the z-axis is trivial. Between each reflection, z changes according to

$$\Delta z(s,p) = \frac{p_z}{\sqrt{1-p_z^2}} l_{2D}(s,p). \tag{4.6}$$

where, $\Delta z(s,p)$ is related to the 2D chord length l_{2D} traversed by the rays in between reflections, as shown in figure 4.1. As a result, the power distribution function evolve according to

$$f_{m+1}(s,p,z,p_z) = f_m(\varphi^{-1}(s,p), z - \Delta z(s,p), p_z). \tag{4.7}$$

Since the p_z component is conserved between reflections, it is henceforth suppressed in the notation. An operator, called the Frobenius-Perron operator (FPO), T_{3D}, acting on

f_m would, in 3D, simply map the distribution as

$$f_{m+1}(s,p,z) = T_{3D} f_m(s,p,z), \tag{4.8}$$

where T_{3D}, acting on an arbitrary function $g(s,p,z)$, is defined by

$$T_{3D} g(s,p,z) = g(\varphi^{-1}(s,p), z - \Delta z(s,p)). \tag{4.9}$$

For each (s,p,z) on the 3D fibre curved surface, there is a unique path starting from the $z = 0$ cross-section and having a fixed number of reflections. This enables a way to estimate the long-term light distribution as propagated in the fibre by simply analysing a 2D distribution for a constant p_z value. A Laplace transformation is applied on equation 4.8, to exploit the trivial relationship between z and p_z. The Laplace transform is chosen over the Fourier Transform because the light distribution is initiated from $z = 0$ plane, and the problem becomes akin to an initial value problem. Also, the formulation described here is equally applicable to light propagation when gain or loss media are included. Although, only passive optical fibres are dealt with in this thesis, the method can also be applied to optical fibres with gain.

The Laplace transform of $f_m(s,p,z)$ is defined as

$$\mathcal{L}\{f_m(s,p,z)\} = \int_{z=0}^{\infty} e^{-\beta z} f_m(s,\bar{p},z) dz, \tag{4.10}$$

and the transformation applied to equation (4.8) is given by

$$\mathcal{L}\{T_{3D} f_m(s,p,z)\} \equiv \bar{T}_{3D} \bar{f}_m(s,p,\beta). \tag{4.11}$$

Using the shifting theorem, we get

$$\bar{T}_{3D} \bar{f}_m(s,p,\beta) = e^{-\beta \Delta z(s,p)} \bar{f}_m(\varphi^{-1}(s,p),\beta). \tag{4.12}$$

Let, a 2D transfer operator $\bar{T}_{2D}$ be defined, so that $\bar{T}_{2D}$ operating on an arbitrary 2D

phase space distribution $h(s, \bar{p})$ is given by

$$\bar{T}_{2D}.h(s,p) = h(\varphi^{-1}(s,p)). \tag{4.13}$$

Therefore, equation 4.12 is now expressed as

$$\bar{T}_{3D}\bar{f}_m(s,p,\beta) = e^{-\beta\Delta z(s,p)}\bar{T}_{2D}\bar{f}_m(s,p,\beta), \tag{4.14}$$

where

$$\bar{T}_{3D} = e^{-\beta\Delta z(s,p)}\bar{T}_{2D}. \tag{4.15}$$

Equation 4.15 enables a linear correspondence between the light distribution in 3D with its 2D components. $\bar{T}_{2D}$ is independent of β, and it operates only on a 2D cross-sectional component of the 3D light distribution that can be analysed in the phase space. Along the z-axis, the behaviour of $\bar{f}_m$ for $\beta \to 0$ in the Laplace domain provides information about the behaviour of f_m for $z \to \infty$.

Therefore, the cross-sectional phase space analysis of the 3D fibre is sufficient to model the propagation of the light distribution with the help of $\bar{T}_{2D}$, and measuring the corresponding distance of propagation, Δz, after each reflection at particular p_z. However, $\bar{T}_{2D}$ is an infinite dimensional operator. So, in order to propagate light using this method, a discretization scheme is developed in the phase space to turn $\bar{T}_{2D}$ into a finite operator, as will be discussed in section 4.3. This is a more efficient alternative to 'brute force' ray-tracing, because the formation of the discretized finite operator only requires ray-tracing for one reflection. Once the mapping of all possible trajectories is done in the phase space for one reflection, the operator, $\bar{T}_{3D}$, can be applied to a light distribution iteratively to obtain the distribution for all subsequent reflections.

4.3 The pixelation of the phase space

The finite operator is obtained by the pixelation of the phase space. The phase space of the enclosure defined by the quadrupolar equation was investigated in chapter 3. The deformation parameter, ϵ, was used to smoothly deform the boundary. The quadrupolar boundary models the 2D cross-sectional boundary of an unstructured fibre. In this section, the phase space is coarse-grained to form the finite 2D operator, $\bar{T}_{2D}$. The pixelation scheme converts the process of tracing individual rays into mapping of a flow of power from one region of the phase space (a pixel) to another. The process of mapping of power is performed using an *ensemble* of rays.

The 2D phase space is divided into pixels and transformed into an intensity map. Since the boundary is perfectly reflecting for all values of p_z considered (i.e. those for which TIR occurs), the total power in the system remains unchanged. The number of rays incident upon a particular pixel determine its light intensity. When the phase space is pixelated, rays in an ensemble, uniformly distributed in each pixel, are traced simultaneously until they hit the boundary again. The transfer of intensity from one pixel to the next is obtained by calculating the fractional power in the rays of the initial ensemble that are now incident over multiple other pixels in the phase space. The fractional powers indicate the mapping probabilities from one pixel to the next after a reflection, and form discrete probability distributions arranged columnwise in the $\bar{T}_{2D}$ matrix. These discretised probability distributions are also called Markov chains (as the phase space is a representation of all possible states, in terms of position and momentum, of a classical ray distribution) [87], and will be discussed further in the following subsection.

The pixelation is done as a first step towards optimising the process of ray tracing in the phase space. When the phase space is pixelated, and the mapping probabilities from one pixel to the next are calculated by ray tracing for the first reflection, all the subsequent reflections can be predicted using those mapping probabilities, without the need to trace rays beyond the first reflection.

The phase space is mixed, and so the one dimensional regular invariant curves (ICs) in it can only be approximated with a finite resolution. As the area of the pixel decreases, the resolution with which the phase space patterns can be discerned increases. However, there are some pixelation artefacts introduced, notably in the form of diffusion, which can be diminished, but not eliminated, when the area of the pixel approaches the limit of zero. Due to diffusion, the chaotic region and the regular regions in the pixelated phase space can interact. In ray tracing, the initial condition of a ray in the phase space determines its motion as either quasi-periodic or chaotic, and the two regions can never overlap. In the pixelated version, there are a range of initial conditions chosen from each pixel and they may result in either chaotic or period motion or both. The ability to distinguish between them diminishes at sub-pixel level. Therefore, the intensity of pixel may overlap both regular and chaotic regions of the phase space.

The pixelation is done to make more efficient the simulation of evolution of intensity distribution around the boundary of the fibre for many reflections, through the formation of finite dimensional $\bar{T}_{2D}$. The phase space is coarse-grained in this way to allow the development of a numerically efficient algorithm that can produce a smooth intensity distribution. An investigation is done on the variation in the intensities depicted in the phase with the area of the mapping pixels. The evolution of the pixelated intensity map is observed and compared with that of the 'brute-force' ray-traced version to see the effects of diffusion. As long as a fine coarse graining is used, it is shown that the diffusion artefacts can be kept minimal for a few hundreds of reflections, and fortunately, it is found that the intensity distribution reaches a steady state distribution within this window.

4.3.1 Calculation of the 2D finite operator

In this subsection, the construction of the two dimensional finite operator is described by using a very crudely pixelated phase space of an unstructured fibre cross-section. The cross-sectional boundary of the fibre is defined here, for instance, by the quadrupolar equation given by equation 3.2 with $\epsilon = 0.05$. Rays are traced inside this boundary and

the power transferred by the rays around the boundary is represented in the pixelated phase space as an intensity distribution. The 2D finite operator, $\bar{T}_{2D}$, contains all the probabilities of power being deterministically transferred from each pixel to the next for one reflection.

When the area of a phase space is divided into $N \times N$ pixels, it results in a finite operator, $\bar{T}_{2D}$, in the form of a $N^2 \times N^2$ dimensional matrix. Entries in a column of this matrix are probabilities of mapping power from a corresponding pixel. The procedure to calculate the discrete mapping probabilities, or Markov chain, from a given pixel and subsequently forming a column of the $\bar{T}_{2D}$ matrix is described here, using a very coarse-grained phase space with $N = 5$. In the actual modelling, described in the following subsection and subsequent chapters, the phase spaces have finer pixelations with much higher values of N.

The phase space with 5×5 pixels is shown in figure 4.2. In order to obtain a Markov chain for a particular pixel, let, for instance, a pixel in row 4 and column 3 in this phase space be initialised. A set of 100 rays, uniformly distributed in this pixel, are initiated and traced for one reflection. The points are registered in the phase space again when they hit the boundary after one reflection. The points are first converted to rays at the boundary as shown in figure 4.3(a), and there are 10 ray positions corresponding to 10 s values as each position has rays going in 10 different directions. The rays are then traced to the next point of reflection as shown in figure 4.3(b) and 4.3(c) and the new position and momentum of the rays are registered in the phase space. The rays in the same phase space after one reflection are shown in figure 4.3(d).

As shown in figure 4.3(d), the rays from the initial pixel have now spread to other pixels in the phase space after a reflection at the boundary. The number of rays that landed in each pixel after the reflection are counted and given as a fraction of the total number of rays traced. If the total power among the initialised rays is equal to one, then the fractions represent the power incident at each pixel after one reflection. These fractions also signify the mapping probabilities of the initialised pixel. The process of calculating

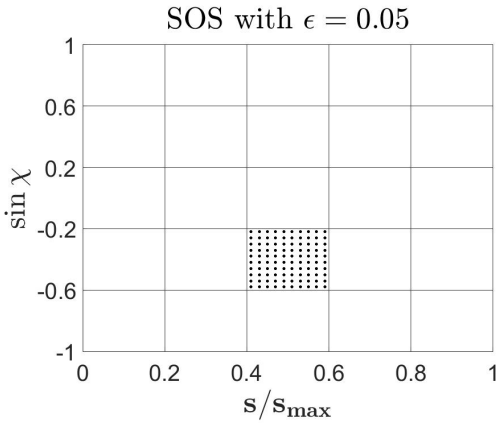


Figure 4.2: A phase space of the cross-sectional boundary of an unstructured fibre is divided into 5×5 pixels. The pixel with row 4 and column 3 is initialised with a uniform set of 10×10 rays. These rays are traced deterministically to determine the probabilities of power being transferred from this pixel to other pixels after one reflection.

the mapping probabilities is described as follows.

Figure 4.2 shows a pixel initialised in a 5×5 pixelated phase space. Let the total power initialised among the rays add up to 1. The rays form an ensemble and take the shape of the rectangular pixel. In matrix form, representing the phase space in figure 4.2, the power distribution amongst the pixels is given by

$$\begin{bmatrix} 0 & 0 & 0 & 0 & 0 \\ 0 & 0 & 0 & 0 & 0 \\ 0 & 0 & 0 & 0 & 0 \\ 0 & 0 & 1 & 0 & 0 \\ 0 & 0 & 0 & 0 & 0 \end{bmatrix}. \tag{4.16}$$

After ray tracing, the rectangular ray bundle scatters, and redistributes among other pixels in the phase space. Again, in a matrix form representing the phase space shown in

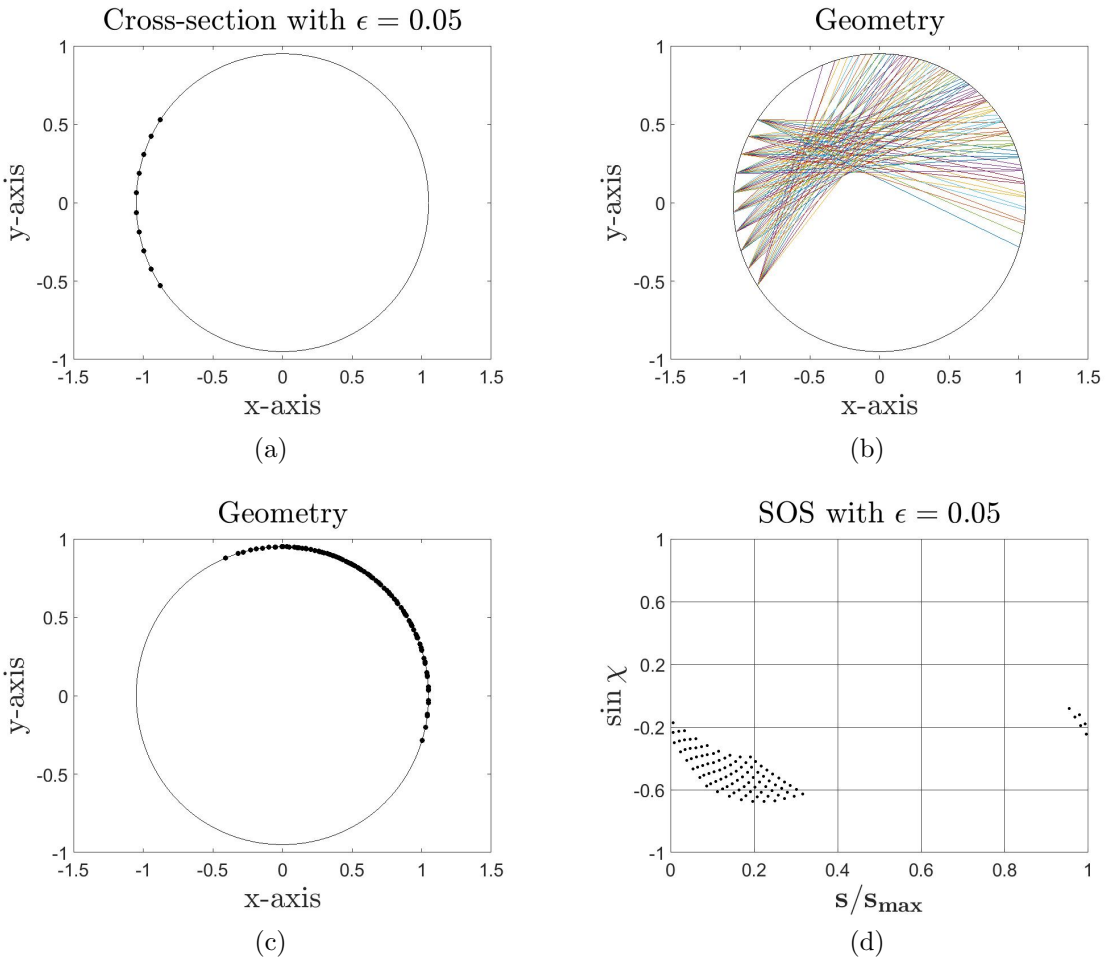


Figure 4.3: Transfer of phase space points after 1 reflection of rays. (a) Phase space points in figure 4.2 is converted into rays at the boundary. These are the starting points for ray tracing and each position contains 10 rays heading in different directions. (b) Ray tracing each initial ray until it reflects again at the boundary.(c) The positions where the rays have ended up at the boundary again after one reflection. (d) The new phase space after one reflection of the rays from the pixel.

figure 4.3(d), the power distribution among the pixels after a reflection becomes

$$\begin{bmatrix} 0 & 0 & 0 & 0 & 0 \\ 0 & 0 & 0 & 0 & 0 \\ 0.01 & 0 & 0 & 0 & 0.05 \\ 0.58 & 0.16 & 0 & 0 & 0.01 \\ 0.08 & 0.11 & 0 & 0 & 0 \end{bmatrix}. \tag{4.17}$$

The matrices 4.16 and 4.17 rearranged in a vector form become Markov chains. This point-to-point probability mapping is called the Ulam's method [67]. The approach was reported recently by Kullig *et al* [80], but was being developed independently by the author during the period of this PhD. The $\bar{T}_{2D}$ stores such Markov chains column-wise.

To describe the column-wise arrangement of individual Markov chains, a simple pixelated phase space, with $N = 2$, is again taken. The resulting phase space now only has four pixels. Let the first pixel in the phase space be populated with an arbitrary number of initial conditions (a rectangular array of ray positions and momenta). Let, the resulting Markov chain be denoted by the vector $\bar{g}_0^1$ and it lists the initial the power/probability distribution of the phase space. It is given by

$$\bar{g}_0^1 = \begin{pmatrix} 1 \\ 0 \\ 0 \\ 0 \end{pmatrix} \tag{4.18}$$

where, the subscript of $\bar{g}$ denotes the reflection number, and the superscript denotes the index of the pixel.

$\bar{T}_{2D}$ operating on any Markov chain, or a general distribution, $\bar{f}_0$, produces a new distribution $\bar{f}_1$ after one reflection. This iterative process can be written as

$$\bar{f}_1 = \bar{T}_{2D}\bar{f}_0. \tag{4.19}$$

.

The $\bar{T}_{2D}$ would redistribute the power and result in a new vector $\bar{g}_1^1$, which is given by

$$\bar{g}_1^1 = \bar{T}_{2D}.\bar{g}_0^1 = \begin{pmatrix} 0.1825 \\ 0 \\ 0.8175 \\ 0 \end{pmatrix}. \tag{4.20}$$

Likewise, populating the second pixel in the phase space and ray-tracing for a reflection yields $\bar{g}_1^2$ from $\bar{g}_0^2$, where $\bar{g}_0^2$ is given by

$$\bar{g}_0^2 = \begin{pmatrix} 0 \\ 1 \\ 0 \\ 0 \end{pmatrix}. \tag{4.21}$$

The $\bar{T}_{2D}$-matrix redistributes the power to generate $\bar{g}_1^2$ given by

$$\bar{g}_1^2 = \bar{T}_{2D}.\bar{g}_0^2 = \begin{pmatrix} 0 \\ 0 \\ 1 \\ 0 \end{pmatrix}. \tag{4.22}$$

The process is repeated for all the pixels in the phase space and the generated vectors in the form of Markov chains arranged column-wise gives

$$\begin{pmatrix} \bar{g}_1^1 & \bar{g}_1^2 & \bar{g}_1^3 & \bar{g}_1^4 \end{pmatrix} = \bar{T}_{2D}. \begin{pmatrix} 1 & 0 & 0 & 0 \\ 0 & 1 & 0 & 0 \\ 0 & 0 & 1 & 0 \\ 0 & 0 & 0 & 1 \end{pmatrix} = \begin{pmatrix} 0.1825 & 0 & 0.8125 & 0.08 \\ 0 & 0 & 0 & 0 \\ 0.8175 & 1 & 0.1875 & 0.92 \\ 0 & 0 & 0 & 0 \end{pmatrix}. \tag{4.23}$$

The set of $\bar{g}_0^i$ vectors concatenated together is an identity matrix and the matrix multi-

plication with an identity matrix is the matrix itself. Therefore, $\bar{T}_{2D}$ for a 2×2 pixelated phase space is given by

$$\bar{T}_{2D} = \begin{pmatrix} 0.1825 & 0 & 0.8125 & 0.08 \\ 0 & 0 & 0 & 0 \\ 0.8175 & 1 & 0.1875 & 0.92 \\ 0 & 0 & 0 & 0 \end{pmatrix}. \tag{4.24}$$

In general, the mapping probability t_{ij} of power from the j^{th} pixel to one of the i^{th} spread pixel in a $N \times N$ pixelated phase space is given by

$$t_{ij} = \frac{\mu(I_j \cap \varphi^{-1}(I_i))}{\mu(I_j)}, \tag{4.25}$$

where $\mu(I_j)$ is the power contained in the j^{th} pixel. The mapping probabilities from each pixel are arranged in the form of a Markov chain, and the concatenated chains form the columns of $\bar{T}_{2D}$ such that

$$\bar{T}_{2D} = \begin{pmatrix} . & \cdots & t_{1j} & \cdots & . \\ \vdots & \cdots & \vdots & \cdots & \vdots \\ t_{i1} & \cdots & t_{ij} & \cdots & t_{iN^2} \\ \vdots & \cdots & \vdots & \cdots & \vdots \\ . & \cdots & t_{N^2 j} & \cdots & . \end{pmatrix}_{N^2 \times N^2.} \tag{4.26}$$

After the formation of $\bar{T}_{2D}$, any arbitrary distribution in the pixelated phase space can be propagated for any number of reflections by applying the $\bar{T}_{2D}$ iteratively on the distribution. Raising $\bar{T}_{2D}$ to the m^{th} power and applying it on an initial distribution yields the distribution in the phase space *after m reflections*. This process is represented as

$$\bar{f}_m = \bar{T}_{2D}^m . \bar{f}_0 \tag{4.27}$$

This approach provides an efficient method to find the ray distribution without using

ray-tracing beyond the first reflection.

4.3.2 Eigen-analysis of the finite operator

Once the finite $\bar{T}_{2D}$ matrix is formed using the pixelated phase space, it can be analysed to investigate the model of propagating a light distribution with it. For the investigation, a 300×300 pixelated phase space is chosen for a cross-sectional boundary defined by the quadrupolar equation 3.2 with $\epsilon = 0.11$. A $N^2 \times N^2$ dimensional T-matrix, with $N = 300$, was formed and its eigen-analysis was performed. The complete set of $l = N^2$ eigenvalues and the eigenvectors of the matrix can be calculated by MATLAB's in-built function 'eig()' which returns three matrices, V,D, and W.

$$\begin{bmatrix} V & D & W \end{bmatrix} = \text{eig}(\bar{T}_{2D}) \tag{4.28}$$

where, V is a matrix consisting of columns of the right eigenvectors of $\bar{T}_{2D}$, W is likewise the matrix of the set of left eigenvectors, and D is a diagonal matrix with eigenvalues of the matrix along its diagonal. Usually, the eigenvalues in D are not sorted in the descending order of magnitude when eig() is called. So D was subsequently sorted with the 'sort()' function to create the matrix D_s where

$$D_s = \text{sort}(D,'\,\text{descend}') \tag{4.29}$$

so that $\lambda_0 > \lambda_1 > ... > \lambda_l$, and the matrix is in the form

$$D_s = \begin{bmatrix} \lambda_0 & 0 & . & . \\ 0 & \lambda_1 & . & . \\ . & . & . & . \\ . & . & . & \lambda_l \end{bmatrix}. \tag{4.30}$$

The left and right eigenvectors can also be sorted accordingly, and their dot product gives a diagonal matrix A given by

$$A = W^T.V = \begin{bmatrix} a_0 & . & . & . & . \\ . & a_1 & . & . & . \\ . & . & a_2 & . & . \\ . & . & . & . & . \\ . & . & . & . & a_l \end{bmatrix}. \tag{4.31}$$

The diagonal values of A can be used to scale either the left or right eigenvectors so that their corresponding dot product is equal to 1, i.e. the left and right eigenvectors now form orthonormal pairs. Here, the right eigenvector V is scaled with the diagonal values of A to get V_{scaled} so that

$$V_{\text{scaled}} W^T = W^T V_{\text{scaled}} = I \tag{4.32}$$

where I is an identity matrix.

The $\bar{T}_{2D}$ entries are sparse, and the numerical eigen-decomposition becomes more computationally burdensome as the size of the matrix grows with the use of smaller pixel sizes. The MATLAB function 'eigs()' is used instead to calculate on the largest few eigenvalues and eigenvectors using in-built iterative algorithms. Table 4.1 shows the 20 largest eigenvalues of $\bar{T}_{2D}$, and figure 4.4 illustrates their position in the complex plane. The largest eigenvalue is equal to 1, and so the rest of the eigenvalues can be placed inside a unit circle in the complex plane. The 20 leading eigenvalues of this particular illustrative matrix are all close to 1 in magnitude. There are 9 eigenvalues very close to the leading eigenvalue of 1, as shown by the inset to figure 4.4.

The characteristics of the $\bar{T}_{2D}$ matrix suggest that after a large number of reflections the operated upon light distribution would converge to a scalar multiple of the eigenvector corresponding to the leading eigenvalue. The reason why this is so can be explained by defining the initial light distribution as the sum of components projected towards the

Eigenvalue No.	Value
1	1
2	0.999890343712320
3	0.999841165337592
4	-0.999790923161595
5	0.999723240684048
6	-0.998931451038312
7	0.998889378394276
8	0.997478882194225
9	0.996943060464375
10	0.995952295198011
11	0.995336317309704
12	$-0.000023417335205 + 0.993894382012134i$
13	$-2.34173352053613 \times 10^{-5} - 0.993894382012134i$
14	-0.993814849707936
15	$-0.495775412924573 + 0.858053754867045$
16	$-0.495775412924573 - 0.858053754867045i$
17	$0.495768645163316 + 0.858031790860874i$
18	$0.495768645163316 - 0.858031790860874i$
19	$0.495185670435853 + 0.858069652798561i$
20	$0.495185670435853 - 0.858069652798561i$

Table 4.1: A list of 20 leading eigenvalues for a T-matrix of a pixelated phase space with $N = 300$ of the quadrupolar cross-section with $\epsilon = 0.11$.

eigenvector space of the matrix. The initial distribution projected on the right eigenvector space can therefore be given by

$$\bar{f_0} = \mathrm{c}_0 v_0 + \mathrm{c}_1 v_1 + \mathrm{c}_2 v_2 + ... + \mathrm{c}_l v_l \ , \tag{4.33}$$

so that

$$\bar{f_0} = V.c, \tag{4.34}$$

where, $c = [c_0, c_1, c_2, ..., c_l]$ is a column vector of the coefficients characteristic to $\bar{f_0}$, and v_0, $v_1 ..., v_l$ are the columns of V. The coefficients can be calculated by noting that

$$\bar{f_0} = V_{\text{scaled}}.W^T \bar{f_0}, \tag{4.35}$$

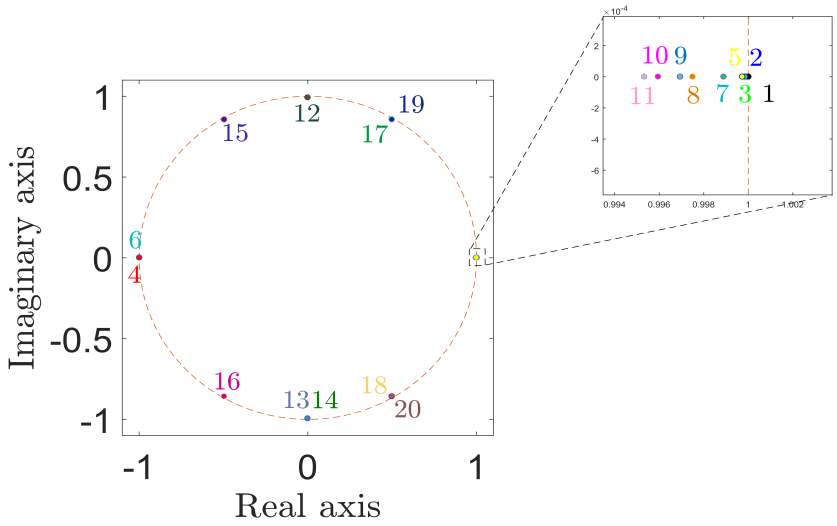


Figure 4.4: 20 largest eigenvalues of the $\bar{T}_{2D}$-matrix for the phase space with $\epsilon = 0.11$

and c is simply defined by

$$c = W^T \bar{f}_0. \tag{4.36}$$

Therefore, f_0 is a linear combination of the scaled right eigenvector

$$\bar{f}_0 = V_{\text{scaled}}.c. \tag{4.37}$$

When the $\bar{T}_{2D}$ matrix is applied on $\bar{f}_0$ for m reflections, the light distribution can be expressed in terms of a linear combination of eigenvalues and eigenvectors of the matrix multiplied with the coefficients c_i of the initial light distribution as

$$\bar{T}_{2D}^m \bar{f}_0 = \mathrm{c}_0 \lambda_0^m v_0 + \mathrm{c}_1 \lambda_1^m v_1 + ... + \mathrm{c}_l \lambda_l^m v_l. \tag{4.38}$$

Except for the largest eigenvalue, all other eigenvalues have a magnitude less than one; so it is apparent from equation 4.38 that eventually in the iterative process only the first term would remain as the value of m increases. Thus, the light distribution reaches a steady state where the final distribution is simply the leading eigenvector of $\bar{T}_{2D}$ scaled by the coefficient of the initial light distribution having a component towards the leading eigenvector. Figure 4.5 shows some of the leading eigenvectors of $\bar{T}_{2D}$ analysed in this section. It is observed that the leading eigenvector of the $\bar{T}_{2D}$ is a uniform distribution in

the phase space. Therefore, it can be deduced that any light distribution propagated by the $\bar{T}_{2D}$ matrix would eventually result in an uniform distribution in the phase space.

The contribution of the other leading eigenvectors is also significant in the evolution of the light distribution, especially for those whose corresponding eigenvalues are very close to 1. These eigenvectors linger in the evolution for many reflections and present their characteristic features of the structures in the phase space, mainly the regular regions. Figure 4.5(b)-(h) reveals some of those regular regions. Figure 4.5(b) shows a thin regular region at the vertical ends of the phase space corresponding to the whispering gallery motion with the boundary. Figure 4.5(c)-(h) shows various eigenvectors that pick up the island patterns characteristic of the particular phase space.

The contributions of the eigenvectors, apart from the leading one, are required to be preserved in the overall propagated light distribution. Thus, the number of reflections undertaken needs to be truncated before the components corresponding to these eigenvectors are extinguished from the evolution during the iterations. An understanding of a suitable truncation point in the evolution needs to be developed. A comparison between a ray-traced pixelated phase space with the finite operator iterated phase space is made in the next section to take a step towards this direction. The following section investigates the effect of decreasing the pixel sizes in order to make the operator iterated phase space more similar to the ray-traced one.

4.4 A comparison of the pixelated phase space with the ray-traced one

The intensity map in the phase space can be produced by ray-tracing as well as by the finite operator method. This provides us a way to compare the distribution between the two processes. The advantage of the operator method is that, after the formation of the matrix, $\bar{T}_{2D}$, it takes very little computational effort to produce the intensity after m

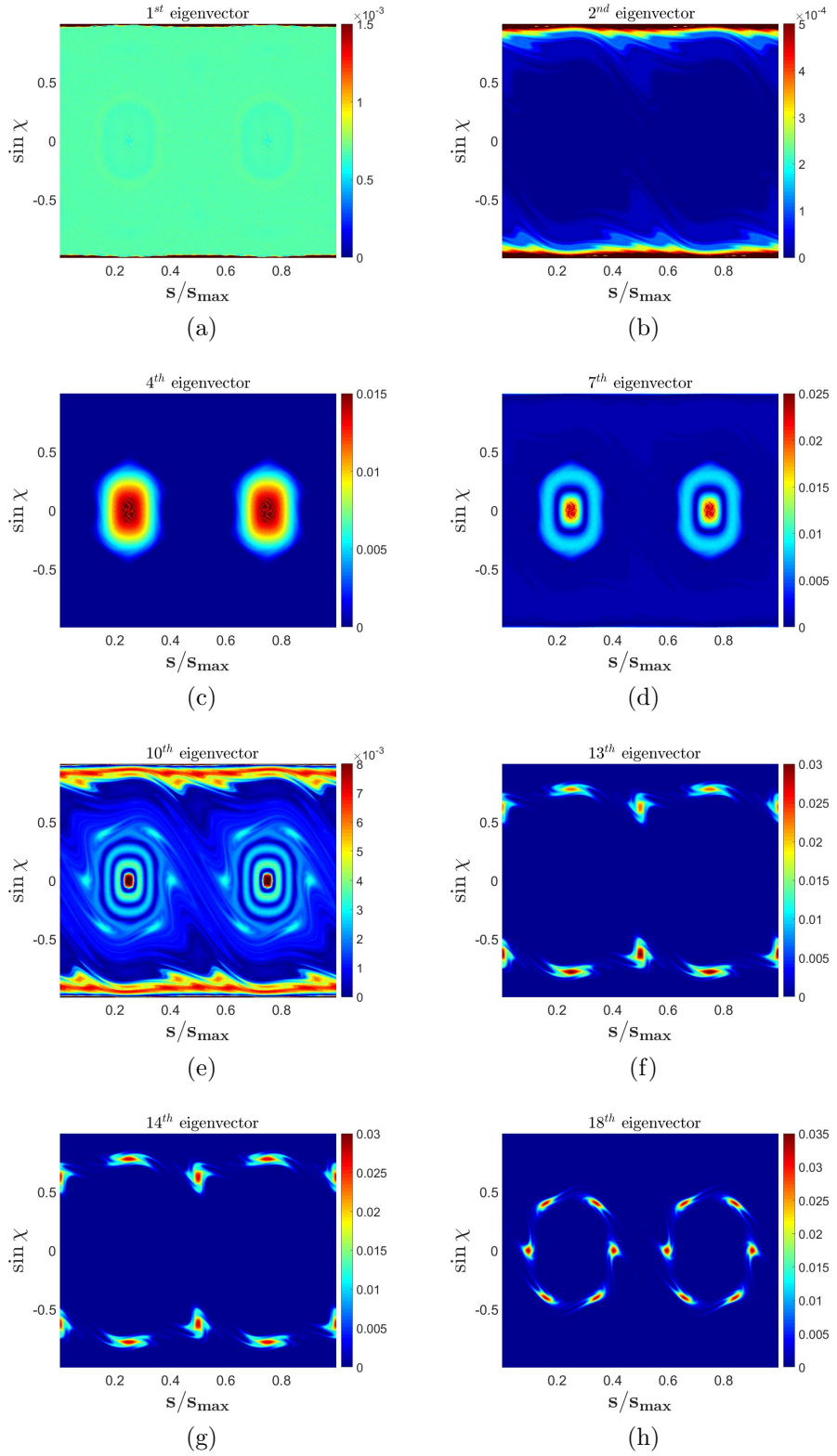


Figure 4.5: Leading eigenvectors of the $\bar{T}_{2D}$ with $\epsilon = 0.11$

number of reflections, where m can be very large. The propagated intensity distribution is smooth and the resolution can be adjusted by altering the individual pixel size. The ray-tracing method is cumbersome owing to the numerical root-solving methods to be applied for each reflection, and because a large number of rays are required. Unless a very large number of rays are traced in the phase space, the resulting intensity distribution tends to be "spiky" owing to inhomogeneous distribution of rays. A large number of initial conditions are required to smooth out the overall distribution as it evolves dynamically in the phase space.

In this section, an investigation is carried out on how the pixel mapping method using the finite operator provides a faithful depiction of the intensity map. The phase space investigated is mixed and consists of 1D regular regions and a 2D chaotic sea. The modelling of the 1D regular regions in the form of invariant curves (ICs) by a 2D rectangular pixel introduces some obvious artefacts. The ray tracing method does not suffer from this problem because each ray is traced from an initial condition and, depending on that condition, a ray will always maintain either regular or chaotic motion in the phase space. When the phase space is pixelated, and subsequently propagated by the FPO method, the power distributed among the pixels can be in both regular and chaotic regions. Hence the intensity leaks between the two regions in a pixelated phase space overlap. This was evident in the characteristics of the constructed $\bar{T}_{2D}$ presented in section 4.3.2 where the leading eigenvector turned out to be a uniform distribution covering the entire phase space. This means that *diffusion* between the integrable and non-integrable regions in the phase space results ultimately in the elimination of the regular regions from the phase space. Therefore, the pixelation artefact creates an upper limit on the number of reflections m that can be made on the basis of the mapping probabilities.

However, the upper limit of m can be increased by reducing the pixel area. This also increases the convergence of the leading eigenvalues close to the unit circle. In this section, the effect of changing the pixel size on the diffusion process is investigated. It is found that the effect of diffusion which occurs as a result of the pixelation artefact can be minimised, and thus the value of m for which the evolution can be observed can be increased.

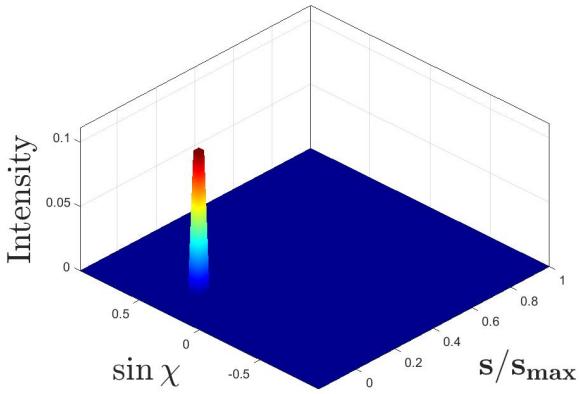


Figure 4.6: Intensity map of an initialised pixel.

4.4.1 Evolution of the intensity from a pixel

In this sub-section, the evolution of intensity originating from a single pixel is investigated and a comparison is made between ray-tracing and the finite operator methods. For the investigation, the phase space for $\epsilon = 0.11$ is chosen, and it is divided into 50×50 pixels; the pixel areas are relatively large and such a coarse pixelation is only used for the illustrative analysis of this sub-section. In an intensity map representation of the phase space, an initialised pixel is shown as in figure 4.6. A pixel in the chaotic region of the phase space is arbitrarily chosen. For the ray-tracing method, the power in the pixel is divided among an ensemble of rays, and for the finite operator method the Markov chain is formed and operated on by the corresponding 2500×2500 $\bar{T}_{2D}$ matrix, as discussed in sub-section 4.3.1.

The distribution is iterated for only a couple of reflections. The first reflection yields, by construction, the same result for both methods. Figure 4.7(a) and (b) shows the rays and the corresponding intensity distribution in the pixels for the first reflection. When the next reflection occurs, the initial conditions after the first reflection are traced again until they hit the boundary in the ray-tracing method. The distribution is then pixelated again to form the second intensity map as shown in figure 4.7(c). In the finite operator method, the Markov is chain formed after the first reflection corresponding to the intensity map

in figure 4.7(b) and is iterated using $\bar{T}_{2D}$ matrix to produce the second distribution, as shown in figure 4.7(d). The finite operator method redistributes the intensity by using the pixel mapping probabilities, whereas the ray-tracing method retraces the same set of rays, specularly reflecting around the boundary, and calculates the fractional power in each pixel based on the number of incident rays. A comparison between figure 4.7(c) and (d) shows that the intensity map of the finite operator method is more spread out than that of the ray-traced method. This trend continues for all the subsequent reflections and after many iterations the intensity map between the two methods may look substantially different.

A 50×50 pixel phase space is rather coarse, and it is re-emphasised that this is only shown to exaggerate the differences in the intensity map between the two methods after only the second reflection. When a finer pixelation is done, the ray-traced and the finite operator map are comparable to each other after a larger number of reflections. Figure 4.8 illustrates this by presenting the intensity map consisting of 300×300 pixels evolved from the same initialisation of a pixel in the chaotic region. The initialised pixel was iterated for 50 reflections by both methods.

Figure 4.8(a) shows the map produced by ray-tracing method and 4.8(b) shows the map produced by the finite operator method. After 50 reflections, the power from a single pixel has spread out almost uniformly to all parts of the chaotic sea, revealing the regular islands embedded in it. Since a pixel in the top-half of the phase space with positive momenta was initialised (corresponding to rays reflecting in a counter-clockwise manner around the boundary), the intensity distribution is brighter there than in the bottom half. The distribution in the chaotic sea produced by ray-tracing is grainy showing a lot of spikes, whereas that produced by the finite operator method is very smooth.

Therefore, some subset of rays follow each other closely for a long time during their evolution in the phase space, while others move further apart during the same time. The result is that the intensity map produced by ray-tracing requires a lot of initial conditions to be included in order to make it smooth. The number of reflections to be observed also

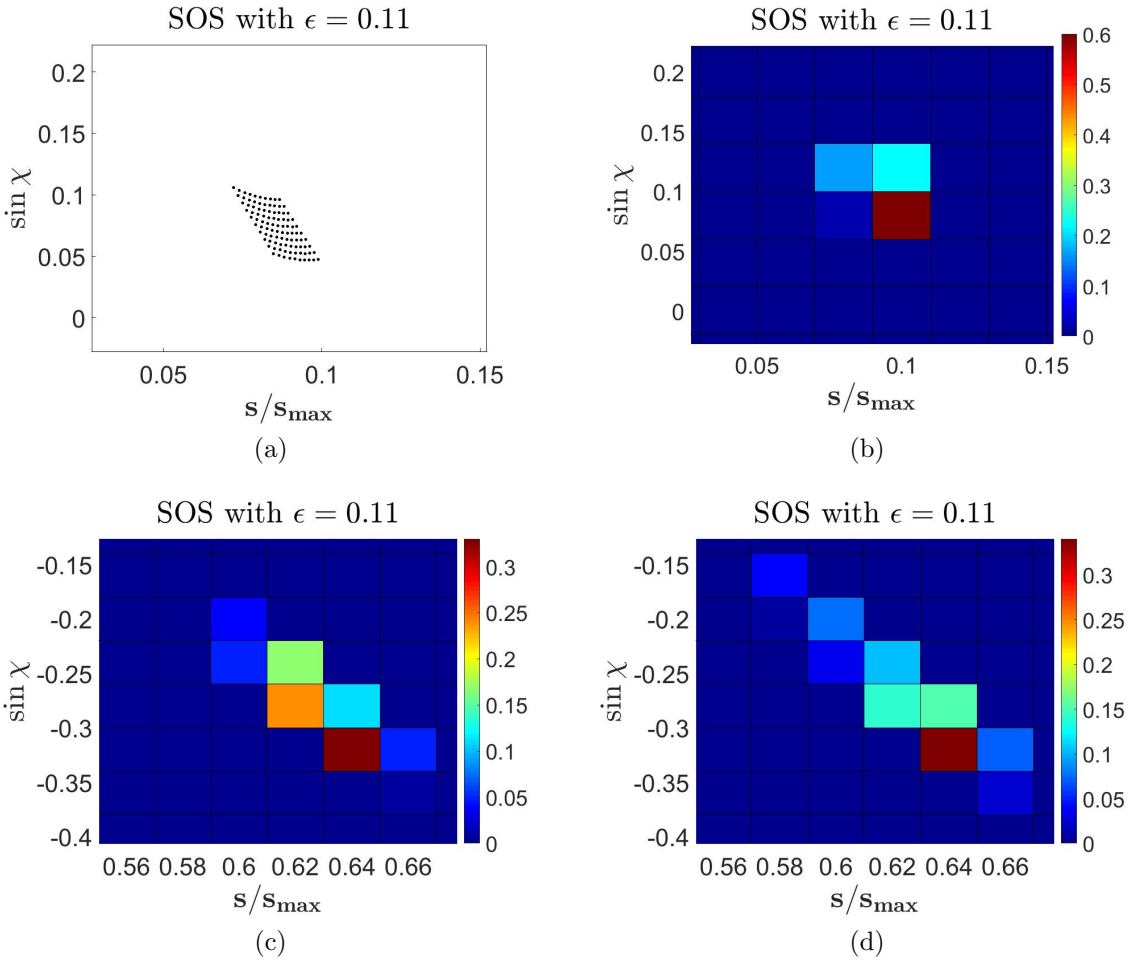


Figure 4.7: **(a)** First iteration of a traced ray ensemble. **(b)** shows the coarse-grained structure where the map is turned into 50×50 pixel array. Due to the finite area of the pixels, the fine structure of the ray ensemble are coarse-grained on the mapped pixels. **(c)** Second iteration of the ray ensemble by tracing individual rays and then forming the pixelated phase space. **(d)** shows the same pixel distribution of (b) propagated twice by the finite operator.

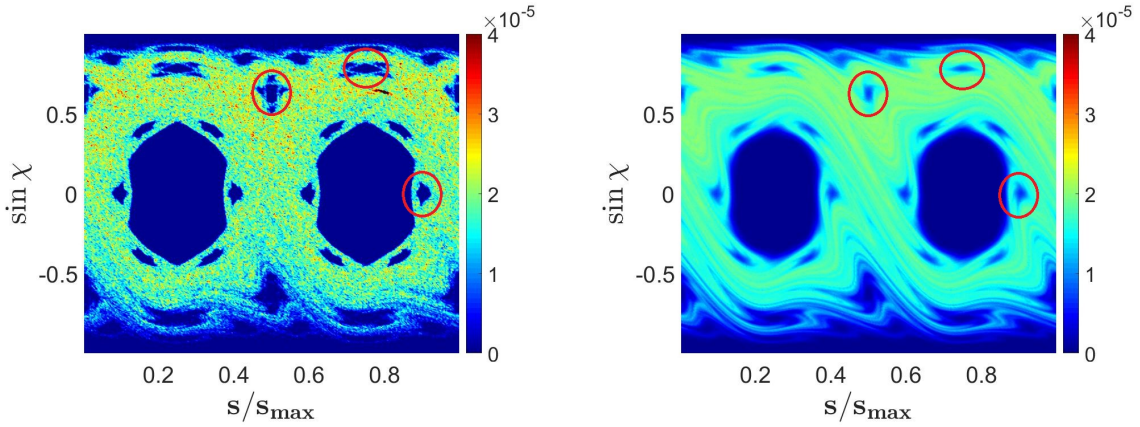


Figure 4.8: Differences are illustrated in the phase space distribution between a ray ensemble traced from a pixel **(a)** and an intensity from the same pixel iterated by the finite operator **(b)** in a boundary defined by the quadrupolar equation with a deformation of $\epsilon = 0.11$. The distribution has evolved from an excited pixel in the chaotic region of the phase space after 50 reflections (in a 300 by 300 pixel phase space). The circles highlight some of the regions where the phase space differ between the two methods.

plays a contributing factor in this choice because, with more reflections the rays are going to spread themselves more uniformly in the chaotic sea and so more initial conditions are required to be included to avoid the graininess. These factors contribute to additional computational effort. Although, the ray-tracing method maintains the separation of rays between integrable and non-integrable regions, the fact that a large number of rays is required in the calculation makes the method numerically very prohibitive. Therefore, the finite operator method is employed where such problems are overcome completely at the cost of diffusion artefacts.

The intensity map produced by the finite operator method is considerably faster to produce numerically. The pixel area is made sufficiently small to minimise the rate of diffusion from the pixelation artefact within the observation window, i.e for the first 50 reflections. The circles in figure 4.8 point out the important difference at the border between the chaotic sea and the regular islands between ray-tracing and the finite operator method. The islands have been partially eroded by the diffusion process, but overall the finite operator method provides a very smooth estimation of the intensity distribution that is not achievable by the ray-tracing method.

4.4.2 Evolution of a Gaussian spot

The previous subsection has shown the evolution of a density originating from a single pixel. A case can now be considered where the rays with unequal weights or power, spread out over multiple pixels, can be be propagated them in the pixelated phase space. In this section, a Gaussian intensity distribution is initialised in the phase space and observed for the same duration of 50 reflections. Also, the Gaussian is arranged to approximately cover a regular island in the phase space. The regular island excited corresponds to $N_p = 4$ in a quadrupolar boundary with $\epsilon = 0.11$, and the trajectories are reflecting in a counter-clockwise manner around the boundary; figure 3.7(c) shows the corresponding motions but in differently deformed boundaries. The diffusion of the intensity out of the regular region in the FPO method is investigated and compared with the ray-traced phase space.

Figure 4.9 shows the intensity map at the 48^{th} reflection when the excited Gaussian spot has circulated around the boundary for 12 times (but observed for up to 50 reflections). The ray-traced version, shown in figure 4.9(a) shows the power in the regular island remaining trapped. In contrast, the map produced by the finite operator, in figure 4.9(b), shows a diffused spot as a result of artefacts inherent the finite operator method. The peak at the fixed point is more diminished and the intensity at the edges has spread more out of the regular island than that in ray-tracing method. The leading eigenvectors of the $\bar{T}_{2D}$-matrix have been investigated in section 4.3.2, and out of the first 20, eigenvectors 12, 13, and 14 correspond to these regular islands; figure 4.5(f) and (g) shows two out of three of the corresponding eigenvectors.

4.4.3 Calculation of the power distribution by altering the pixel area

The power distribution is calculated separately for all pixels/rays reflecting in clockwise (CW) and counter-clockwise (CCW) manners. The CCW section of the phase space consists of all the trajectories having a positive momenta and occupy the top-half of the

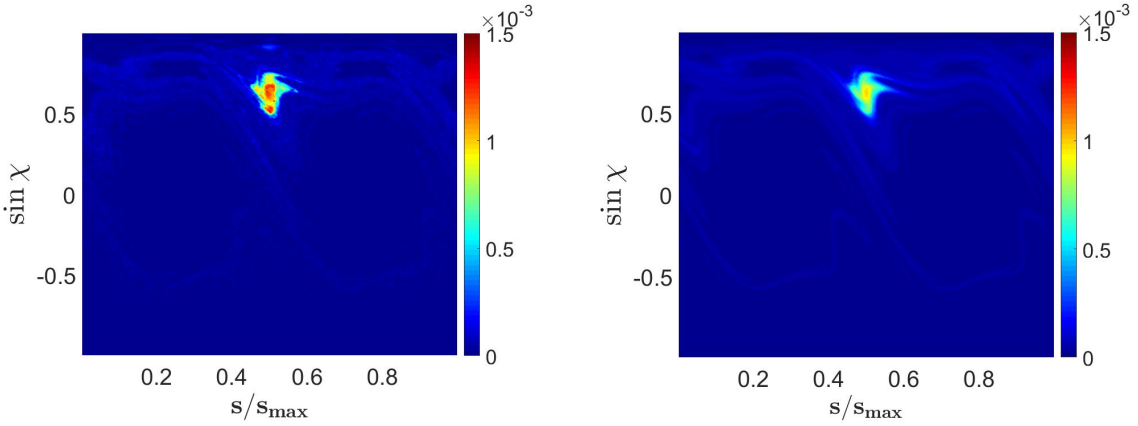


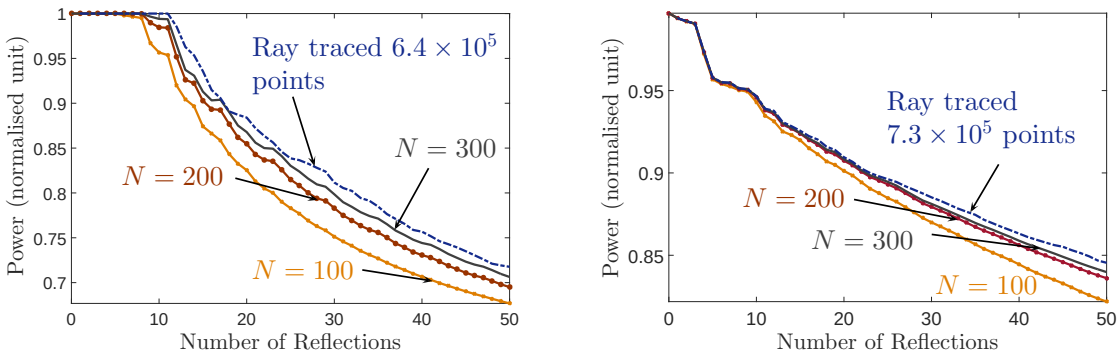
Figure 4.9: Evolution of a Gaussian spot initialised in a regular island with $N_p = 4$ and observed at the 48^{th} reflections in the pixelated phase space. (a) The ray-traced version shows the intensity in the regular region remaining trapped. (b) The version produced by the finite operator method shows the same spot with much of its intensity diminished as a result of diffusion, which is an artefact of the pixelation.

map. A comparison is made between ray-tracing and the FPO method on how much of an excited initial distribution from the CCW region is transferred to the CW region over the number of observed reflections. The cases discussed in section 4.4.1 and 4.4.2 are used to calculate the power in the CCW region. Figure 4.10 shows the resulting plots, where three separate $\bar{T}_{2D}$ matrices with varying pixel sizes are also constructed and compared with the ray-traced result.

Creating finer pixelation in the phase space results in the power in the CCW region calculated using the FPO method to become closer to that of the ray-traced method. Thus as N is increased from 100 to 300, the power distribution follows more closely to the ray-traced curve.

4.5 Chapter summary

In this chapter, the finite operator model was developed for the analysis of light in optical fibres. The 3D finite operator, $\bar{T}_{3D}$, was developed and expressed in terms of its constituent 2D component $\bar{T}_{2D}$, and an exponential factor along the direction of propagation



(a) (b)

Figure 4.10: Total power calculated in the top half of the SOSs after each reflection for the evolution of (a) the initialised pixel in the chaotic sea in figure 4.6, (b) the Gaussian spot discussed in section 4.4.2. The result using brute-force ray-tracing is indicated using dashed line, and the results using the finite operator method is shown by the solid lines. In the latter case, three different sizes of $\bar{T}_{2D}$ have been used with $N = 100, 200,$ & 300 respectively. Ray-tracing allows the power calculation to be made with no diffusive artefacts, and the results using $\bar{T}_{2D}$ indicate lower diffusion as N increases.

containing information about the distance traversed between each reflection. The properties of the $2D$ finite operator were investigated in this chapter using the cross-sectional boundary of an unstructured fibre, and in presence of fibre deformations.

The mixed phase of the deformed unstructured fibre was then coarse-grained to form the 2D finite operator, $\bar{T}_{2D}$. The development of this operator provides an alternative to ray-tracing which produces a smooth intensity distribution in the phase space that is not possible with ray-tracing, although the separation between the regular and chaotic regions in the phase space becomes less distinguishable by this. However, the advantage gained is the ease with which the evolution of any distribution that can be observed for a large number of reflections. The phase space was divided into $N \times N$ pixels and each pixel was then filled with a set of uniform distributed ray ensemble. They were traced numerically and registered again in the phase space after one reflection. The pixel mapping probabilities were calculated by finding the fraction of the rays that landed in each pixel after one reflection. These mapping probabilities were arranged in a Markov chain and the process was repeated for each pixel in the phase space to form the $\bar{T}_{2D}$ matrix. With the help of this, the intensity distribution in the phase space after the subsequent reflections

was evaluated. This helped alleviate the considerable computational burden associated with ray-tracing.

The properties of the constructed finite operator $\bar{T}_{2D}$ were analysed using eigen-decomposition. The largest eigenvalue is equal to one and the leading eigenvector corresponding to this eigenvalue was shown to be a uniform distribution in the phase space. This means that the diffusion process introduced as an artefact of the rectangular pixelation completely engulfs all the features of the mixed phase space. So the iterations by the $\bar{T}_{2D}$ using the mapping probabilities can only provide a finite window, in terms of the number of reflections, in which the evolution can be observed before the pixelation artefacts take over. There are other leading eigenvectors of the matrix that pick up various characteristic features of the phase space and as long as their contributions to the overall evolutionary density is preserved the iterations can be continued.

To highlight the essential differences in the intensity map between ray-tracing and the finite operator model, the two methods were applied using the same initial conditions and the evolution of light was observed for the same number of reflections. It was established that as the pixel area in the operator model was decreased the resulting phase space distribution became more comparable to the ray-traced distribution. In the limit of the pixel area becoming zero, the operator becomes infinite dimensional and the model essentially is indistinguishable from ray-tracing.

In the following chapters, the finite $\bar{T}_{2D}$ is extended for the step index fibre (SIF). The SIF introduces more than one boundary for which the phase space map is required to be constructed. The finite operator method is more suitable for the analysis of the SIF than the ray-tracing method because, in the SIF, the number of rays to be traced increases exponentially after each reflection when traced in presence of a reflecting and refracting in dielectric media. Each time a ray hits the dielectric interface, a reflected ray and a transmitted ray is created and the number of rays required to be traced increases exponentially. This puts a severe limitation on the ray-tracing method. The finite operator model overcomes this limitation as only one reflection is required to calculate the map-

ping probabilities and all subsequent reflections can be calculated without any significant additional computational effort.

Chapter 5

Formation of the pixelated phase space for step-index fibres

5.1 Introduction

In this chapter, the finite operator method is extended to model light propagation in 3D step index fibres (SIF). The finite operator based on the ray-dynamical system was developed in chapter 4 to model light distribution in the phase space of deformed unstructured fibres. The phase space was formed using the cross-sectional boundary of the unstructured fibre. In the case of SIF cross-section, there are multiple core and cladding boundaries. In this chapter, a phase space will be formed for each boundary of the SIF that will show the evolution of a light distribution as it propagates through the SIF. Simply ray-tracing in the SIF with multiple core and cladding dielectric media is very challenging, because each ray hitting the core boundary will multiply in number by two with the formation of a reflected ray and a transmitted ray, and the total number of rays to be traced increases exponentially after each reflection. An example of a ray propagating through a deformed SIF and multiplying in number is shown in figure 5.1. As will be discussed in this chapter, the finite operator model extended for the SIF provides an efficient way of solving this problem.

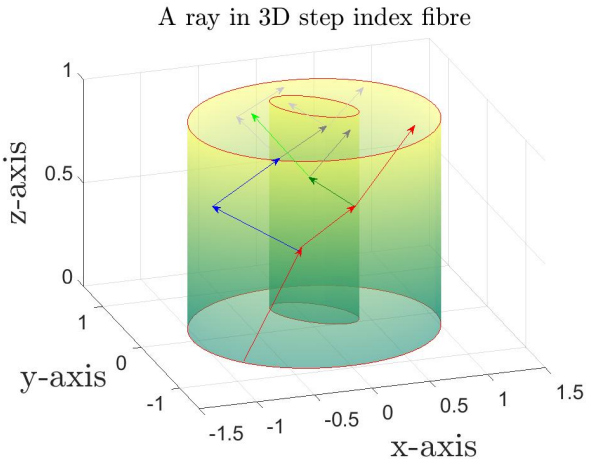


Figure 5.1: Rays modelled in 3D in the step index fibre.

Individually traced rays have no area associated with them in the phase space. So, when constructed by the ray-tracing method, the phase space patterns could potentially be of infinite resolution. In chapter 4, the phase space was coarse-grained and the power transferred from one region in the phase space to another was modelled using pixel-mapping. The phase space was essentially turned into an intensity map of the light that tracked rays at the boundary after each reflection. The resolution of the intensity distribution was determined by the area of each pixel. The finite operator was constructed for evaluating the intensity distribution iteratively as the trajectories reflected inside the fibre boundary. Numerically, this operator is in the form of a matrix denoted by $\bar{T}_{3D}$ which redistributes the intensity in the phase space after each reflection, and whose dimensions increase with finer phase space pixelation. In chapter 4, it was shown that it was also possible to make a 2D operator, $\bar{T}_{2D}$ by separating the 2D cross-sectional components of 3D rays in the fibre. This allowed the light distribution to be visualised in the phase space. In this chapter, the finite $\bar{T}_{2D}$ matrix is constructed for the deformed SIFs. The analysis of the full 3D operator, $\bar{T}_{3D}$, for the SIF will be discussed in chapter 7.

5.2 Representation of 3D rays in the phase space for step index fibres

In this section, the 3D rays are represented in terms of their 2D cross-sectional components in the SIF in order to track their evolution in the phase space while they are propagating along the fibre. In the case of an unstructured fibre in chapter 4, there was only one cross-sectional boundary present and the phase space was formed assuming the boundary was perfectly reflecting. In the SIF, the core has a higher refractive index, n_c, than that of the cladding, n_{cl}, and so light rays in the core medium may also undergo total internal reflections (TIR). In the finite operator model, any arbitrary initial input light distribution, $f_0(s, p, z, p_z)$ is propagated in the SIF for a particular p_z, where p_z is defined in section 4.2, chapter 4. If there is air surrounding the fibre, then the light distribution with $p_z \geq 1/n_{cl}$ will be trapped in the SIF by TIR at the cladding-air interface. The momentum of each ray must be defined in the different propagating media, and in a 3D space. The position of the ray must be tracked using the inward and outward facing core boundaries in addition to the cladding boundary in the SIF. In the following subsection, the momentum and position of the rays are defined again for SIFs.

5.2.1 Representation of position and momentum in 3D

The momentum of a ray is now defined when it is propagating in a medium with a specific refractive index, and is taken on the 2D cross-sectional plane of an optical fibre as shown in figure 5.2. Let, the momentum of a ray propagating in 3D in a medium n_i, and having a direction vector $\bar{\mathbf{p}}_\mathbf{i}$ be denoted by $\bar{p}_i$, where

$$\bar{p}_i = \hat{t}.\bar{\mathbf{p}}_\mathbf{i}, \tag{5.1}$$

$$= n_i \sin\theta \sin\chi, \tag{5.2}$$

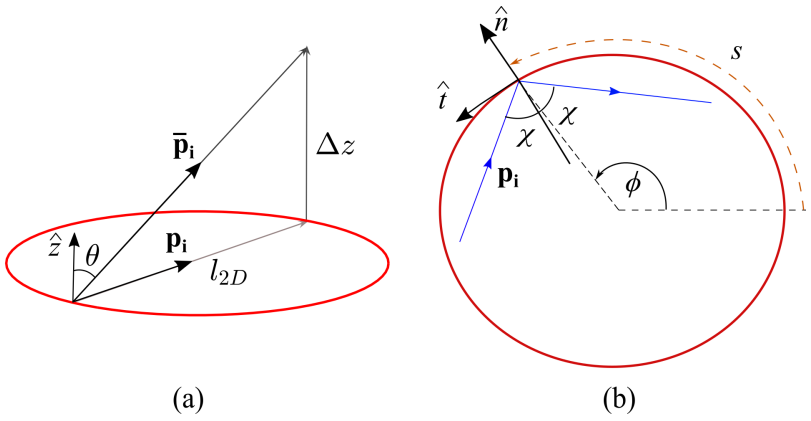


Figure 5.2: 3D rays in the fibre. The momentum of the 3D ray is given by $\bar{p}_i = \hat{t}.\bar{\mathbf{p}}_\mathbf{i}$ in a propagating media with refractive index n_i. For $p_z = 0$, the momentum of the ray is given by $p_i = \hat{t}.\mathbf{p}_\mathbf{i}$.

where the angles (θ, χ), and the unit vector tangential to the boundary $\hat{t}$ are shown in figure 5.2; i denotes either the cladding or core medium in which the ray is propagating. In terms of p_z the momentum of the ray is given by

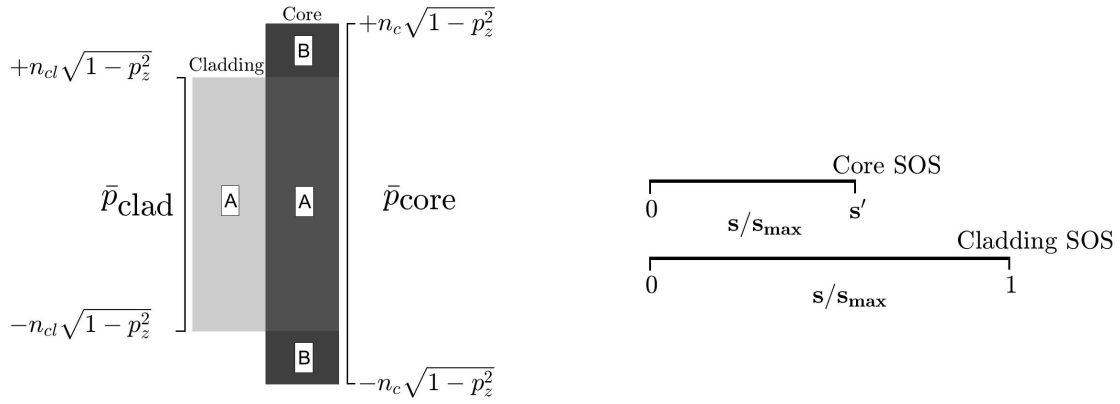
$$\bar{p}_i = n_i \sqrt{1 - p_z^2} \sin \chi. \tag{5.3}$$

At the core-cladding dielectric interface of the SIF, the momentum at the incident medium i is equal to the momentum in the transmitted medium t according to Snell's law, and so

$$\bar{p}_i = \bar{p}_t. \tag{5.4}$$

The component of the momentum in the z-direction, p_z, is also conserved. Figure 5.3(a) shows the range of momentum between the phase spaces to be created between the core and cladding boundary where the value of refractive index scales the range of momentum a ray can have in different propagating media. In the updated notation, in cases where the analysis of the light distribution is limited to the 2D cross-section of the fibre with $p_z = 0$, and only $\bar{T}_{2D}$ is used to propagate the light, the bar notation on the momentum is suppressed and the 2D momentum is simply given by

$$p_i = n_i \sin \chi \tag{5.5}$$



(a) (b)

Figure 5.3: (a) The vertical axis of the phase space distinguishing the momenta of rays between the core and cladding media. The refractive index of the cladding is n_{cl}, which is lower than the refractive index n_c of the core. Rays having a momenta in the regions labelled A are partially reflected and partially transmitted when incident at the core boundary, whereas rays in region B can only exist in the core medium and have momenta that results in total internal reflection upon hitting the core boundary. (b) The horizontal axis of each phase space is normalised with the circumference of the cladding boundary $s_{\max}$; s' is the circumference of core boundary given as a fraction of the circumference of the cladding boundary.

to distinguish from calculations in 3D.

Therefore, the momentum of a ray in the cladding medium and registered in the cladding boundary phase space is denoted by $\bar{p}_{\text{clad}}$. The momentum of a ray that hits the core outward-facing boundary, or the core exterior boundary is still in the cladding medium, and so will still be denoted by $\bar{p}_{\text{clad}}$. In the core medium, any ray that hits the core interior boundary will be denoted by $\bar{p}_{\text{core}}$. Figure 5.3(a) shows the modification of the momentum axes of the phase space for 3D rays in terms of p_z, and n_{cl} and n_c.

In figure 5.3(a), the regions denoted by A are the range of $\bar{p}_{\text{clad}}$ for which the rays are partially reflected and partially transmitted from cladding medium to the core medium and vice versa, and $\bar{p}_{\text{core}} = \bar{p}_{\text{clad}}$. A ray originating from the core medium, upon hitting the core boundary, will be completely reflected if the incident angle χ is greater than the critical angle χ_c. Region B is the range of $|\bar{p}_{\text{core}}|$ for which rays incident at the boundary from the core medium are total internally reflected and cannot reach the cladding medium. The rays in the core medium, having a momentum in the range $n_{cl}\sqrt{1-p_z^2} < \bar{p}_i \leq$

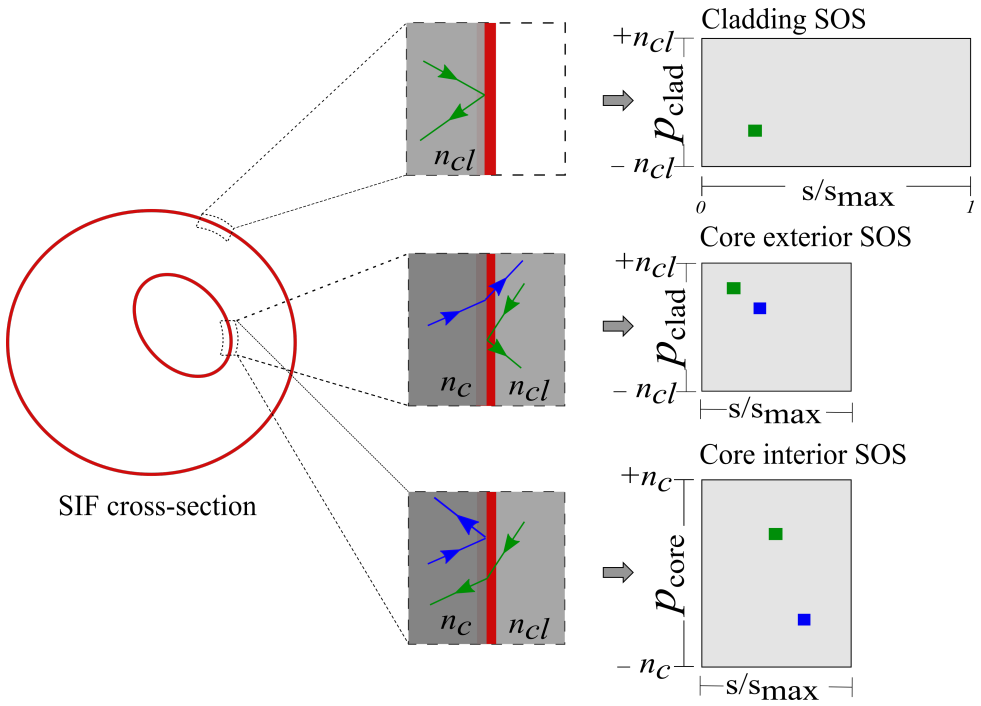


Figure 5.4: Formation of the separate phase spaces for the SIF cross-section with $p_z = 0$. The core refractive index is n_c which is higher than that of the cladding, n_{cl}, so $p_{core} > p_{clad}$. The cladding boundary is assumed to be perfectly reflecting so as to keep the total power in the system invariant.

$n_c\sqrt{1-p_z^2}$, will be total internally reflected. Therefore, separate phase spaces are required for the core exterior boundary in the cladding medium and the core interior boundary in the core medium because the ranges of momenta a ray may have in different dielectric media are different.

The horizontal s-axes of the core phase spaces are different from that for the cladding one owing to the smaller core boundary arc length. Here, the respective arc lengths s of each boundary are represented as a fraction of the circumference of the cladding boundary $s_{\max}$ as shown in figure 5.3(b). The total arc-length of the cladding is normalised to unity, and the circumference of the core as a fraction of that of the cladding is denoted by s'.

Figure 5.4 shows the formation of three different phase spaces for the SIF for $p_z = 0$. The cladding phase space only shows rays being reflected off the the cladding boundary as the total power is assumed to be contained in the fibre. The core exterior phase space shows rays from the cladding medium (green) being reflected off the core boundary and also rays that are transmitted out of the core (blue). The core interior phase space shows rays

transmitted into the core medium from the cladding medium (green), and also rays in the core medium being either partially or totally reflected from the core boundary (blue).

5.2.2 Division of power at the core-cladding interface

A scalar approximation is adopted in order to describe the division of power between the transmitted ray and the reflected ray when one is incident on the core-cladding dielectric boundary. Fresnel's equation for the TE polarisation is used to find the reflectance and transmittance of the rays travelling in and out of the core boundary, and the reflection coefficient is given by

$$r_{TE} = \frac{n_i \cos\chi_i - n_t \cos\chi_t}{n_i \cos\chi_i + n_t \cos\chi_t}, \tag{5.6}$$

where χ_i is the incident angle and χ_t is the angle of transmission. The reflectance, R_{TE}, is obtained by using equation 5.6 and, after simplifying, it is given by

$$R_{TE} = \left|\frac{a-b}{a+b}\right|^2, \tag{5.7}$$

where

$$a = \sqrt{n_i^2 - \sin^2\chi_t - n_t^2 p_z^2(1-\sin\chi_t^2)}, \tag{5.8}$$

$$b = n_t\sqrt{(1-p_z^2)(1-\sin\chi_t^2)}. \tag{5.9}$$

The power in the transmitted ray is obtained using the transmittance and is given by

$$T_{TE} = 1 - R_{TE}\ . \tag{5.10}$$

In the following section, the formation of $\bar{T}_{2D}$ for the SIF is discussed, and during this initial discussion $p_z = 0$ and suppressed, and $p_i = \bar{p}_i$. The discretisation scheme will also be discussed, where each of the three phase spaces of the SIF will be discretised and ray ensembles from each pixel will be traced, similar to the case of unstructured fibre

discussed in chapter 4. The difference is that, ray ensembles from one boundary can now transfer power to the phase space of another boundary, and the total power is spread over all the three phase spaces of the SIF.

5.3 Formation of the coarse-grained phase spaces for step index fibres

In this section, the construction of the finite 2D operator, $\bar{T}_{2D}$, is undertaken by pixelating the phase space. Its formation can be described in a 2D setting, and ignoring the z-directional components of the rays. The columns of $\bar{T}_{2D}$ consist of Markov chains, that calculate the mapping probabilities between one pixel and others. The mapping probabilities are obtained by tracing ray-ensembles from each pixel and from each phase space of the SIF. The rays are assumed to be trapped in the cladding boundary by TIR, and so, only the inward-facing cladding boundary is considered. The core-cladding interface forms a dielectric boundary where rays are partially transmitted and partially reflected. This results in an inward facing and an outward facing core boundary.

Here, the SIF is modelled to have core and cladding refractive indices similar to those as one would find in typical chalcogenide glasses [17]. The core refractive index is chosen to be equal to 2.70, and the cladding refractive index is taken at the slightly lower value of 2.55. Using the ray-tracing method, any general shape of the SIF can be modelled. Therefore, a deformed SIF cross-section is taken, where the core is elliptical and centred at $(0.1, 0.3)$, with $(0.4, 0.2)$ as major and minor axes lengths respectively. In addition, the axis of the core is rotated by a angle of $3\pi/4$. The core is surrounded by the cladding with a quadrupolar boundary defined as in equation 3.1 with $\epsilon = 0.05$. The corresponding cladding phase space was shown in figure 3.8, chapter 3.

The phase space is divided into rectangular grids which serve as pixels when they are transformed into an intensity map as shown in figure 5.5 and 5.6. Each phase space

is crudely divided into 10×10 pixels for the illustrations in this subsection. To form a column of the $\bar{T}_{2D}$ matrix, a ray ensemble originating from the cladding boundary is excited by choosing initial conditions within a pixel in the cladding phase space, as shown in figure 5.5(a). A total of 100 rays is initialised and their initial positions at the cladding boundary are shown in figure 5.5(b). These rays are traced until they hit the boundaries again. In the case of the SIF, rays hit the core boundary as well as the cladding boundary as shown in figure 5.5(c). After a reflection, it is required to form the respective phase spaces and register the rays according to their positions, momenta, and the propagating media. The momentum of a ray in the cladding medium is denoted as p_{clad}, and that in the core medium as p_{core}. The rays hitting the cladding boundary are reflected with the same momentum p_{clad}; this is registered again in the cladding SOS, as shown in figure 5.5(d). The rays that hit the core boundary are partially reflected and partially transmitted. The reflected rays at the core boundary are registered in the core exterior SOS with their momenta denoted by p_{clad} as they remain in the cladding medium, as shown in figure 5.5(e). The transmitted rays have the same positions on the boundary but a different momenta from the reflected rays, and they are registered in the core interior phase space. Their momenta are denoted by p_{core} since they are now in the core medium. Figure 5.5(f) shows the resulting core interior phase space. The momentum in the core interior phase space ranges within $\pm n_{\text{c}}$, whereas that in the core exterior phase space ranges within $\pm n_{\text{cl}}$, but both phase spaces are divided into the same number of pixels.

Notice, that the total number of rays to be traced for the next reflection has increased by this method. Each new transmitted ray must be traced in addition to its reflected counterpart after each reflection. This eventually creates a limitation on the number of reflections that can be observed using the ray-tracing method as the number of initial conditions increases exponentially with the number of reflection steps considered. The intractability resulting from this increasing number of rays prompts one to use the finite operator method instead, where mapping probabilities from pixel-to-pixel are calculated, and the total number of pixels in the phase space remains constant. Figure 5.6 shows the pixelated versions of the phase spaces of figure 5.5, where the intensity of each pixel is

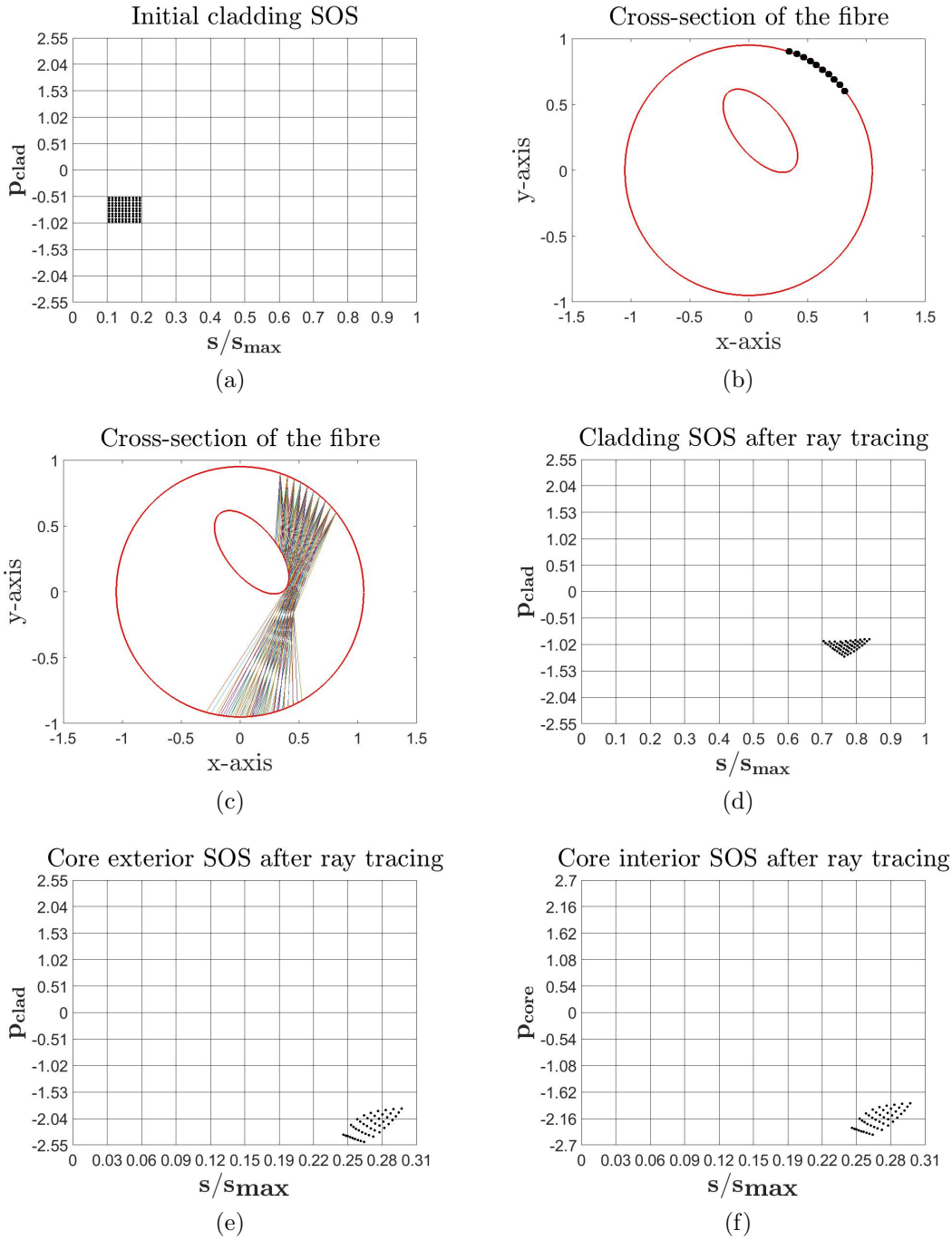


Figure 5.5: Formation of the phase space for the step-index fibre. (a) Initial conditions where a pixel in the cladding SOS is initialised, (b) the cross-section of the fibre showing the initial positions of the rays corresponding to the initialised pixel, (c) the rays are traced until they hit the boundary again and the phase spaces are constructed after the reflection, (d) the cladding phase space for rays reflecting at the cladding boundary (e) the core exterior phase space showing rays hitting the core and being reflected, and (f) the core interior phase space showing the rays hitting the core and being transmitted

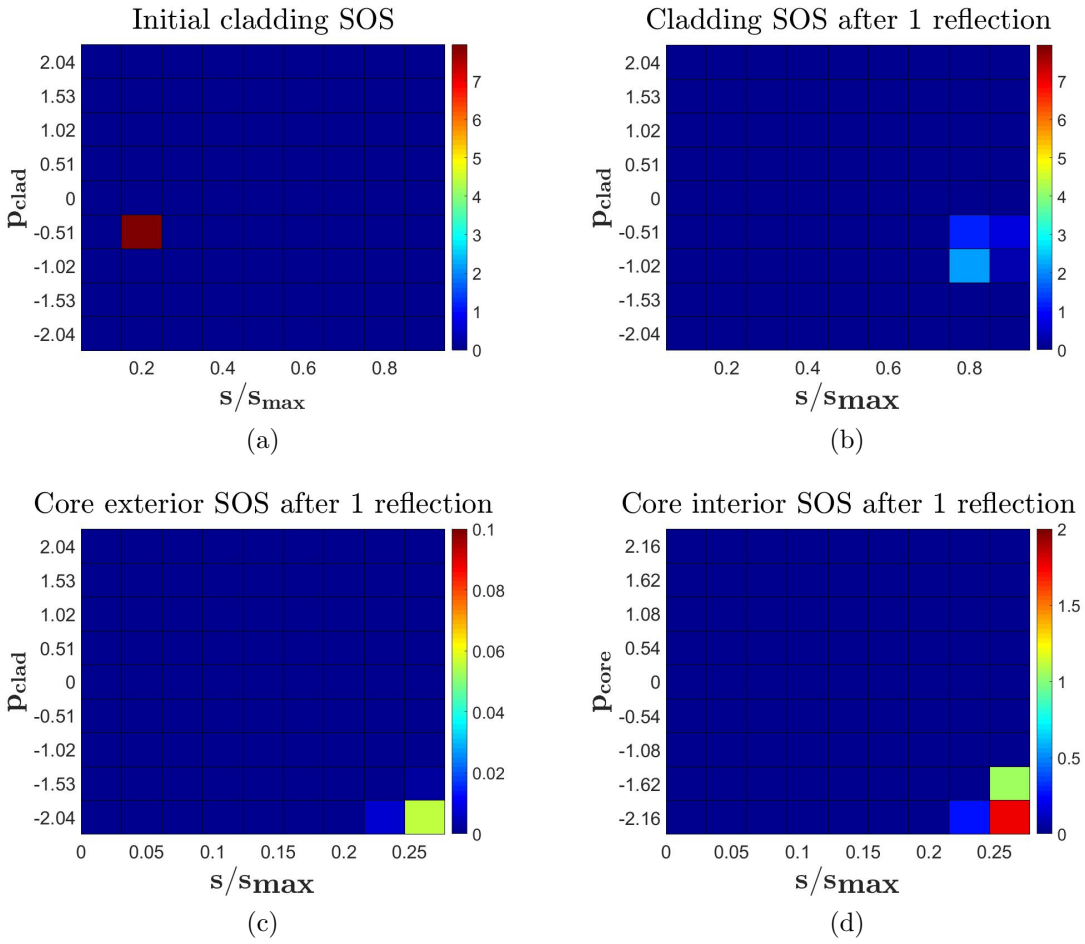


Figure 5.6: Pixelated phase space of the step-index fibre.

determined by the number of rays incident on them after tracing the ray ensemble. In the next subsection, the finite operator for the pixelated phase spaces is constructed, and it is shown to provide a more efficient way to propagate ray distributions in the fibre.

5.3.1 Formation of the extended finite operator

In this subsection, the finite operator matrix blocks consisting of the pixel to pixel mapping probabilities, are constructed for the SIF. Each of the cladding, core exterior, and core interior phase spaces could be divided equally into $N \times N$ pixels such that the total number of pixels becomes equal to $3N^2$. An initial light distribution f_0 in the phase space spread around the boundaries of the SIF is propagated by the 2D finite operator $\bar{T}_{2D}$ for

m reflections as

$$f_m = \bar{T}_{2D}^m . f_0, \tag{5.11}$$

where f_m is the light distribution in the phase spaces after the m^{th} reflection.

The light distribution, f_m, is split into three parts corresponding to the three phase spaces of the SIF. The iterative propagation of the light distribution by the finite operator is given by

$$\begin{bmatrix} f_c \\ f_e \\ f_i \end{bmatrix}_{m+1} = \begin{bmatrix} \bar{T}_{cc} & \bar{T}_{ce} & \bar{T}_{ci} \\ \bar{T}_{ec} & \bar{T}_{ee} & \bar{T}_{ei} \\ \bar{T}_{ic} & \bar{T}_{ie} & \bar{T}_{ii} \end{bmatrix} \times \begin{bmatrix} f_c \\ f_e \\ f_i \end{bmatrix}_m , \tag{5.12}$$

where subscripts c, e, and i refer to the cladding, core exterior, and core interior phase space, or SOS, respectively. The $\bar{T}_{2D}$ is expressed as having sub-matrix blocks where each block registers mapping probabilities of pixels from one boundary to itself or another. Therefore, the $\bar{T}_{cc}$ block represents the mapping probabilities to pixels in the cladding phase space from other cladding pixels, $\bar{T}_{ic}$ represents mapping probabilities of core interior phase space pixels coming from the cladding phase space pixels, and so on. Note that the mapping probabilities are calculated by ray-tracing from individual pixels for one reflection, as described in chapter 4, section 4.3.1, but here in the case of multiple boundaries, some $\bar{T}_{2D}$ sub-block matrices have all-zero entries, such as $\bar{T}_{ee}$, $\bar{T}_{ci}$, and $\bar{T}_{ie}$. This is because, for instance, a pixel from the core exterior phase space can be only mapped on to pixels in the cladding phase space after one reflection.

When each of the phase spaces are divided differently, the dimensions of the sub-blocks of $\bar{T}_{2D}$ are not equal. Table 5.1 shows the $\bar{T}_{2D}$ with its sub-block matrices with their respective dimensions if the cladding, core exterior, and interior phase space are divided into $N \times N$, $N_e \times N_e$, and $N_i \times N_i$ pixels respectively.

With the formation of the finite 2D operator, $\bar{T}_{2D}$, for the SIF boundaries, it is now possible to model successive reflections of a propagating light distribution using the pixelated phase spaces. $\bar{T}_{2D}$ only accounts for cross-sectional components of rays propagating in 3D. In addition to the formation of $\bar{T}_{2D}$, it is also required to measure the distances traversed

Cladding to Cladding $(N^2 \times N^2)$	Outer Core to Cladding $(N^2 \times N_e^2)$	Inner Core to Cladding $(N^2 \times N_i^2)$
Cladding to Outer Core $(N_e^2 \times N^2)$	Outer Core to Outer Core $(N_e^2 \times N_e^2)$	Inner Core to Outer Core $(N_e^2 \times N_i^2)$
Cladding to Inner Core $(N_i^2 \times N^2)$	Outer Core to Inner Core $(N_i^2 \times N_e^2)$	Inner Core to Inner Core $(N_i^2 \times N_i^2)$

Table 5.1: Arrangement and dimensions of the extended $\bar{T}_{2D}$ for the SIF.

by each ray along the z-axis, and therefore construct the full 3D finite operator, $\bar{T}_{3D}$. The analysis of $\bar{T}_{3D}$ is deferred to chapter 7, where its construction is discussed in the context of calculating the net power accumulation in the core after an arbitrary light propagation in a SIF.

In chapter 4, f_0 was defined as a light distribution just after reflection at the curved boundary of the fibre at the cross-sectional plane with $z = 0$. In the following section, a method is developed that constructs f_0 from an arbitrary distribution incident on the xy plane. The light distribution incident on a xy plane inside the fibre media is to be transferred to the curved boundaries of the fibre so that it can be illustrated in the phase space. This allows modelling of light sources at the input face of the fibre that can be propagated using the phase space transport.

5.4 Excitation at the input face of the fibre

In this section, a method to trace light from the input face of the fibre to the curved boundaries is developed. This is an additional step towards the formation of an initial light distribution in the phase space originating from an incident source. The resulting phase space light distribution can then be propagated by using the finite operator method as discussed in the previous section.

Considering only an unstructured fibre at the moment; the light distribution at the curved boundary of the fibre is denoted by

$$f_0(s, \bar{p}_i, z, p_z) \tag{5.13}$$

where $\bar{p}_i$ is the momentum for non-zero p_z in the phase space in a medium with refractive index n. f_0 is constructed using a light distribution from the input face of the fibre. Let the light distribution on the xy-plane at $z = 0$, incident on the fibre,be denoted by

$$\rho(x, y, p_x, p_y), \tag{5.14}$$

which varies with the spatial coordinates (x, y) and the directional components (p_x, p_y) of the rays. Figure 5.7 shows a light source directed in an unstructured fibre and a ray is related from a point source in the xy-plane to the curved boundary. The p_x, p_y, and p_z

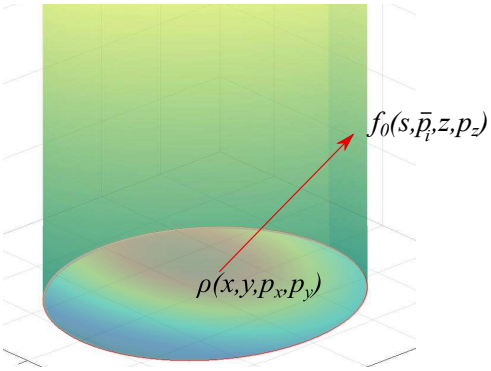


Figure 5.7: A light source is modelled at the input face of the fibre. The light distribution $\rho(x, y, p_x, p_y)$ incident on the xy-plane of the fibre is traced to the fibre curved boundary to form $f_0(s, \bar{p}_i, z, p_z)$.

are components of the unit direction vector of the ray and are given by

$$p_z = \cos\theta, \tag{5.15}$$

$$p_y = \sin\theta \sin\phi, \tag{5.16}$$

$$p_x = \sin\theta \cos\phi. \tag{5.17}$$

The 2D phase space distribution can be evaluated for each p_z at a time. For a particular

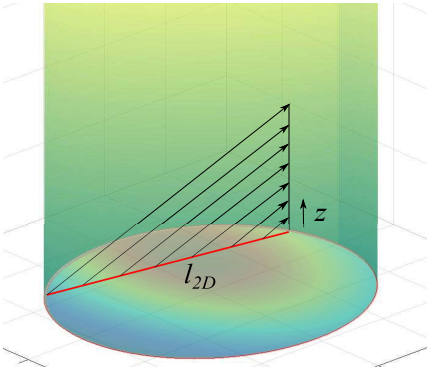


Figure 5.8: The light sources on the xy-plane arriving at the curved boundary along a chord l_{2D} from the fibre input face having constant p_z.

$(s, \bar{p}_i, p_z)$ in the phase space, the contribution of all source points in the xy-plane lies along a 2D chord, l_{2D} in the fibre as shown in figure 5.8. The integral of f_0 along z is then given by

$$\int_0^\infty f_0(s, \bar{p}_i, z, p_z)dz = \int_{l_{2D}} \rho(x, y, p_x, p_y)dl, \tag{5.18}$$

where

$$dz = \frac{p_z}{\sqrt{(1 - p_z^2)}}dl. \tag{5.19}$$

For a particular p_z, a light source ρ in the xy-plane is normalised such that

$$\int \rho(x, y, p_x, p_y)dxdydp_xdp_y = 1 \tag{5.20}$$

inside the fibre. Let, the refractive index of the unstructured fibre be $n_i = 2.55$, and since p_z is constant, the directional components of each ray is constrained by

$$p_x^2 + p_y^2 = 1 - p_z^2. \tag{5.21}$$

A light source for example, invariant of p_x, and p_y, is shown in figure 5.9 and the resulting rays emanate in the form of a cone from every point from the input face.

Let $p_z = 0.9$, and allow the fibre boundary to be deformed using the quadrupolar equation defined by equation 3.1 with $r = 1$. The pixelated phase space is constructed from

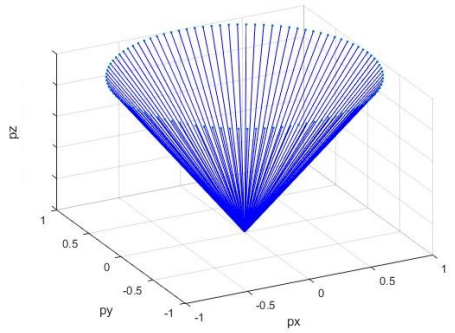
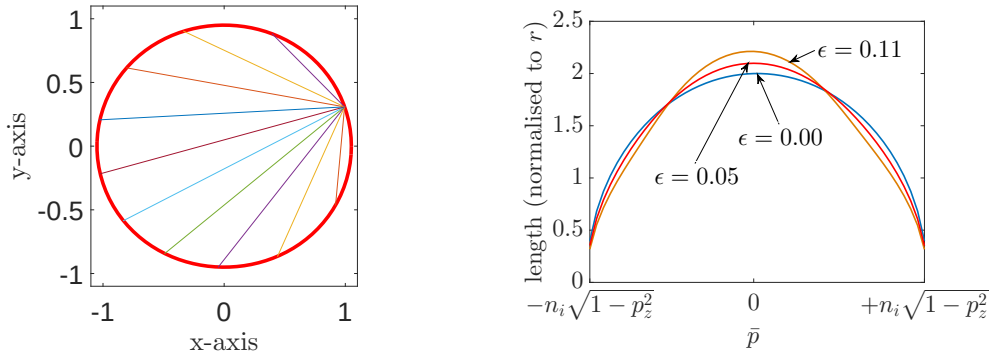


Figure 5.9: Rays emanating in the form of a cone when the value of p_z is fixed for each source point inside the fibre cross-section. The direction of each ray is uniformly weighted to model the source.

$\rho(x, y, p_x, p_y)$ by integrating all point sources in the xy-plane along cross-sectional chords to obtain the distribution $f_0(s, \bar{p}_i, z, p_z)$ at the curved boundary. The transformation from (x, y, p_x, p_y) to $(s, \bar{p}_i, z, p_z)$ is made, where the light distribution from the input face is transformed into a distribution in the boundary phase space, with the total power in the input distribution being equal to the total power in the phase space.

In the following subsection, a phase space distribution f_0 is constructed for a unstructured fibre from an arbitrary uniform light source in the xy-plane for a particular p_z. The changes in the phase space distribution is investigated when the boundary of the fibre is deformed. The model is then extended to the case of step index fibres, and the changes in the phase space from the same arbitrary input in the xy-plane are investigated in relation to the boundary deformations.

The input distribution is mapped into a pixelated phase space. Each chord length is generated by choosing $(s, \bar{p}_i)$ from the mid-point of the phase space pixel. Figure 5.10(a) shows an array of chords, each having a different value of $\bar{p}_i$, originating from a single s position. Figure 5.10(b) shows the variation of the chord lengths for each $\bar{p}_i$ from a particular s, as the boundary is deformed. The variation of the chord length, l_{2D}, over $\bar{p}_i$ is the same for each s when $\epsilon = 0$, but with non-zero ϵ, it depends on both s, and $\bar{p}_i$. So, when the light distribution in the input face is kept uniform, the phase space shows variation in the light distribution in relation to the variation of l_{2D}.



(a) (b)

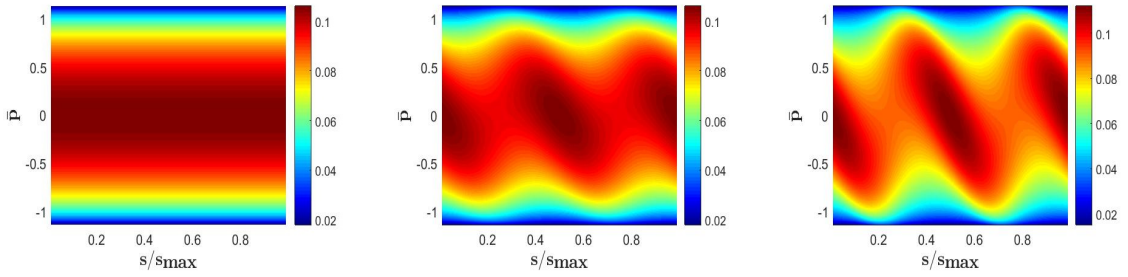
Figure 5.10: Variation of chord length with boundary deformation. Each chord is generated by choosing $(s, \bar{p})$ from the mid-point of a phase space pixel. (a) The chords for each $\bar{p}$, at an arc length along the curved boundary s. (b) Variation of the chord length, l_{2D}, with $\bar{p}$ at a particular s. The l_{2D} variation over $\bar{p}$ is the same for each s when $\epsilon = 0$, but with non-zero ϵ, it depends on both s, and $\bar{p}$.

5.4.1 A uniform light source model at the fibre input face

In this section, an artificial light source is modelled that illuminates the input face of the fibre uniformly. This is done to show the variation in the transferred power from the input face to the curved boundaries with the variation in the length of propagation for the first reflection. The variation is also shown when the fibre cross-sectional boundaries are deformed. The analysis in this section will shed light in the way in which the input source launching criteria may be designed in an experimental setup in future. A simple model of the input source is taken where power emanating in any direction of propagation is invariant, and the magnitude of intensity at the input face is also invariant of (x, y) in the input cross-section. As will be discussed using figure 5.13, in deformed SIFs, a uniform distribution at the input facet maps non-trivially to the phase spaces, and the input light source is required to be carefully designed.

Figure 5.11 shows the phase space distribution of $f_0(s, \bar{p}_i, p_z)$ resulting from a uniform distribution at the input face of the fibre. The distribution is altered when boundary deformation is introduced and the variation is dependent on the changes in the chord length. Therefore, figure 5.11(a) shows the phase space of a circular boundary where the variation in $\bar{p}_i$ is the same for all s. Figure 5.11(b) and (c) shows the power distribution in

the phase space for deformed boundaries with $\epsilon = 0.05$, and $\epsilon = 0.11$ respectively, where the distribution varies with chord length for both s, and $\bar{p}_i$ variation.

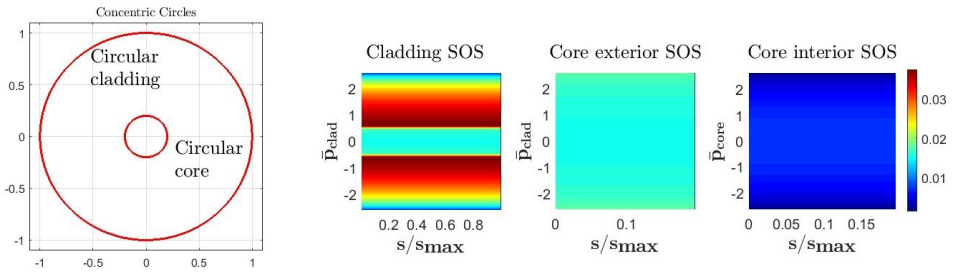


(a) (b) (c)

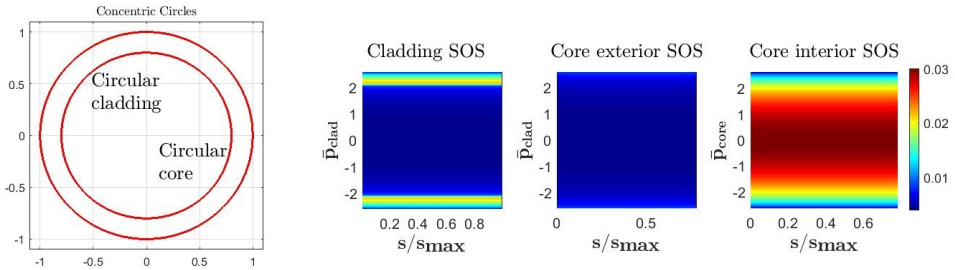
Figure 5.11: The light distribution in the phase space of the unstructured fibre resulting from a uniform distribution at the fibre input face, for (a) $\epsilon = 0$, (b) $\epsilon = 0.05$, and (c) $\epsilon = 0.11$.

This analysis is extended to the boundaries of the SIF, with the formation of the additional core interior and exterior phase spaces. The light sources from the input face is incident on the pixels of each of the three phase spaces of the SIF, and the resulting light distribution is obtained. Figure 5.12 shows SIFs with circular core and cladding boundaries with the core positioned at the origin in the fibre cross section. The refractive index of the core is $n_c = 2.70$, and that of the cladding is $n_{cl} = 2.55$. Figure 5.12(a) shows a small core size, with radius, $r_c = 0.2828$, and a core area of 8% relative to the total SIF cross-section. In this case, most of the power from the input cross-sectional face ends up in the cladding boundary and the intensity in the cladding phase space is higher. In figure 5.12(b) a larger core with $r_c = 0.8$ is used where the intensity in the core interior phase space now is higher than that in the cladding phase space. In each case, the cladding phase space shows a cut-off valley for low $|\bar{p}_{\text{clad}}|$ due to a shadow created by the core boundary. The phase spaces with circular boundaries show no variation along s-axis, and the valley is rectangular in shape.

Figure 5.13 shows the constructed phase spaces with various deformations in the SIF cross-sectional structure. In figure 5.13(a), the core and cladding boundaries are circular, but the core is placed in an off-centred position in the fibre at $(0.1, 0)$. The resulting light



(a)



(b)

Figure 5.12: Uniform distribution at the input face of the step index fibre. (a) Incident light at the boundaries of the fibre with small core, with $r_c = 0.2828$, shows more power being transferred to the Cladding SOS rather than the core interior SOS. (b) Incident light at the boundaries of the fibre with a larger core, with $r_c = 0.8$, results in more power initialised in the core interior SOS instead. In circular SIFs, the input distribution varies with momenta, $\bar{p}_i$, of the media i=core,clad, but not with s.

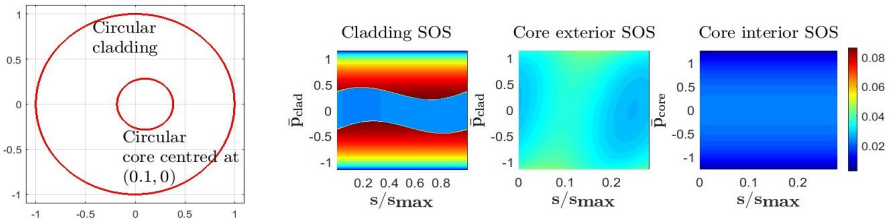
distribution from a uniform distribution from the input face is shown in the boundary phase spaces. The cladding SOS shows a non-linear cut-off valley in the places where l_{2D} was cut short due to the presence of the core. In figure 5.13(b), the core is made elliptical, with the centre at the origin, and the resulting phase space is constructed. Here the core interior and exterior phase space shows non-linear patterns due to l_{2D} depending on both s, and $\bar{p}_i$. The cladding SOS shows the non-linear cut-off valley created due the core's shadow. In figure 5.13(c), the phase space is created with an elliptical core centred at $(0.1, 0.3)$, and figure 5.13(d) shows the created phase space of a SIF with a deformed cladding boundary (quadrupolar boundary with $\epsilon = 0.05$) in addition to the core being elliptical and off-centred.

In this subsection, the variation in the phase space due a uniform distribution the input face of the fibre is discussed with both deformed and circular SIFs. In the following subsection, the formation of $f_0(s, \bar{p}_i, z, p_z)$ is investigated when the input distribution at the fibre input face is changed from a uniform distribution to a Gaussian distribution.

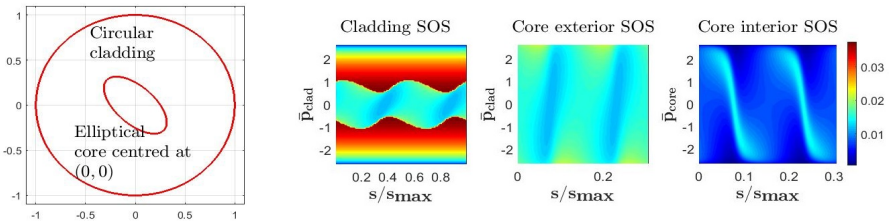
5.4.2 Gaussian distributions at the fibre input face

In this section, the light distribution at the input face is changed to a Gaussian distribution from a uniform distribution of the previous subsection, which is more similar to a practical light source. The changes in the phase space of the deformed SIF are observed with the changes in the mean position and size of the Gaussian distribution. The case of the deformed SIF cross-section, as shown in figure 5.13(d), is used to obtain the input distribution in the phase space in this section.

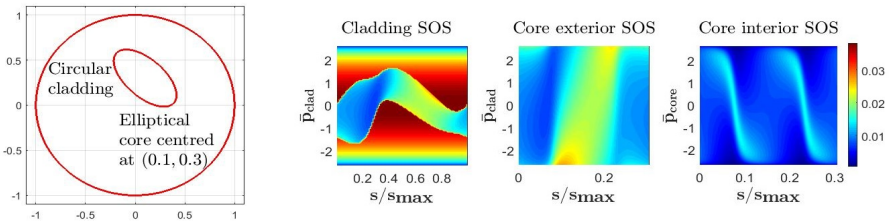
Figure 5.14 shows examples of Gaussian distributions incident at the input face of the SIF with the deformed core and cladding boundaries. In figure 5.14(a) a Gaussian distribution, G1, is incident directly into the core. The mean position of the Gaussian peak is made the same as the centre of the core, and it is at $(0.1, 0.3)$. The variances of the Gaussian along both x and y directions are equal ($\sigma_x = \sigma_y = 0.2$).



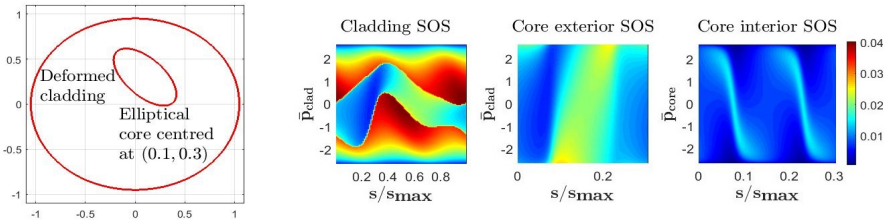
(a)



(b)

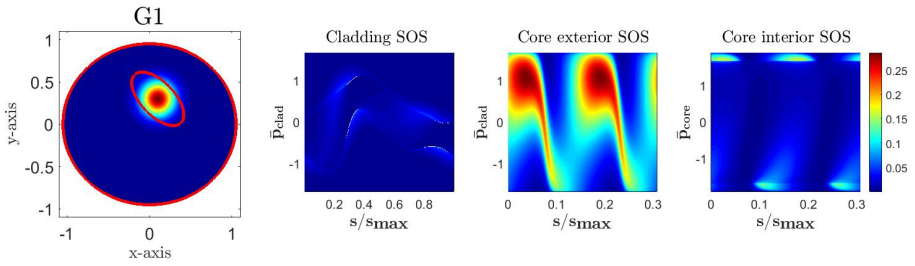


(c)

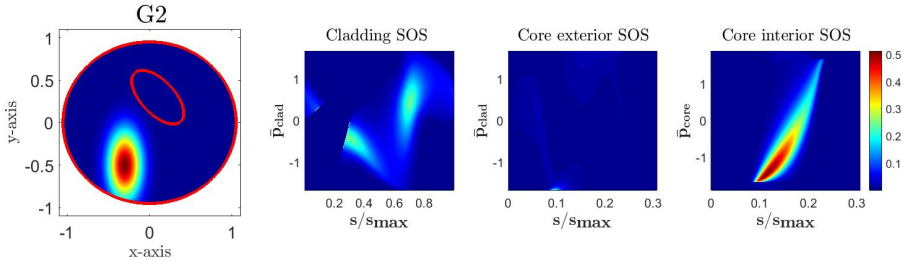


(d)

Figure 5.13: Variation in the phase space distribution from a uniform light distribution at the input face of the fibre with (a) the core moved to an off-centred position at (0.1,0), (b) the core made elliptical with major and minor axis given by $a = 0.4$, and $b = 0.2$, and its axis rotated by 135°, (c) the elliptical core then moved to an off-centred position at $(0.1, 0.3)$, and (d) the cladding boundary is also deformed in addition to the core by using $\epsilon = 0.05$ and $R = 1$ in the quadrupolar equation 3.1.



(a)



(b)

Figure 5.14: Gaussian distributions incident at the input face of the fibre, and the resulting phase space distribution at the curved boundaries after the first reflection. In (a) a Gaussian distribution, G1, incident directly into the core is modelled, where the mean position of the Gaussian beam is $(0.1, 0.3)$, the same as the centre of the core. The variance of the Gaussian is the same along both x and y axes, and is equal to $\sigma_x = \sigma_y = 0.2$. In (b) a Gaussian distribution, G2, is placed away from the core, at a mean position of $(-0.3, -0.5)$, and with $\sigma_x = 0.2$, and $\sigma_y = 0.4$.

The resulting phase spaces are shown, that is the light distributions, after arriving at the curved boundaries and once reflected. Very little light reaches the cladding phase space in the first reflection, and most of the excitation in the core is transmitted out of the core and ends up in the core exterior phase space as transmitted light. The TIR region of the core is excited partially by this input distribution, as shown by the resulting core interior phase space. The light trapped here will remain permanently throughout the light propagation.

In figure 5.14(b), a Gaussian, G2, is incident upon the input face in the same SIF but away from the core. Here, the Gaussian is centred at $(-0.3, -0.5)$, with variance along the x axis is $\sigma_x = 0.2$, and the variation along the y-axis $\sigma_y = 0.4$. The resulting phase spaces are shown. Any light incident at the core boundary is transmitted into the core medium, as shown by the core interior phase space, and very little gets reflected off the

boundary, as shown by an almost empty core exterior phase space.

The propagation of these Gaussian distributions from the input face of the SIFs can be conveniently undertaken using the finite operator model. Obtaining a model for the phase space distribution resulting from the light incident on the input cross-sectional face of the fibre provides insight as to how the source must be designed to excite the fibre. In the following chapter, the properties of the two dimensional finite operator $\bar{T}_{2D}$ are investigated to better understand the dominant patterns in the phase spaces of deformed SIFs, similar to the analysis done for unstructured fibre in section 4.3.2, chapter 4.

5.5 Chapter summary

In this chapter, the finite operator method has been extended to model SIFs. Additional phase spaces were made to include the inward and outward facing boundaries of the core. The finite operator enables efficient simulation of light propagation in SIFs and the same calculations are numerically prohibitive when the ray-tracing method is used. The method to construct the 2D finite operator, $\bar{T}_{2D}$, was shown by calculating the mapping probabilities. After its formation, successive reflections at the boundaries of the fibre can be carried out for any arbitrary input and its evolution can be visualised in the pixelated phase spaces.

In addition, a model was also presented to obtain a light distribution in the phase space from a source at the input face of the fibre. The model allowed light distribution at the boundaries of the fibre to be related to the distribution that entered the fibre and showed how changes in the boundary deformations affected the light reaching the curved boundaries.

In the following chapter, the properties of $\bar{T}_{2D}$ for SIFs will be investigated with $p_z = 0$, i.e. on a 2D setting. The changes in the leading eigenvectors of $\bar{T}_{2D}$ are observed with the changes in resolution of the pixelated phase spaces and the properties of the SIF cross-sectional structure. The formation of the full 3D finite operator, $\bar{T}_{3D}$, will be discussed

in chapter 7, where the calculations will also include the distances traversed by the rays along the z-axis. In chapter 7, the net accumulation of power in the core in SIFs will be be calculated using the finite operator model, after 3D light propagations, and modelling parameters that effect such measurements will be investigated.

Chapter 6

Properties of the 2D finite operator for step-index fibres

6.1 Introduction

The formation of the finite operator, $\bar{T}_{2D}$, as described in the previous chapter, enables the visualisation of successive reflections of arbitrary light distributions in the pixelated phase spaces of the step-index fibre (SIF). In this chapter, the properties of the $\bar{T}_{2D}$ will be investigated, where it only suffices to consider the 2D components of the propagating rays. Densities obtained by iterating with the full 3D finite operator, $\bar{T}_{3D}$, that accounts for both the cross-sectional and axial components of the rays propagating in the fibre will be discussed in chapter 7.

The properties of $\bar{T}_{2D}$ will be analysed using its eigen-decomposition, as was done on the finite operator for the unstructured fibre in chapter 4. The evolution of the light intensity propagated by the finite operator eventually converges to its leading eigenvector after a large the number of iterations, as dictated by the Frobenius-Perron theory [68]. As was shown in chapter 4, the finite approximation undertaken by the pixelation of the phase space creates some non-physical artefacts in the dynamical system in the form of diffusion. Although the finite operator captures most of the dominant physical attributes of the light

propagation, these diffusion artefacts result in a non-physical steady-state. Therefore, before the phase space evolution converges towards the leading eigenvector, successive iterations performed by the operator must be truncated at some point before diffusion artefacts takes over. Truncation preserves the contributions of the smaller eigenvectors of the 2D finite operator on the overall evolution of the light distribution and a steady state distribution can be obtained that adheres to the physical dynamics.

In this chapter, the effect of diffusion in the phase space transport is investigated in SIFs, and an observation window is established in terms of the number of reflections before which the phase space evolution is taken over by the diffusion artefacts. The eigen-spectrum of the $\bar{T}_{2D}$ for a deformed SIF is investigated. In subsection 6.2.2, the eigen-decomposition of the $\bar{T}_{2D}$ for the SIF is carried out to investigate the contribution of the leading eigenvectors on the steady state distribution. The leading eigenvectors vary with the resolution of the pixelated phase space. So, in subsection 6.3.1, the variation in the properties of $\bar{T}_{2D}$ is investigated by varying the resolution of the phase space for a given input distribution. Lastly, in subsection 6.3.2, the variation in the properties of $\bar{T}_{2D}$ is observed by varying the refractive index contrast between the core and cladding media of the SIF.

6.2 The phase space transport

A simple arbitrary light propagation using the 2D finite operator suffices to explain the dynamical behaviour in the pixelated phase spaces of the SIF. Propagation of a light distribution within the SIF with cross-sectional properties described in section 5.3 is chosen. Here, a finer coarse-grained phase space is chosen with $N = N_e = N_i = 300$ as the size of pixels with $N = 10$ is too large to discern any phase space pattern; the resulting discretised $\bar{T}_{2D}$ has dimensions of $3N^2 \times 3N^2$. Figure 6.1(a) shows the initial light distribution chosen for the propagation, which consists of uniformly exciting all the pixels in the cladding SOS. The distribution from the cladding is spread to other parts

of the phase space as observed for successive reflections in figures 6.1(b)-(e). The colour maps show the power distribution in various parts of the phase spaces and locate the various regular and chaotic regions that are formed in the dynamical system as the light distribution is reflected within the boundaries of the fibre.

The propagation of the initially uniform distribution from the cladding is limited to 500 reflections for now in order to observe the dynamics in the transient state. During the transient state of the evolution, the intensity from the cladding phase space is propagated to other phase spaces over successive reflections. At steady state, a mixed phase space distribution will be formed where power is divided between the chaotic sea, and various regular regions. This is seen in figure 6.1(e), where the steady state is nearly reached and the area coloured by yellow/green is the chaotic region and those regions coloured red/blue are the various regular regions. Therefore, the addition of the core boundary allowed the intensity from the cladding phase space to flow towards the empty core phase spaces and eventually fill out all the available regular and the chaotic regions.

6.2.1 Leaky resonance

The steady state distribution has not been reached in figure 6.1 after 500 reflections because of the presence of a phenomenon termed here as *leaky resonance*. The steady state of the evolution itself will be discussed in more detail in conjunction with the eigen-analysis of the finite operator, $\bar{T}_{2D}$ in section 6.2.2. Figure 6.1(b) shows the phase space distribution after the 10^{th} reflection where the distribution is seen to have spread into all three parts of the phase space. Outlines of the regular islands start to appear after 50 reflections, as shown in figure 6.1(c). Note that the cladding phase space, or SOS, patterns, formed for the deformed cladding boundary defined with the quadrupolar equation having $\epsilon = 0.05$, are similar to the phase space in figure 3.8 in chapter 3 for higher $|\mathrm{p_{clad}}|$ range. In the presence of the core, however, the regular regions in the cladding SOS for the lower $|\mathrm{p_{clad}}|$ range have disappeared and have been replaced by a chaotic sea, but the regular regions for higher $|\mathrm{p_{clad}}|$ range have remained unchanged. Even within

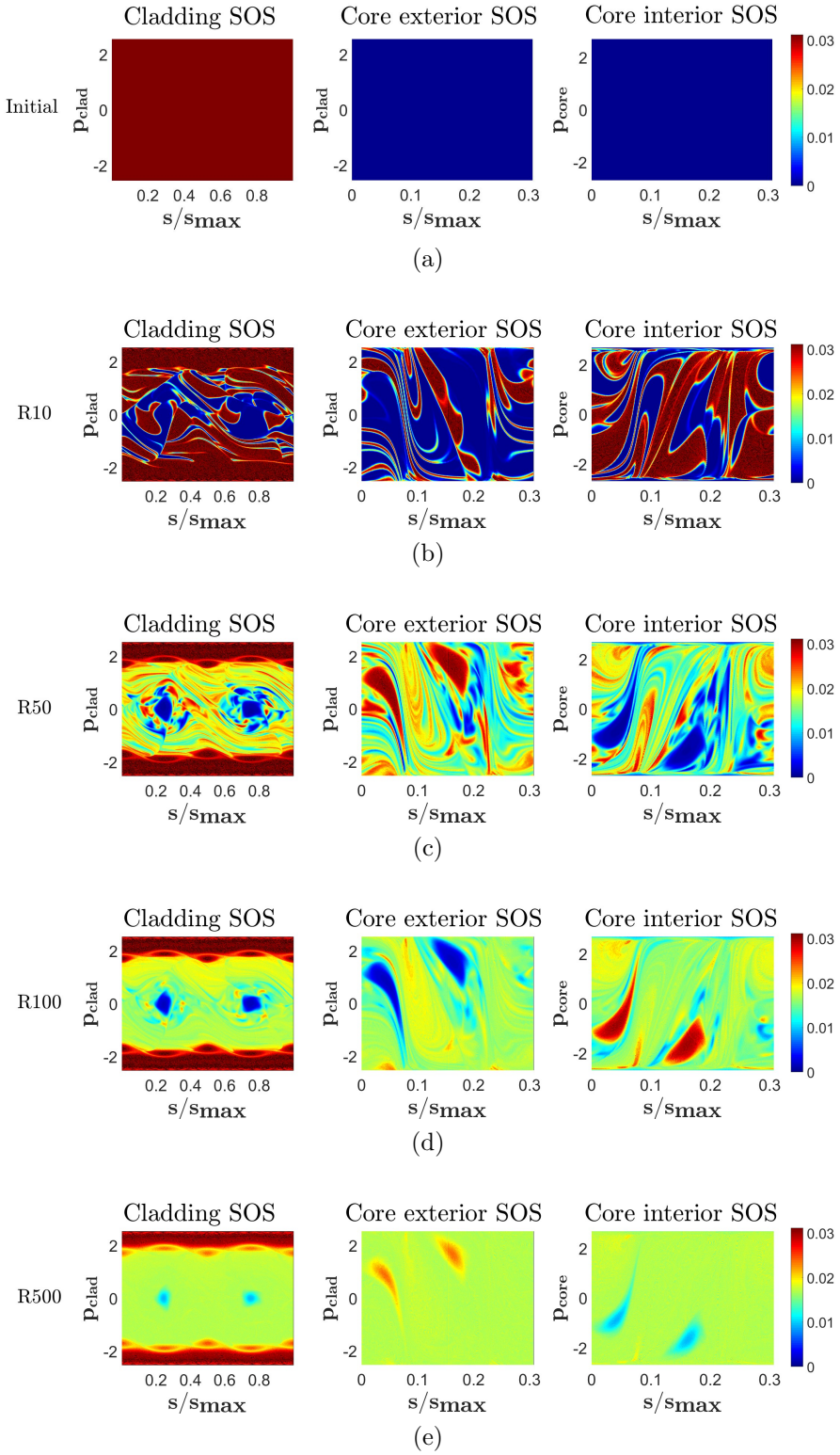


Figure 6.1: Evolution of an initial light distribution in the pixelated phase space of the step-index fibre. (a) The cladding SOS is uniformly excited initially. The evolution of the initial light distribution is shown after (b) 10, (c) 50, (d) 100, and (e) 500 reflections

the scattered region, the power is seen to oscillate among some quasi-regular islands around $s = 0.25s_{\max}, 0.75s_{\max}; \mathrm{p_{clad}} = 0$. After 100 reflections, figure 6.1(d) shows that the intensity in the chaotic sea has settled down and the embedded regular islands have become more clearly visible. In the cladding SOS, the regions in red for high $|\mathrm{p_{clad}}|$ are permanent regular regions and on the other hand the two regions in blue for $|\mathrm{p_{clad}}| \approx 0$ as transient or pseudo- regular regions. The embedded blue/red islands seen in the core exterior and interior SOS in figure 6.1(d) are also part of the transient regular regions in the evolution. The reason for differentiating the regular regions in this way will become clear after the phenomenon of leaky resonance has been discussed.

Figure 6.1(e) shows the evolution of the distribution after 500 reflections. The decay of intensity from the various regular regions has resulted in shrinkage of the area occupied by them. The phase spaces now show fewer distinct regular regions and an expanded chaotic sea. Notice that between the 100^{th} and the 500^{th} reflection, the intensity in the pseudo-regular regions has decayed more rapidly than that in permanent ones, indicating different underlying mechanisms of decay between the two types of regions.

The decay from permanent regular regions occurs because of diffusion and is an artefact of the pixelation of the phase spaces. In figure 6.1(e), at higher $|\mathrm{p_{clad}}|$ the permanent regular regions in the cladding SOS have lost very little of their intensity and the trajectories corresponding to these regular regions do not hit the core boundary. These include the regular islands in the cladding SOS corresponding to the whispering gallery motion with the cladding boundary, and four periodic islands whose corresponding motion was described in section 3.2.3, figure 3.7(c) in chapter 3.

The pseudo-regular region in the cladding SOS corresponds to the vertical 2-bounce reflection in the unstructured fibre cross-sectional boundary as discussed in section 3.2.3, chapter 3 with figure 3.6(a). However, in the SIF, these trajectories pass through the core medium and therefore the corresponding pseudo-regular counterpart regions also appear in both the core exterior and interior SOS as is more visible in figure 6.1(d). The intensity leakage from the pseudo-regular regions is a part of the physical dynamics in the system

and occurs because of reflections occurring at the core-cladding dielectric boundary.

The power in those trajectories which correspond to the pseudo-regular regions are scattered because of the regular round-path as will be described now. A group of rays starting from the vicinity of $s = 0.25 s_{\max}; \mathrm{p}_{\mathrm{clad}} = 0$, in the cladding boundary reaches the core boundary and gets partially reflected and partially transmitted. The reflected power appears in the core exterior SOS and the transmitted power appears in the core interior phase space. The rays getting reflected are scattered from the regular path and the power in the scattered rays end up in the chaotic sea. Upon the second reflection, the rays transmitted into the core hit the core boundary again and this time the core interior phase space shows the power scattered in the reflected rays and the core exterior phase space shows the power in the transmitted rays. Again the transmitted rays remain in the regular path and the reflected rays end up in the chaotic sea. Upon the third reflection, the transmitted ray then reaches the cladding boundary again at the core exterior ($s = 0.75 s_{\max}; \mathrm{p}_{\mathrm{clad}} = 0$) where it is completely reflected. The reverse path taken up by the rays remaining in regular motion also results in two more scattering events at the core-cladding dielectric boundary. Eventually, after enough reflections, the power carried by these rays in regular motion through the core will be completely scattered into the chaotic sea. So the pseudo-regular regions appearing in the evolution of the light distribution occur due to this process of leaky resonance.

If the iterations are continued indefinitely the power trapped in all regular regions would eventually leak out and only a chaotic sea will be seen, uniformly distributed in all the phase spaces. However, as opposed to being a diffusion artefact, the leaky resonance is a real phenomenon and the rate of scattering of power from them depends on the refractive index contrast between the core and cladding media. The objective here is to obtain a steady state by minimising the diffusion artefacts in the pixelated phase while allowing the power trapped in leaky resonant regions to scatter completely.

The observation window is set in terms of a number of reflections at the end of which an effective steady state is reached in the physical dynamics. In figure 6.1, the modelling

parameters chosen do not allow this to happen because some permanent regular regions in the cladding phase space are decaying significantly due to diffusion, whereas the rate at which the leaky resonances in the system is decaying is very slow. Before the observation window could be set, the power from the permanent resonant regions have decayed already and the phase space distribution is significantly distorted. There are two ways to prevent this distortion. The first, which for a given fibre may be the only way, is to decrease the rate of diffusion by decreasing the individual pixel areas in the phase spaces. This results in a larger, and more computationally demanding, $\bar{T}_{2D}$. The second way is more case specific and involves changing the refractive index contrast between the core and cladding media so that the leaky resonances decay faster. This changes the fibre model, but from a modelling perspective, changing the refractive indices of the core and cladding is a more convenient way to determine the observation window for a given phase space pixelation. In the following section, the phenomenon of leaky resonance is investigated more extensively with the help of the eigen-analysis of $\bar{T}_{2D}$. In section 6.3, the contributions of the leading eigenvalues and eigenvectors are observed and possible changes in such modelling parameters to overcome the competing decay rates are explored.

6.2.2 Eigen-decomposition of the 2D finite operator

The characteristics of the light distribution propagated in phase space are also evident in the properties of the eigen-spectrum of $\bar{T}_{2D}$. The process of numerically obtaining the eigen-decomposition of the $\bar{T}_{2D}$ was discussed in section 4.3.2 chapter 4, and the same procedure is used for the eigen-decomposition of $\bar{T}_{2D}$ constructed for the SIF. The eigen-decomposition is carried out for $\bar{T}_{2D}$ constructed for the cross-section shown in figure 5.5(b) with core refractive index as $n_{\mathrm{c}} = 2.70$, and $n_{\mathrm{cl}} = 2.55$. Figure 6.2 shows the 20 leading eigenvalues of the matrix in the complex plane. The largest eigenvalue is equal to one, and the other eigenvalues are inside the unit circle in the complex plane with magnitudes less than, but close to, one. The largest 6 eigenvalues and their corresponding eigenvectors are all real-valued. Figure 6.3 shows the 1^{st} (E1), 2^{nd} (E2), 3^{rd} (E3), 4^{th} (E4)

and 5^{th} (E5) eigenvectors of the $\bar{T}_{2D}$ matrix, and apart from the leading eigenvector E1, they correspond to the various regular regions in the phase space of the SIF cross-section as will be detailed in the following sub-subsection.

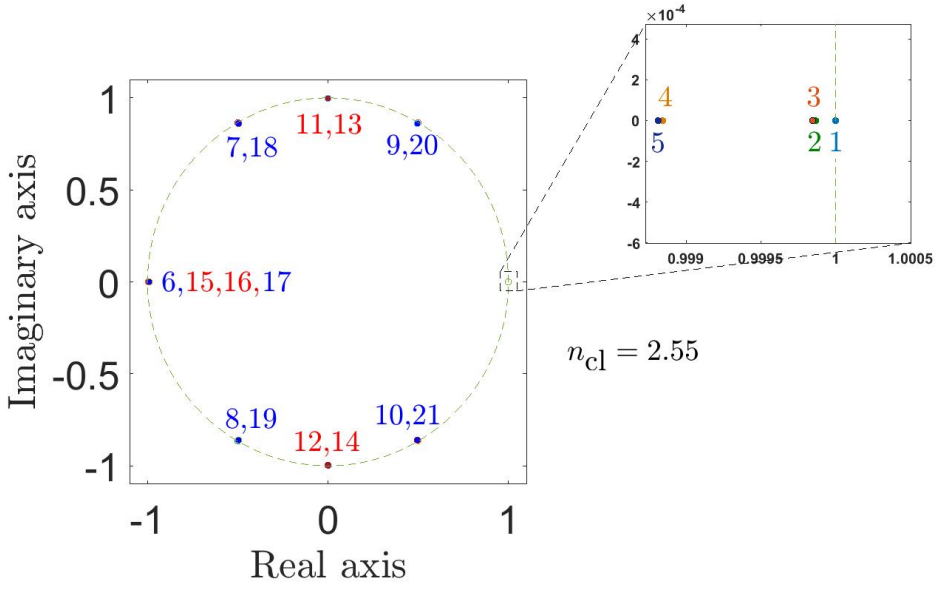


Figure 6.2: Leading eigenvalues of $\bar{T}_{2D}$ constructed for the SIF with cross-section shown in figure 5.5(b) and the phase space is pixelated with $N = N_e = N_i = 300$. The cladding and core refractive indices are given by $n_{cl} = 2.55$, $n_c = 2.70$.

Regular motion of rays represented in eigenvectors of the finite operator

Apart from E1, the distribution of the next four leading eigenvectors correspond to the permanent resonances of the phase space. Most of them are in the cladding SOS and occur due to regular motion of trajectories unscattered by the presence of the core boundary. These regular motions can occur in a counter-clockwise (CCW) or clockwise (CW) manner around the cross-section. Therefore, (E2, E3), and (E4, E5) occur in pairs indicating the corresponding motion in CCW and CW directions respectively [80]. Figure 6.4 shows this more clearly, where E2 and E3 are added together in figure 6.4(a) where only a CW motion remains, and subtracted in 6.4(b) where only the CCW motion remains. The same addition and subtraction is shown for the (E4, E5) pair in figures 6.4(c) and (d) respectively.

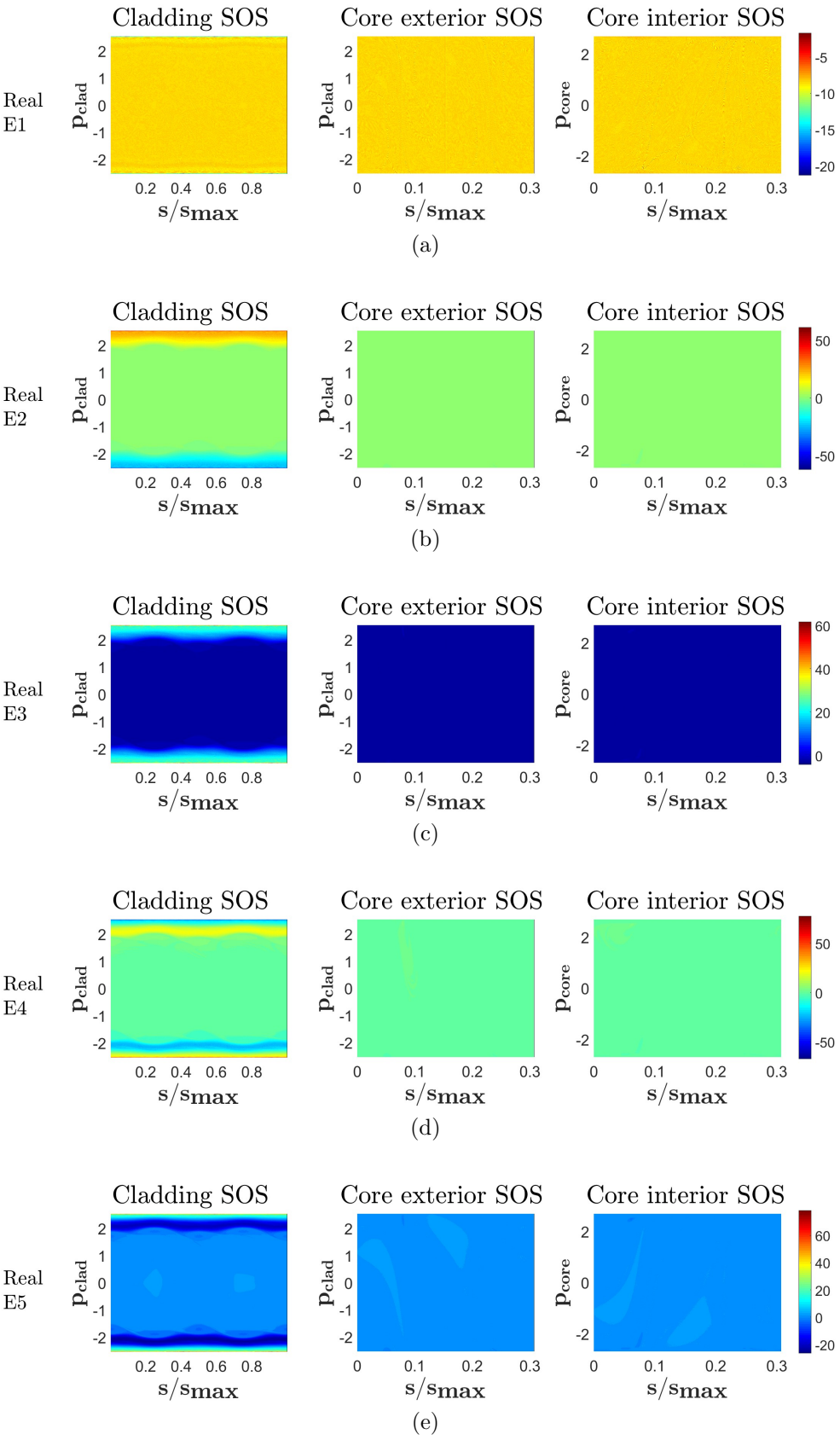


Figure 6.3: Five leading real eigenvectors of $\bar{T}_{2D}$ for the SIF structure shown in figure 5.5(b), whose phase space is pixelated with $N = 300$ with corresponding eigenvalues shown by the inset in figure 6.2. The eigenvector corresponding to the largest eigenvalue is a uniform distribution throughout the entire phase space.

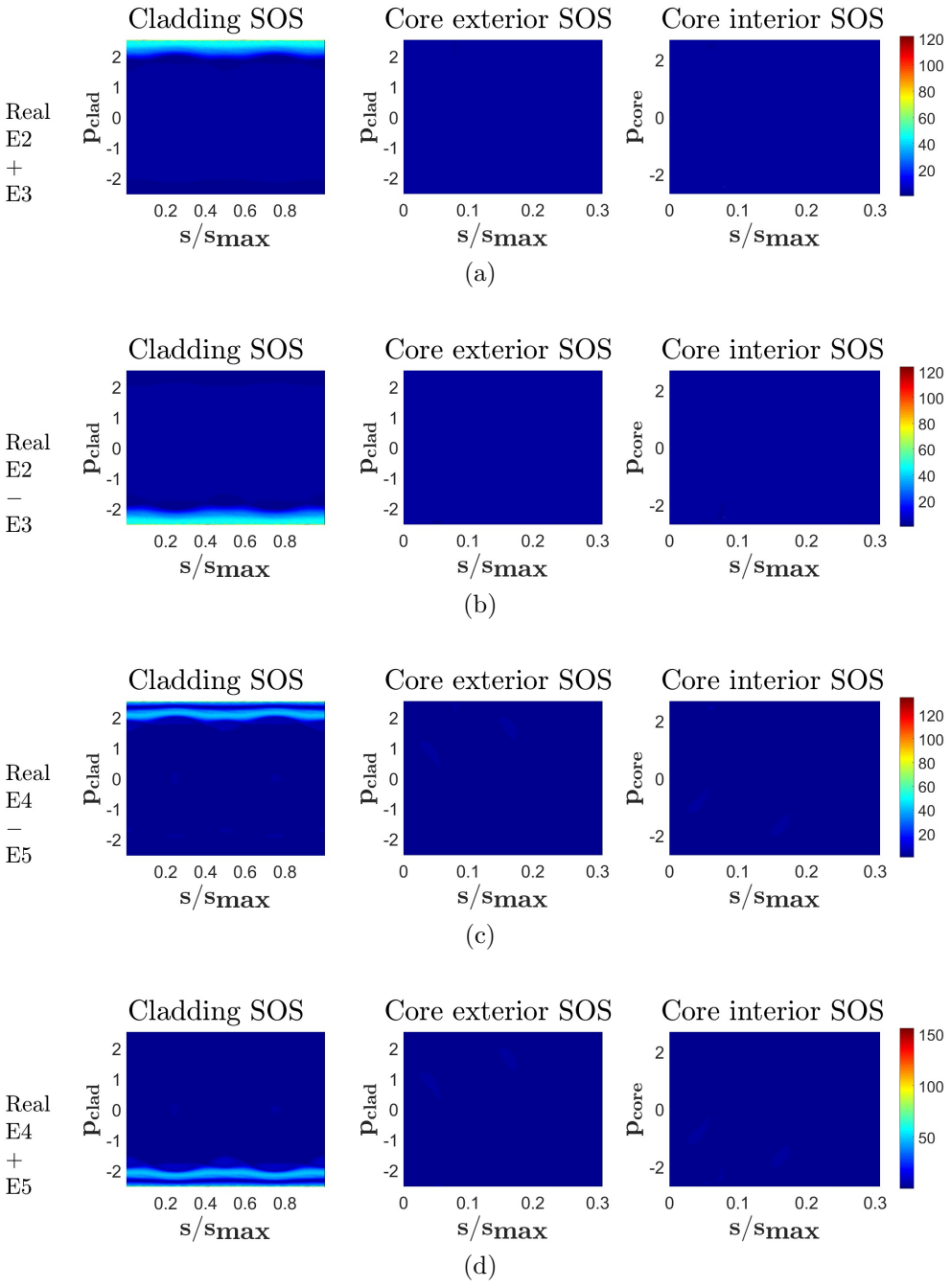


Figure 6.4: (a) CCW and (b) CCW permanent resonances shown by the eigenvector pairs E2 and E3. (c) CW and (d) CCW resonance counterparts between E4 and E5 eigenvectors.

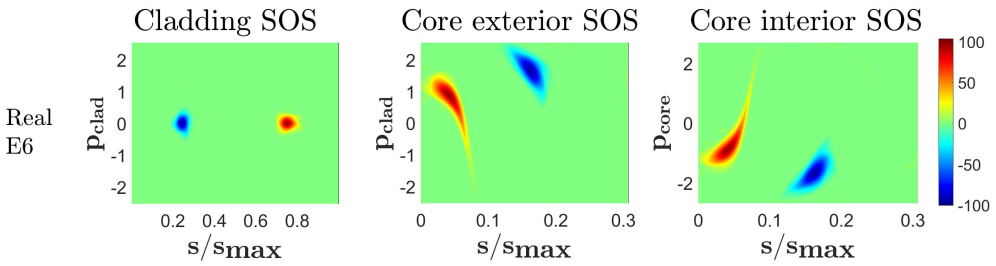


Figure 6.5: 6^{th} leading eigenvector corresponding to a leaky resonance in the T-matrix constructed with $N = N_e = N_i = 300$, $n_{\text{cl}} = 2.55$, $n_{\text{c}} = 2.70$.

The leaky resonance is reflected in the sixth leading eigenvector E6, as shown in figure 6.5. As discussed in section 6.2.1, this resonance can only be temporary since the rays in this resonance are scattered continually by the core. There is more than one eigenvector that corresponds to the leaky resonance. For instance, the eigenvectors corresponding to the 7^{th}, 8^{th}, 9^{th}, and 10^{th} eigenvalues (shown in blue in figure 6.2) are all variants of E6 and the eigenvalues are complex conjugates of each other. Figure 6.6 shows E9 and E10 eigenvector pairs, whose corresponding eigenvalues are complex conjugates. The real parts of both E9 and E10 are identical as shown in figure 6.6(a), but their imaginary parts are shifted in phase as shown in figure 6.6(b) and (c) with their intensity peaks found at different spots in their conjugate phase space distribution. This is also true for any island-like regular regions in the phase space, and a similar phenomenon for the case of a permanent resonance in the cladding is shown for eigenvectors E11 and E12 in figure 6.8.

The evolution of an arbitrary light distribution in the pixelated phase space, as shown in figure 6.1 revealed the various permanent regular regions in the phase space. In the cladding SOS, the island-like permanent regular regions also occur as CW-CCW pairs, as shown in figure 6.7. The eigenvectors for this motion occur at the 15^{th} and 16^{th} rank among the largest eigenvalues. The CW eigenvector is shown in figure 6.7(a), formed by adding eigenvectors E15 and E16, and the CCW counterpart is shown in figure 6.7(b), formed by subtracting eigenvectors E15 and E16 respectively. Figure 6.8 shows other complex eigenvectors E11 and E12 occurring as conjugate pairs for the same permanent islands in the cladding phase space. The imaginary parts of the eigenvectors E11 and E12

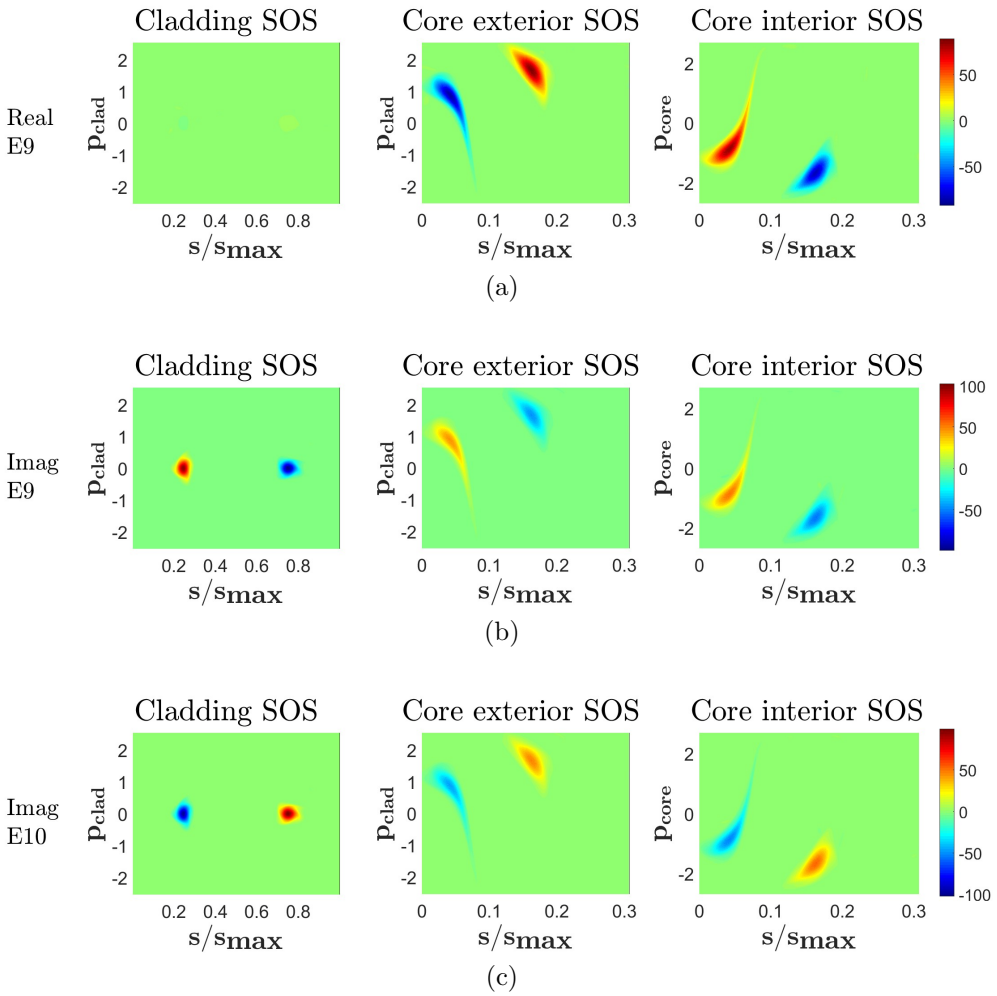


Figure 6.6: Phase variant eigenvectors corresponding to leaky resonances. (a) Real part of the 9^{th} leading eigenvector (Real E9). The real part of both E9 and E10 which have conjugate eigenvalues are identical, but their imaginary parts differ. Peaks in the imaginary part of (b) E9 and (c) E10 are phase shifted complements. The eigenvectors correspond to $\bar{T}_{2D}$ with $N = N_e = N_i = 300$, $n_c = 2.70$, and $n_{cl} = 2.55$.

are shown in figures 6.8(b) and (c) respectively, and indicate the phase associated with the resonant peaks in these periodic islands.

Steady state distribution using the 2D finite operator

According to the finite operator method, after a large number of iterations is performed using $\bar{T}_{2D}$, the distribution would converge towards the leading eigenvector E1 with eigenvalue equal to one; this is explained through equation 5.11 which was discussed in section 5.3.1. Therefore, all the permanent and leaky resonances in the pixelated phase space

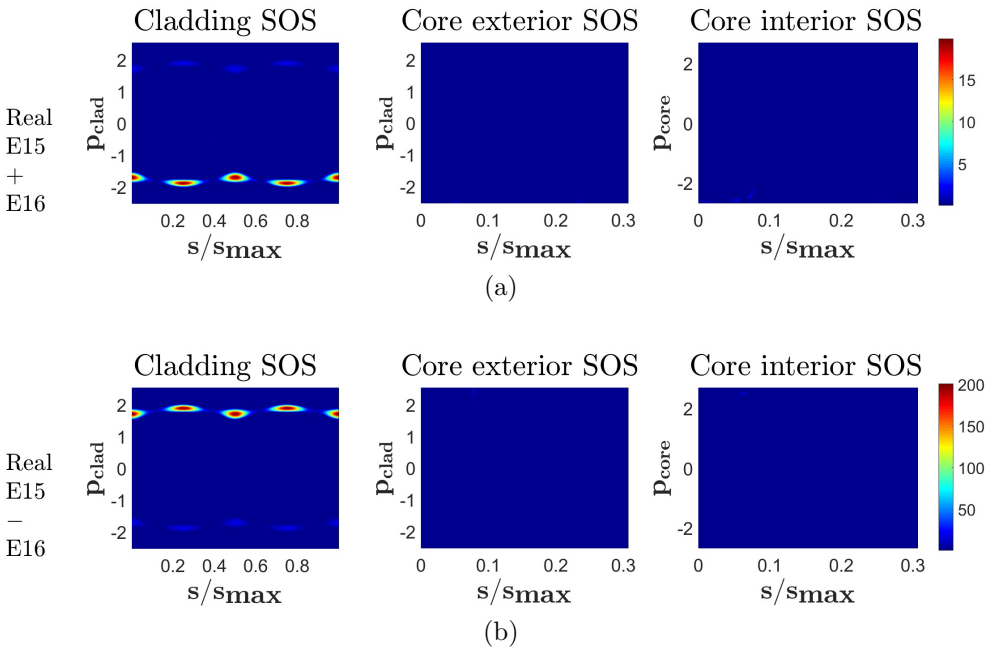


Figure 6.7: (a) Addition of the 15^{th} and 16^{th} eigenvectors of the $\bar{T}_{3D}$ reveals the CCW permanent regular islands in the cladding SOS. (b) The subtraction of the same pair of eigenvectors reveals the CW counterpart.

are subjected to decay. There is a limited number of reflections that can be observed for the evolution of the light distribution in the pixelated phase space. After a finite number of reflections, the contributions of the leading eigenvectors that characterise physical phenomena in the phase space are retained once the transients have settled down. However, the permanent resonances of the system decay by diffusion as a result of pixelation artefacts when the iterations are continued.

In other words, the permanent resonances are retained only within a limited observation window. The leaky resonances are subject to natural scattering process by reflections at the core boundary, and with enough iterations, the intensities trapped in leaky resonances would extinguish in the chaotic sea. A complication arises when the contrast between the core and cladding refractive indices is so low that the rate of reflective scattering is lower than the rate of diffusion. This means that the permanent resonances are scattered faster than the leaky resonances. This is apparent in the eigen-analysis of $\bar{T}_{2D}$, where the eigenvalue corresponding to E6 of a leaky resonance is higher than the eigenvalue of E11 associated with a permanent resonance. As a result, the permanent resonances, as

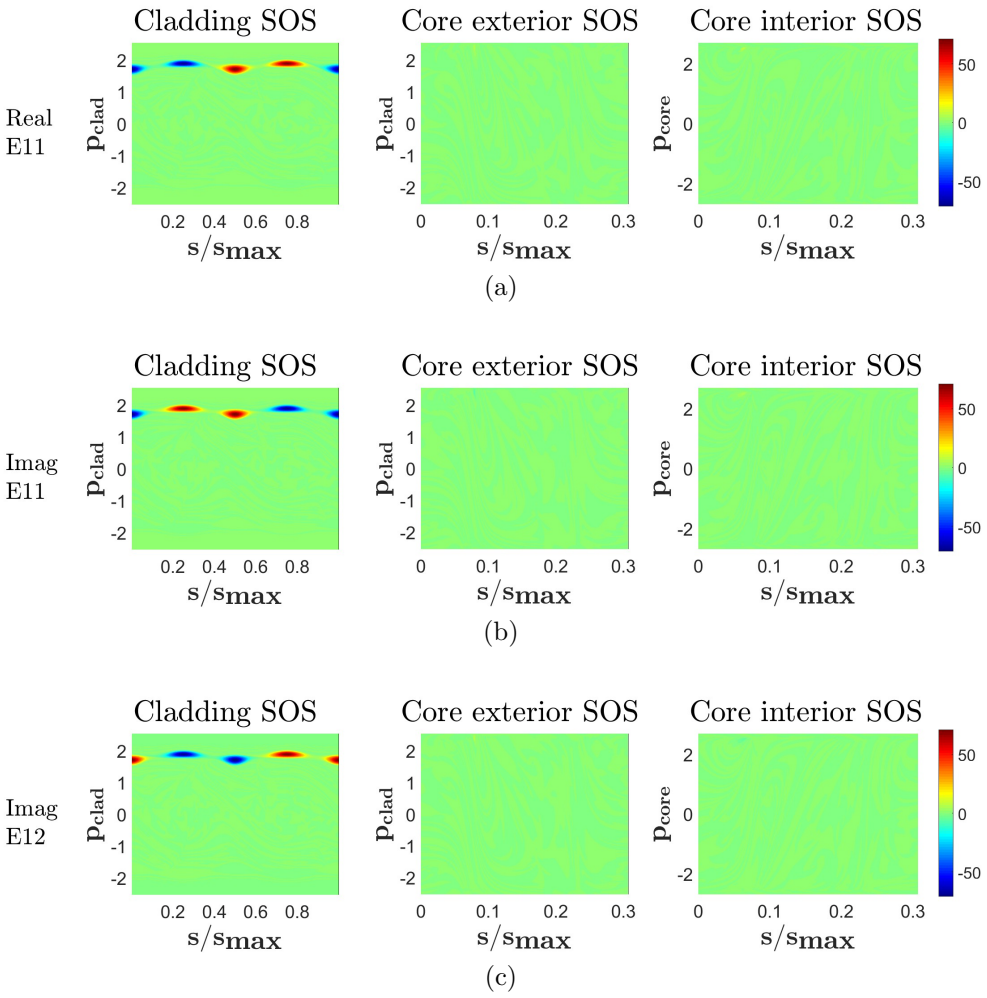


Figure 6.8: Phase variant eigenvectors corresponding to permanent island resonances. (a) Real part of 11^{th} leading eigenvector. Imaginary part of (b) 11^{th} and (c) 12^{th} eigenvectors which are phase-shifted complements.

shown by the eigenvectors of figures 6.7 and 6.8, decay faster during the propagation of a light distribution, than the leaky resonances shown by the eigenvectors in figures 6.5 and 6.6. Therefore, it is not possible to create an observation window in which the dominant permanent resonances are retained but the leaky resonances have relaxed.

The only way to overcome this distortion in the phase space is to increase the resolution of the pixelated phase space. This will in effect decrease the rate of diffusion while maintaining the rate of decay of the leaky resonance. In the eigenspace, the contribution of E11 would become greater than the contribution of E6, as the corresponding eigenvalue of E11 will becomes greater than that of E6. Therefore, by increasing the resolution, a observation window can be formed, at the end of which the finite operator method would be able to produce a steady state with all the transients relaxed and all permanent resonances maintained. This is studied further in the next section.

6.3 Variation of the phase space resolution and refractive indices of the fibre

In the finite operator method, when $\bar{T}_{2D}$ is constructed using a SIF cross-section it captures the resonant features of the SIF phase spaces. Resonant patterns appear among the leading eigenvectors of $\bar{T}_{2D}$ as investigated in the previous section. The presence of a core in the cladding medium causes scattering of some regular regions in the cladding phase space and results in an expansion of the chaotic sea.

The decay of power from permanent regular regions occurs due to diffusion, whereas the decay in leaky resonances, as discussed in the previous section, occurs due to a physical scattering process by the core medium. The two mechanisms of decay can be controlled by altering different modelling parameters. Firstly, the rate of diffusion by the pixelation artefact is controlled by changing individual pixel area; a finer pixelation leads to a slower rate of diffusion from the regular regions in the phase space. Secondly, the rate of scatter-

ing of the leaky resonances is affected if the refractive indices of the core and cladding are altered. A higher refractive index contrast between the core and cladding would result in more scattering at each reflection at the core boundary and the leaky resonances would decay faster.

Although changing the refractive indices of the SIF requires the fabrication of a new fibre, the parameters are easily alterable in the modelling. In order to change refractive indices in a post-process step, it is important to distinguish between light distribution incident at the boundaries of the fibre and the distribution leaving the boundaries. Let any distribution leaving the boundary be denoted with a '-' sign and any distribution arriving at the boundary be denoted by a '+' sign. Let, $\mathcal{R}$ be a reflection and transmission function at the boundaries that converts an incident light distribution, $\bar{f}_m^+$, after the m^{th} reflection into a distribution $\bar{f}_m^-$, that leaves the boundaries such that

$$\bar{f}_m^- = \mathcal{R}\bar{f}_m^+. \tag{6.1}$$

Let, a transport operator $\bar{T}_{tr}$, be defined which takes the distribution in the m^{th} reflection to a distribution incident at the boundaries for $(m+1)^{th}$ reflection, so that

$$\bar{f}_{m+1}^+ = \bar{T}_{tr}\bar{f}_m^-. \tag{6.2}$$

In terms of the transport and reflection operators, and the momentum p_i, equation 4.14 in chapter 4 is given by

$$\begin{aligned} \bar{f}_{m+1}^-(s, p_i, \beta) &= \bar{T}_{3D}\bar{f}_m^-(s, p_i, \beta) && (6.3)\\ &= e^{-\beta\Delta z(s,p_i)}\mathcal{R}\bar{T}_{tr}\bar{f}_m^-(s, p_i, \beta), && (6.4) \end{aligned}$$

where,

$$\bar{T}_{2D} = \mathcal{R}\bar{T}_{tr}. \tag{6.5}$$

In this chapter, $\Delta z(s, p_i) = 0$ for all rays as $p_z = 0$, and the phase spaces are only showing

rays confined in a 2D cross-section of the fibre. Rays having z-directional components for non-zero p_z will be discussed in chapter 7 which will involve the full 3D finite operator, $\bar{T}_{3D}$. Here, defining a light distribution in terms of incident and reflected parts respectively allows $\mathcal{R}$ to be isolated and various phase space distributions can be observed by varying the refractive indices of the SIF media, which only affects $\mathcal{R}$. Therefore, the rate of scattering of the leaky resonances can be altered in the present modelling without affecting the rate of decay by diffusion. The process does not require the calculation of a new $\bar{T}_{tr}$ each time and so the computationally burdensome process of ray-tracing required for construction can be avoided. Therefore, it is easy in the finite operator method to alter the refractive indices n_c, and n_{cl} of the core and cladding respectively to investigate the effect on the resulting phase spaces. In section 6.3.2, the variation of the rate of scattering from leaky resonances is investigated with the variation of n_{cl}, while keeping n_{c} constant.

However, as discussed in subsection 6.2.2, the only way to obtain an observation window when there is a weak decay rate in the leaky resonances is to make the rate of decay associated with diffusion even weaker. This is only possible by finer phase space resolution which requires the alteration of individual pixel size and the re-evaluation of $\bar{T}_{2D}$. When using the smaller pixel size, the dimensions of $\bar{T}_{2D}$ increase, and its formation requires more computational effort because more ray-tracing is involved. In the following section, the analysis is done for two different phase space resolutions with $N = N_e = N_i$ to make the rate of diffusion due to pixelation artefact weaker than the rate of decay of leaky resonances in the SIF.

6.3.1 The effect of a finer resolution in the coarse-grained phase space

In subsection 6.2.2, the eigen-decomposition of $\bar{T}_{2D}$ with $N = N_e = N_i = 300$ revealed that the magnitude of the eigenvalue corresponding to the leaky resonance was larger than the eigenvalue corresponding to a permanent resonance. This meant that the permanent resonance diffused into the chaotic sea faster than the decay of leaky resonance during

the evolution of the distribution. It is desirable that the effects of the diffusion artefacts remain weaker than that of the leaky resonances so that the latter diminishes completely, and an approximate steady state can be reached. Once the steady state is reached, the finite operator iterations can be halted to minimise further diffusion, and this forms the observation window.

To that end, the pixel count was increased by setting $N = N_e = N_i = 800$, and figure 6.9 shows the comparison between the phase spaces with lower (figure 6.9(a)) and higher (figure 6.9(b)) resolutions. The phase space is shown after 2000 reflections from an excitation of an uniform distribution in the cladding, which is a continuation of the evolution of the distribution presented in figure 6.1 in section 6.2. Figure 6.9(a) shows that the leaky resonance corresponding to the eigenvector E6 in figure 6.5 has scattered completely, along with the permanent island resonances corresponding to eigenvectors E11 and E12 of figure 6.8. However, when the resolution is increased, figure 6.9(b) shows that the permanent island resonances are retained with the leaky resonance fully decayed. Therefore, the iterations can be truncated at this stage so as to retain an approximate steady state distribution and form the observation window before pixelation artefacts take over. This comparison further augments the assumption that the leaky resonances have a different scattering mechanism than that of the permanent resonances in the phase space of the SIF.

6.3.2 Controlling the leaky resonances by changing the cladding refractive index of the fibre

In the previous subsection, the rate of diffusion in the dynamics was altered by changing the resolution of the pixelated phase space. In this section, the resolution is kept constant but the refractive index contrast between the core and cladding is varied. This directly affects the rate of decay in leaky resonances without affecting the permanent resonances in the system. The resolution of the phase space is kept constant by setting $N = N_e = N_i = 300$, and the geometric features of the SIF cross-section are as detailed in section

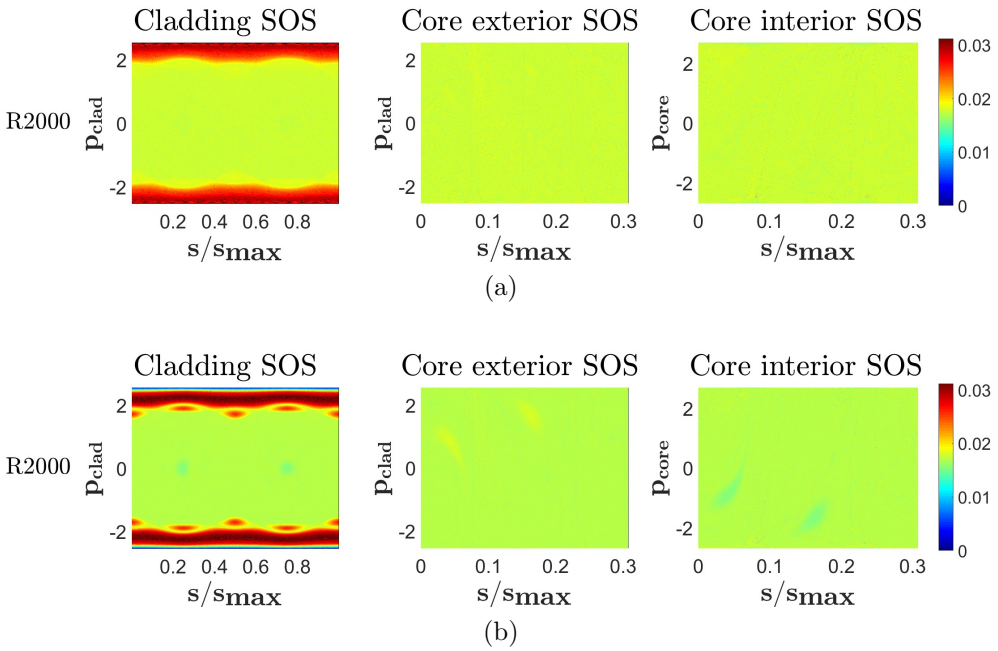


Figure 6.9: The phase space distribution from a uniform excitation in the cladding SOS after 2000 reflections with (a) $N = N_e = N_i = 300$ and (b) $N = N_e = N_i = 800$. The higher resolution allows the permanent island resonances in the cladding phase space to be retained while the leaky resonances decay completely.

6.2. Only the cladding refractive index of the SIF is varied, and for each case the effect on the eigen-spectrum of the $\bar{T}_{2D}$ matrix is investigated.

Four different values of n_{cl} are investigated. The refractive index of the core is kept constant at $n_c = 2.70$, and the eigenvalues of $\bar{T}_{2D}$ are evaluated. The differences are observed in the eigen-spectrum of $\bar{T}_{2D}$ as the refractive index of cladding is varied. In the first example, the refractive index contrast between the core and cladding is kept very low by setting $n_{cl} = 2.65$. The leading eigenvalues of the corresponding $\bar{T}_{2D}$ are shown in figure 6.10(a). The cladding refractive index is higher than the case studied with $n_{cl} = 2.55$ in section 6.2 and the eigenvalue spectrum in the complex plane is comparable to that shown in figure 6.2. The presence of eigenvalues $19 - 22$, and the shifts in the positions of eigenvalue 4 and 5, are among the major differences between the eigenvalues shown in figure 6.2.2 and those shown in figure 6.10(a). The five leading eigenvalues shown by the inset in figure 6.10(a) correspond to the permanent non-island regular regions in the cladding phase space, identical to those shown in figure 6.3. The permanent island resonances in

the cladding phase space and the leaky resonances of the system were identified in section 6.2.2. In this example, the eigenvalues of the leaky resonances are greater in magnitude than the eigenvalues of the permanent island resonances of the system. Figure 6.10(a) shows the dominant eigenvalues of the leaky resonances in blue, and those corresponding to the permanent island resonances in red. The 6^{th} largest real eigenvalue corresponds to the leaky resonance, whereas the 11^{th} largest eigenvalue corresponds to a permanent island resonance. Also, the contribution of the phase variant eigenvalues 7-10 of the leaky resonance are larger than the contributions of the corresponding phase variant eigenvalues 13-15 of the permanent island resonance. Therefore, the rate of scattering by the core is weaker than the rate of diffusion when $n_{cl} = 2.65$. As a result, the observation window cannot be accurately determined as the distribution becomes significantly distorted before the transients of the evolution could settle; a higher resolution is necessary in the phase space by lowering the pixel size to prevent this degeneracy.

The weak scattering by the core when $n_{cl} = 2.65$ has allowed more variants of the leaky resonance to linger for longer during the evolution. Eigenvectors E17-22 are all variants of E6, and figure 6.11(a) and (b) reveals real valued eigenvectors E17 and E18. Figure 6.11(c) and (d) shows the imaginary part of the phase variant eigenvectors E18 and E19. Therefore, lowering the core-cladding refractive index contrast allows more variant regular motion in that region of the phase space and their contribution to the dynamics in the overall phase space increases. E6-10, and more variants E17-22 are all eigenvectors of leaky resonances, and E11-16 are the eigenvectors of the permanent island resonances in the cladding phase space. In comparison, in the case of $n_{cl} = 2.55$ in figure 6.2, E18-21 eigenvectors were more localised in the vicinities of E7-10 respectively.

In the next example, n_{cl} is set to 2.30, and the scattering rate of leaky resonance increases as the dielectric contrast between the core and cladding is larger. The resulting eigenvalues are shown in figure 6.10(b). In this case, the leading eigenvalues 6-9 now correspond to the permanent island resonances in the cladding phase space and the eigenvalues of the leaky resonance have been relegated to eigenvectors 12-16. Real and imaginary parts of E6 are shown in figure 6.12(a) and (b) respectively and real and imaginary parts of E12

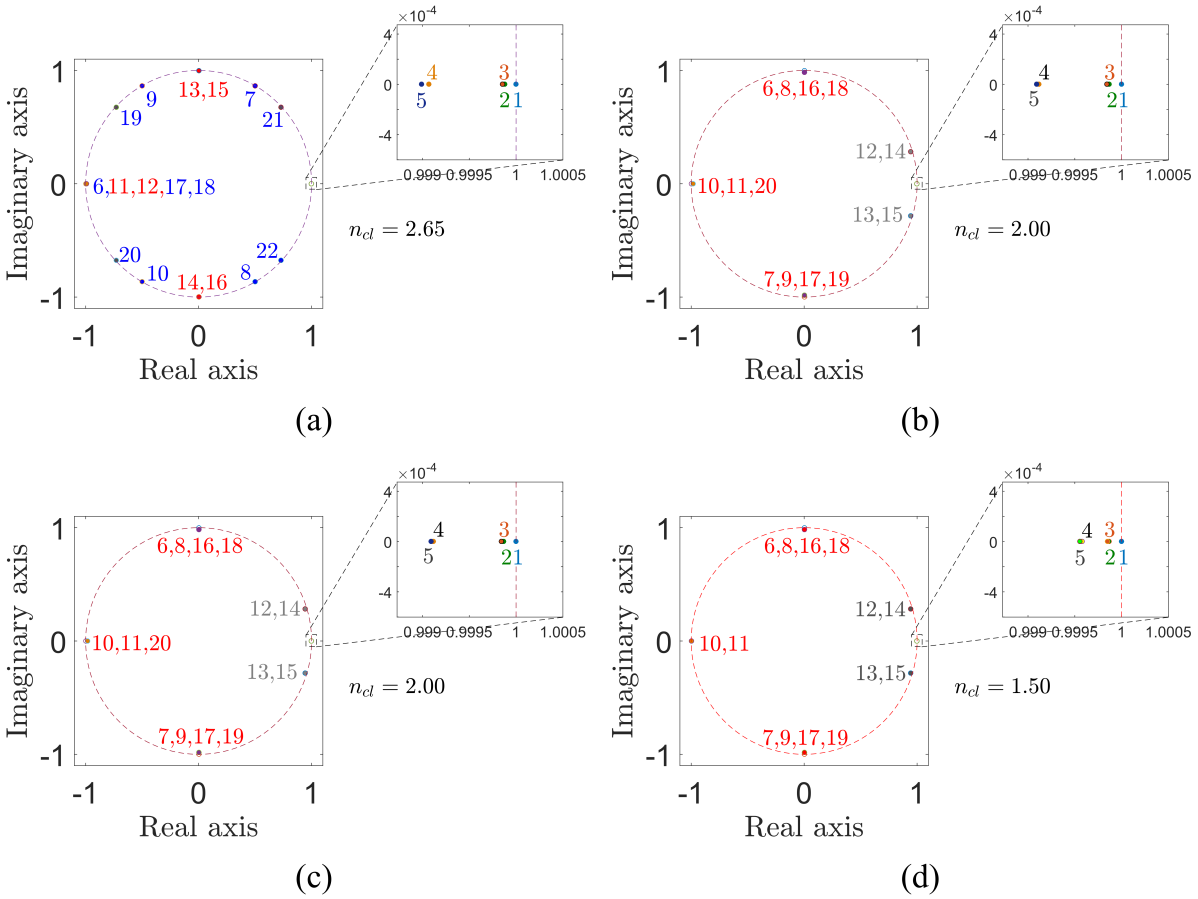


Figure 6.10: Variation of the eigenvalues of $\bar{T}_{2D}$ with the change in cladding refractive index. The refractive index of the core is $n_c = 2.70$ and the cladding refractive index is varied to investigate the scattering of leaky resonances. In (a) $n_{cl} = 2.65$ and index contrast with the core is very low, resulting in larger contribution of the leaky resonances than the permanent ones. In (b), $n_{cl} = 2.30$, and the permanent resonances have larger contribution than leaky resonances. In (c) $n_{cl} = 2.00$ and in (d) $n_{cl} = 1.50$ the contributions of the leaky resonances disappear from the largest eigenvalues. The resolution is kept constant by setting $N = N_e = N_i = 300$.

and E13 are shown in figure 6.12(c) and (d) respectively, to show the respective phase variants of the permanent island and leaky resonances. Moreover, the leading eigenvalues 17-20 now correspond to a different set of phase variant permanent resonances in the cladding phase space. The eigenvector associated with these eigenvalues corresponds to permanent whispering gallery resonances in the cladding phase space for $|p_{clad}| \approx n_{cl}$. On the other hand, the five largest eigenvalues still correspond to the same eigenvectors as shown in figure 6.3. In this example, since the refractive contrast between the core and cladding is high enough for leaky resonances to scatter faster than the rate of diffusion, it is possible to create an observation window after the transients have relaxed, without changing the chosen resolution of the pixelated phase space.

In the third example, the refractive index contrast is increased further by setting $n_{cl} = 2.00$. The leading eigenvalues of $\bar{T}_{2D}$ are shown in figure 6.10(c) and there are two major changes in the spectrum that result from this higher index contrast. Firstly, a regular region formed by the total internal reflection (TIR) in the core medium has emerged, as discussed in section 5.2 and shown as region B in figure 5.3(a). In the complex plane in the inset of figure 6.10(c) the eigenvalues 4-5 now correspond to the regular TIR region of the core interior phase space. This pair of eigenvalues also forms CW-CCW independent motion around the core and the sum and difference of the associated phase space eigenvectors are shown in figure 6.13(a) and (b). In previous cases of lower refractive index contrasts between the core and cladding media, the area of this TIR region was very small and the eigen-analysis was unable to resolve any resonance in this region owing to the diffusion artefact. The power trapped in this region was also minute compared to the power trapped in other permanent resonances of the phase space. In this case, the higher index contrast expanded the TIR region of the core and the intensity trapped by region has now become significant enough for $\bar{T}_{2D}$ to pick up resonances there.

Secondly, the rate of scattering of trajectories by the core is so high that the leaky resonances are not seen among the largest eigenvectors any more; their eigenvalues are lower down in magnitude in the unit circle than the 20 leading ones shown in figure 6.10(c). Eigenvalues 6-11, and 16-20 are all contributions of the permanent resonant islands in

the cladding phase space. Therefore, there is no need to increase the resolution of the phase space and the observation window is obtainable. Figure 6.13(c) and (d) shows real and imaginary parts of the new phase variant eigenvectors E16 and E17 respectively, that were less prominent before. Eigenvalues 12-15 in figure 6.10(b) are the whispering gallery resonant regions in the cladding phase space, and they have also increased in prominence in the dynamics compared to the previous example where they appeared as eigenvalues in the range 17-20 in figure 6.10(b).

In the final example, the refractive index of the cladding is set to $n_{cl} = 1.50$. Such a large refractive index contrast between the core and cladding is viewed as not realistic, but is used in the modelling to show the effect on the phase space dynamics. The TIR region in the core interior phase space has expanded more and the corresponding eigenvalues 4 and 5 have increased in magnitude as shown in figure 6.10(d). The addition of the corresponding real eigenvectors results in the CW independent motion as shown in figure 6.14(a) and the distribution includes the regular regions of the cladding phase space as well. The CCW counterpart obtained by subtracting E4 and E5 is shown in figure 6.14(b). The leading eigenvalues shown in figure 6.10(c) and (d) all correspond to the permanent resonances of the system, and leaky resonances have become insignificant as they decay very rapidly.

In summary, the variation in the refractive index of the cladding was investigated and the resulting changes in the dynamical system in the phase space of the SIF were outlined in this subsection. Changing the cladding refractive index by keeping the core refractive index constant has resulted in a change in the amount of scattering of rays by the core. The resolution of the pixelated phase space was kept constant while the refractive index contrast between the core and the cladding was varied. A higher refractive index contrast caused more scattering and the power trapped in leaky resonances decayed faster. Both permanent and leaky resonances in the system eventually decay if the dynamical system is allowed to evolve, but in order to evaluate the observation window, the leaky resonances must have a higher rate of decay than the permanent resonances. This was achieved by varying the refractive index contrast between the core and cladding of the SIF for a fixed

pixelation.

6.4 Chapter summary

In this chapter, the evolution of the light distribution was investigated in a deformed SIF. It was possible to vary the characteristics of the dynamical system in the intensity map by varying the modelling parameters involved. In this chapter, the two parameters varied in the model were the resolution of the pixelated phase space, and the refractive index of the cladding medium to change the refractive index contrast between the core and the cladding in the SIF. These changes affected the dynamical system in two different ways. Firstly, the increase in phase space resolution decreased the rate of diffusion in the dynamics and thus increased in the observation window within which the phase space evolution can be observed. Secondly, for the same resolution, increasing the contrast between the refractive indices of the core and cladding media resulted in a faster scattering of leaky resonances, and the diffusion-free steady-state was reached within a smaller number of reflections. Faster convergence allowed the observation window to be set shorter and the diffusion artefacts that slowly engulf the permanent resonances in the mixed phase space to be avoided. Tweaking these parameters allow for better modelling outcomes, and in the following chapter these results will be used towards the measurement the captured power in the core using the finite operator model.

The finite resolution of the pixelated map causes diffusion in the regular regions of the phase space, owing to the finite area of the pixels. In the limit the pixel area goes to zero leading to an infinite resolution in the phase space, the diffusion artefact would cease to exist and the operator method would become identical to ray tracing. The resulting $\bar{T}_{2D}$ for a zero-pixel-area would however be of infinite dimension. Numerically, the resolution has to be finite and so all regular regions in the pixelated phase space are subject to diffusion artefacts. This means that the resonant power trapped in the regular regions of the phase would eventually escape into the chaotic sea and the steady state phase space

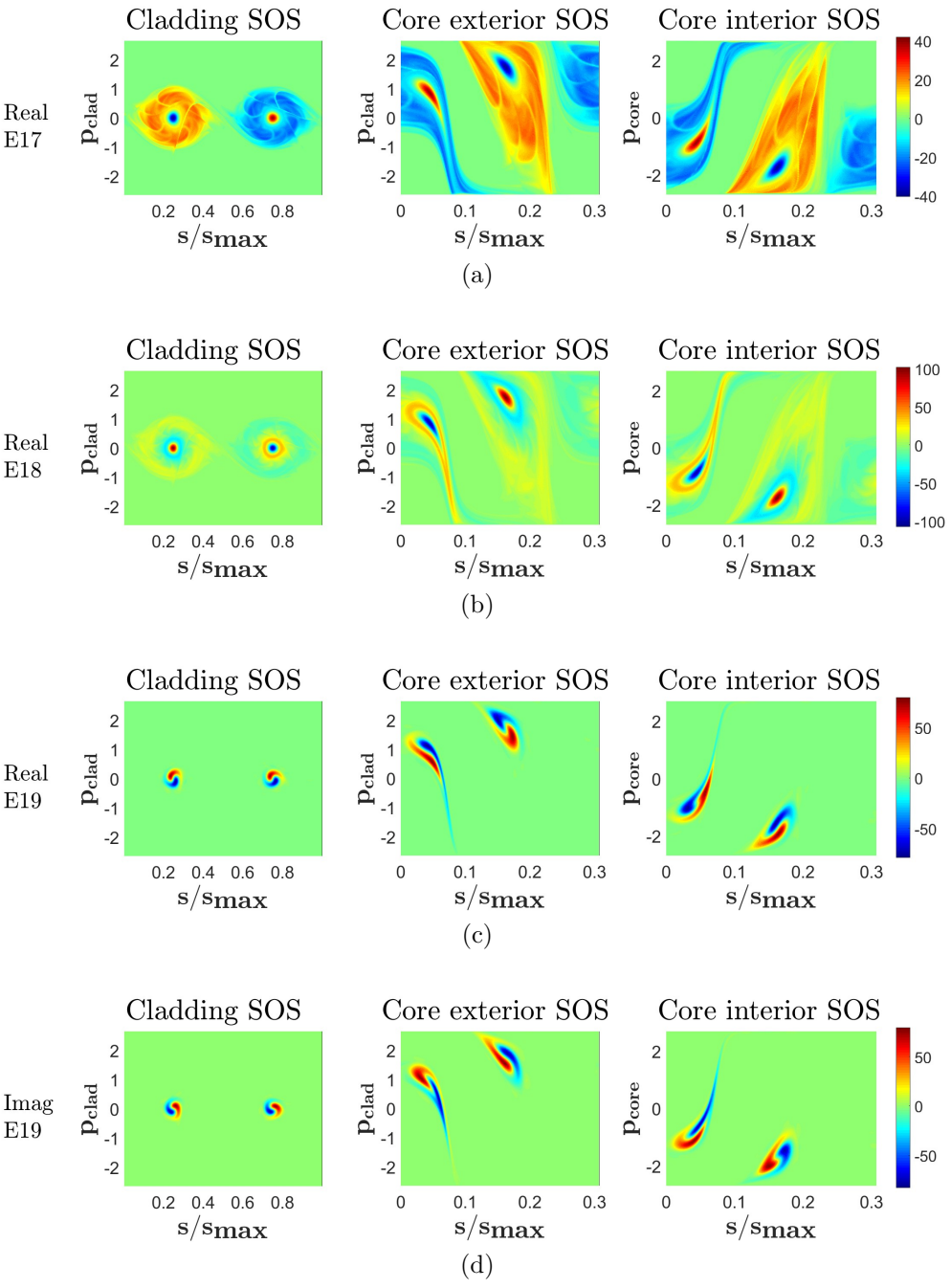


Figure 6.11: More phase shifted variant eigenvectors of leaky resonances become prominent with $n_{cl} = 2.65$, $n_c = 2.70$ due to low scattering rate by the core.

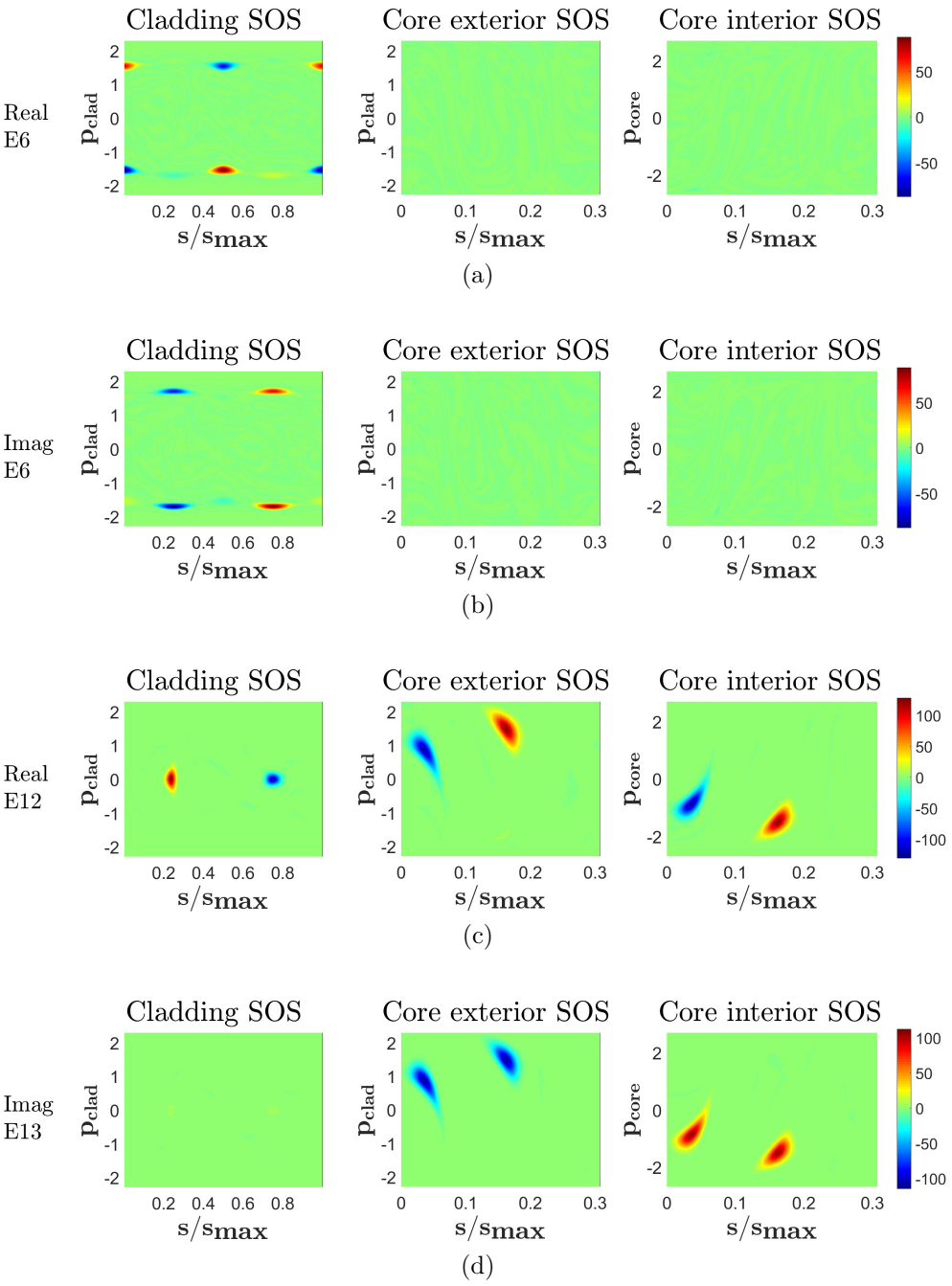


Figure 6.12: The eigenvectors of the permanent island resonances in the system has become more prominent than leaky resonances. Phase shifted (a) real part and (b) imaginary part of E6. The eigenvectors of the leaky resonances have relegated and (c) shows the real part of E12 and (d) shows the phase shifted imaginary part of E13, in the system with$n_{cl} = 2.30$, $n_c = 2.70$.

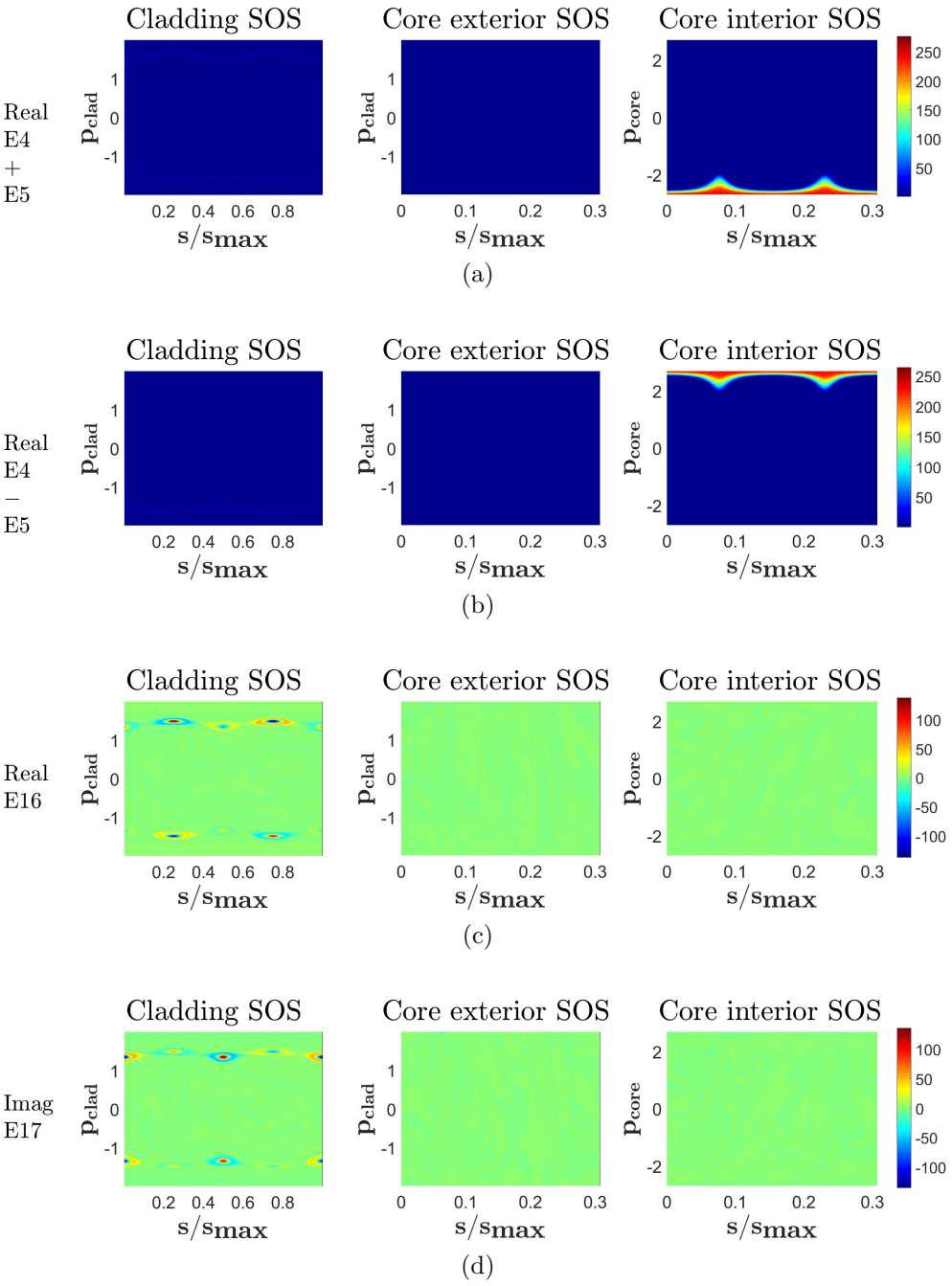


Figure 6.13: Higher refractive index contrast caused the TIR region of the core interior phase space to expand and as a result E4 and E5 pairs correspond to the permanent resonance in the core interior SOS. (a) CW and (b) CCW counterparts of the E4 and E5 pair. The higher refractive index contrast allows the contribution of more variants of the permanent island resonance in the cladding. Such contributions include the phase variant (c) real E16 and complementary (d) imaginary E17, in the system with $n_{cl} = 2.00$, $n_c = 2.70$.

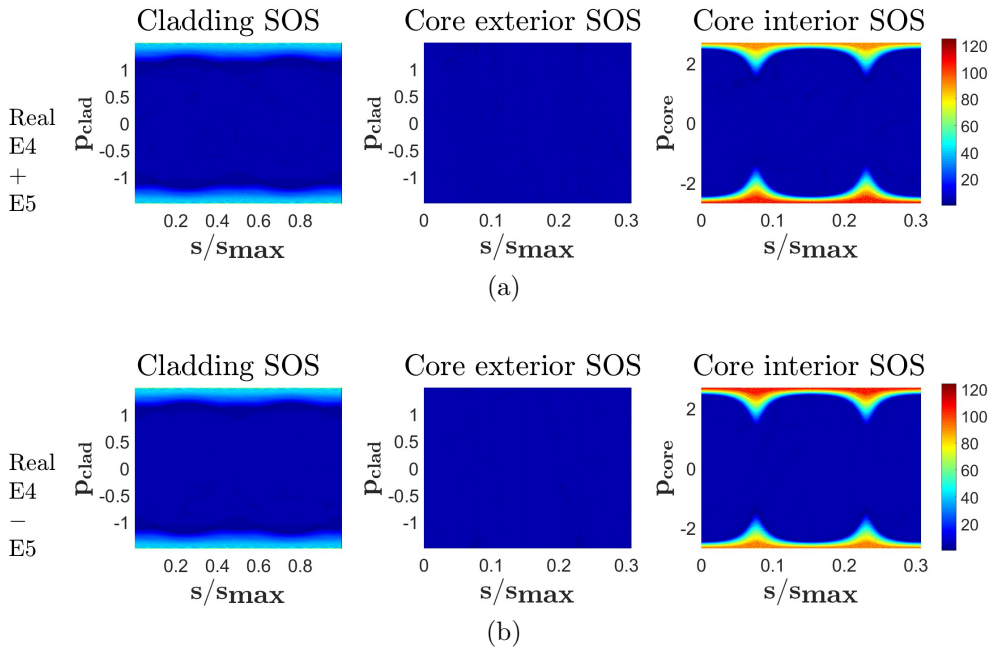


Figure 6.14: The permanent resonant region in the core interior SOS expands further as the refractive index contrast between the core and cladding increases, with $n_{cl} = 1.50$, and $n_c = 2.70$.

after an indefinite number of iterations by the finite operator would result in a uniform distribution in the phase space. In order to prevent this, the iterations are truncated before too much power escapes from the regular regions and an approximate steady state distribution is obtained when the intensity is stabilised in the chaotic sea. Therefore, the observation window is created, in terms of a number of reflections, for which the iterations by the finite operator are carried out. A complication which arises during this process is when there are slowly decaying physical resonances in the dynamics.

One particular phenomenon, discussed in this chapter, that causes interference with the evaluation of the observation window was the leaky resonances. The power trapped in leaky resonances is scattered by the core dielectric boundary upon each successive reflection, which is a physical phenomenon and is not related to the diffusion artefact. The decay from leaky resonances depends on the refractive index contrast between the core and cladding. If this contrast is very low, the decay rate is slower and the leaky resonances linger in the dynamics and mimic leakages from permanent resonances. Since the decay of leaky resonances are not related to phase space pixelation, the resolution

was increased in the phase space by making smaller pixel sizes in order to slow down the diffusion decay rate while keeping the decay of leaky resonances constant. This caused the power in the leaky resonances to decay first, i.e. before the diffusion artefacts started distorting the regular regions. The leaky resonances are a part of the transient stage of the dynamics and their slow decay requires a long observation window. However, for a given resolution (pixel size) there is a finite number of reflections that can be carried out before which the diffusion artefacts start becoming prominent. The observation window is created by terminating the number of reflections carried out to limit diffusion, and this window can only be expanded by finer resolution. If the relaxation rate of the leaky resonances is slow, the finer resolution allows enough iterations to be performed before setting an observation window by truncation.

On the other hand, as mentioned earlier, the decay rate of the leaky resonances is itself varied by changing the refractive index contrast between the core and cladding while keeping the rate of diffusion in the overall phase space to be constant. Changes in the eigen-spectrum of the associated $\bar{T}_{2D}$ were observed. It was shown that, as the refractive index contrast increased, the contribution of the leading eigenvectors corresponding to leaky resonances diminished from the overall distribution. The resolution of the phase space remained unchanged, and for a constant rate of diffusion it allowed the observation window itself to be shortened for a particular phase space resolution as the refractive index contrast increased.

Therefore the finite operator model facilitates the alteration of one or more modelling parameters in order to change the dynamics of the light distribution in the SIF. It provides fresh insight into how the light distribution in deformed fibres can be evaluated. In the following chapter, the concept of the observation window introduced in this chapter is applied in context of the measurement of the net accumulation of power in the core. The analysis of the finite operator is extended to 3D, with the application of the finite $\bar{T}_{3D}$ on various light distributions. The variation of the accumulation of power in the core is investigated in relation to the various deformations applied to the boundaries of the core and cladding in the SIF.

Chapter 7

The net power accumulation in the core in step-index fibres

7.1 Introduction

In this chapter, a method to calculate the net accumulation of power in the core is developed for step index fibres (SIFs) with circular core and cladding cross-sectional boundaries. The finite operator method is applied to 3D SIFs to calculate the net power accumulation in the core after propagation along an arbitrarily long length of the fibre. The finite operator applied to optical fibres was developed in chapter 4, where an operator $\bar{T}_{3D}$ was defined that enabled the propagation of a light distribution, $f_m(s, p, z, p_z)$ through successive reflections, m, at the boundaries in a pixelated phase space. The definition of momentum, p, was modified in chapter 5 to $\bar{p}_i$, so that rays propagating in 3D and in different dielectric media in the SIF can be modelled. The finite operator model applied to 3D rays also provides a numerically efficient way to measure the power captured in the SIF core as will be described in this chapter.

The finite operator can be constructed to model light propagation in any SIFs with circular or deformed cross-sectional boundaries. The properties of the 2D operator were investigated in chapter 6 and the evolution of light distribution was visualised using the

pixelated phase spaces. It was found that the rectangular pixelation of the phase spaces caused diffusion artefacts in the dynamics and distorted the regular regions in the mixed phase spaces. So the iterations by the operator were required to be truncated in order and it was concluded that the rate of diffusion must be minimised by making finer phase space pixelation. Finer pixelation however makes the problem more computationally intensive.

In this chapter, a quantitative measure of the diffusion process will be described in section 7.2 in context of the power accumulation in the core of SIFs. The net transfer of power into the core is affected by the diffusion artefacts and will be measured after each reflection at the boundaries. Because of diffusion, a method to estimate the net power accumulation in the core after a limited number of reflections will be developed. To aid such estimations, special cases will be investigated, such as a toy model which restricts rays in a 2D axial cross-section of the fibre discussed in section 7.3.1, and SIFs with circular core and cladding boundaries, discussed in section 7.3.2. Diffusion is absent in the toy model and, in the circular core/cladding SIF. These diffusion-free dynamical systems will serve as a benchmark for the calculation of the net accumulation of power in the core for more generic SIFs with deformed core/cladding boundaries. The estimation of the net power accumulation in the core of a deformed SIF is discussed in section 7.3.3.

7.2 Diffusion measurement

The finite operator method allows one to monitor flux transfer across the core boundary to capture the power carried by rays moving in to and coming out of the core. The detailed calculation is set out in the next section but here a simplified version of the power transfer problem is discussed using only the 2D finite operator, $\bar{T}_{2D}$, to establish limitations placed by diffusion in the rectangularly pixelated phase space.

Power enters the core when an distribution incident on the core exterior boundary is transmitted through. Power leaves the core when a distribution incident on the core interior boundary is transmitted out. These combine to provide the net transfer of power

into the core. The procedure is illustrated in this section for the special case of $\beta = 0$, and therefore in an effectively 2D setting in which

$$\bar{T}_{3\mathrm{D}} \to \bar{T}_{2D}.$$

The transmittance and reflectance matrix, $\mathcal{R}$, defined in section 6.3, consists of 3×3 block matrices and is given by

$$\mathcal{R} = \begin{bmatrix} 1 & 0 & 0 \\ 0 & R_{ext}(s, \bar{p}_{\mathrm{clad}}) & T_{int}(s, \bar{p}_{\mathrm{core}}) \\ 0 & T_{ext}(s, \bar{p}_{\mathrm{clad}}) & R_{int}(s, \bar{p}_{\mathrm{core}}) \end{bmatrix} \tag{7.1}$$

where R_{ext} and T_{ext} are respectively the reflectance and transmittance functions at the core exterior boundary, and R_{int} and T_{int} are likewise the reflectance and transmittance functions respectively at the core interior boundary, all of which are dependant on the coordinates $(s, \bar{p}_i)$ (with $i = \mathrm{core/clad}$).

The net transfer of power from the cladding to the core at the m^{th} reflection in this simplified 2D problem is then given as

$$\Delta\Phi^m_{2D} = \langle w, f_m \rangle, \tag{7.2}$$

where

$$w(s, \bar{p}_i) = \begin{cases} 0 & \text{on cladding SOS} \\ T_{int} & \text{on core exterior SOS} \\ -T_{ext} & \text{on core interior SOS} \end{cases} \tag{7.3}$$

and $f_m(s, \bar{p}_i)$ is the density of rays arriving at the corresponding boundary. The cumulative

transfer of power, up to and including M reflections, is given by

$$\begin{aligned}\Phi_{2\mathrm{D}}^{M} &= \sum_{m=0}^{M} \Delta\Phi_{2D}^{m}, \\ &= \sum_{m=0}^{M} \langle w, \bar{T}_{2D}^{m} f_0 \rangle. \end{aligned} \tag{7.4}$$

The quantity of interest in applications is the net transfer of power over the entire length of the fibre. The limit

$$\Phi_{2\mathrm{D}} = \lim_{M\to\infty} \sum_{m=0}^{M} \Phi_{2D}^{M}, \tag{7.5}$$

is related to this quantity but is not the same, as will be discussed more fully in the next section, because it orders power transfer by the number of bounces rather than distance z along the fibre. It is used in this section, however, to illustrate the limitations placed on simulations by diffusive effects. The approach to $\Phi_{2\mathrm{D}}$ is emphasised as a limit in (7.5) for two reasons.

1 The limit exists even though its formal geometric sum

$$\Phi_{2\mathrm{D}} = \langle w, (I - T_{2D})^{-1} f_0 \rangle \tag{7.6}$$

is ill-defined because the largest eigenvalue of T_{2D} is equal to 1. The geometric sum can be regularized, as w is necessarily orthogonal to the subspace corresponding to unit eigenvalue, but this procedure requires further discussion, as provided in the next section.

2 More importantly from a practical point of view, unphysical diffusion artefacts may dominate the formal limit $M \to \infty$ when the core or cladding is deformed. In such applications, M is therefore restricted to values for which diffusion has a sufficiently small impact. Estimation of appropriate bounds for M is the subject of the rest of this subsection.

The effects of diffusion will be illustrated using two types of SIF. The first is the SIF with

circular core and circular cladding with insignificant diffusion to serve as a benchmark. The second is the deformed SIF which is intended to be representative of generic problems where diffusion plays a more prominent role. The benchmark SIF has a circular core positioned non-concentrically in a circular cladding so that the dynamics has significant chaotic components. Here diffusion artefacts are confined to horizontal bands of pixels situated at the borders between chaotic and regular regions of core and cladding SOSs as will be discussed in the following subsection.

7.2.1 Propagation in a step-index fibre with circular core and cladding boundaries.

Figure 7.1(a) shows the first example of a SIF where the outer cladding boundary is a unit circle, and the core is circular with radius $r = 0.2828$, centered at $(0.1, 0.3)$. The area of the core is 8% of the cross-sectional area of the cladding. The refractive index of the core is taken to be $n_c = 2.70$ and that of the cladding medium is taken to be $n_{cl} = 2.55$, typical of MIR-transparent chalcogenide glasses.

As shown in figure 7.1(b), a light distribution originating only from the cladding boundary and uniformly distributed in the cladding SOS is taken as an initial excitation. The light distribution reaches a steady state after 450 iterations. The light distribution propagating in the fiber is shown in the SOSs for the 30^{th} (marked as 1), 100^{th} (marked as 2), and the 450^{th} (marked as 3) reflection. When the steady state is reached, the SOSs show three distinct regions. The cladding SOS and the core interior SOS form two disconnected regular regions, and there is a chaotic sea that spans all three SOSs.

These distinct regions exists for any initial light excitation, but the intensity trapped in these regions varies according to where the light was initially excited. The chaotic region occurs because of the trajectories scattered by the core (regions in green). The trajectories with higher value of $|\bar{p}_{\text{clad}}|$, which do not interact with the core, remain in the regular region of the cladding SOS (regions remaining red). Only scattered trajectories appear in

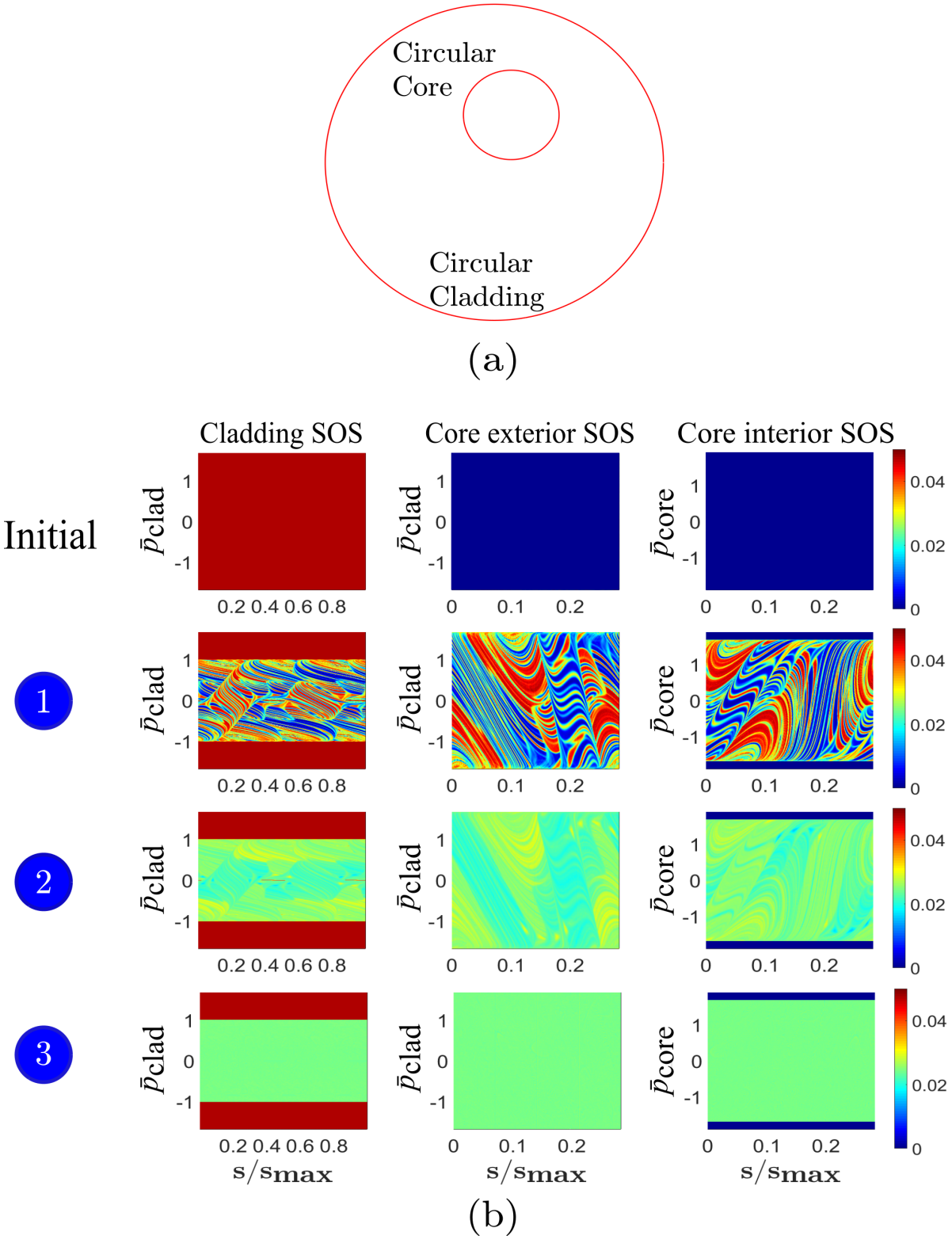


Figure 7.1: **(a)** An SIF cross-section with circular core and cladding boundaries. **(b)** Initially, an arbitrary uniform light distribution was excited from the cladding SOS and allowed to propagate in the fiber. SOS distributions are shown for the propagation after (1) 30^{th}, (2) 100^{th}, and (3) 450^{th} reflections.

the core exterior SOS and these are seen to be completely chaotic. The core interior SOS shows a regular region for trajectories with $|\bar{p}_{\text{core}}| \geq 2.55/2.70$ (regions shown in blue in the core interior SOS), and a chaotic region for lower $|\bar{p}_{\text{core}}|$ (shown in green). This regular region occurs for trajectories that can be trapped in the medium with higher index due to total internal reflection (TIR) and the region expands as the refractive index contrast between the core and the cladding medium increases. In figure 7.1, with the excitation only from the cladding SOS, the regular region in the core interior SOS is empty as it is not accessible by the trajectories coming in from the cladding medium. Owing to a sharp separation between the regular and chaotic regions in the circular SIF that is aligned with the pixelation scheme, the diffusion artefacts do not cause leakage in the intensity trapped in the regular regions.

7.2.2 Propagation in a deformed step-index fibre

In the second example of a deformed SIF, the propagation is more significantly affected by diffusion and the number of reflections cannot be made arbitrarily large. To illustrate this, the initial excitation from the cladding SOS is also propagated in a deformed SIF. Figure 7.2(a) shows the example of the deformed fibre with an elliptical core centred at $(0.1, 0.3)$, with $(0.4, 0.2)$ as its major and minor axes respectively, and the major axis oriented at an angle of 135°. The core has the same cross-sectional area as the core of the circular SIF in the previous example. The outer cladding boundary is also slightly deformed, and the deformation is introduced by defining the boundary with the quadrupolar equation and using $\epsilon = 0.05$. The resulting SOSs are mixed with the regular regions forming a complex network of invariant curves (ICs) embedded in a chaotic sea as shown in figure 7.2(b). The distribution is propagated for 10^3 reflections.

The light distribution is shown at four different stages in its evolution through the fiber in figure 7.2(b). At 30 reflections (marked as 1) the distribution is seen to be spreading in the available regular and chaotic regions of the SOSs. After 100 reflections (marked as 2), the trajectories have largely filled up the chaotic sea (regions shown in green), and there

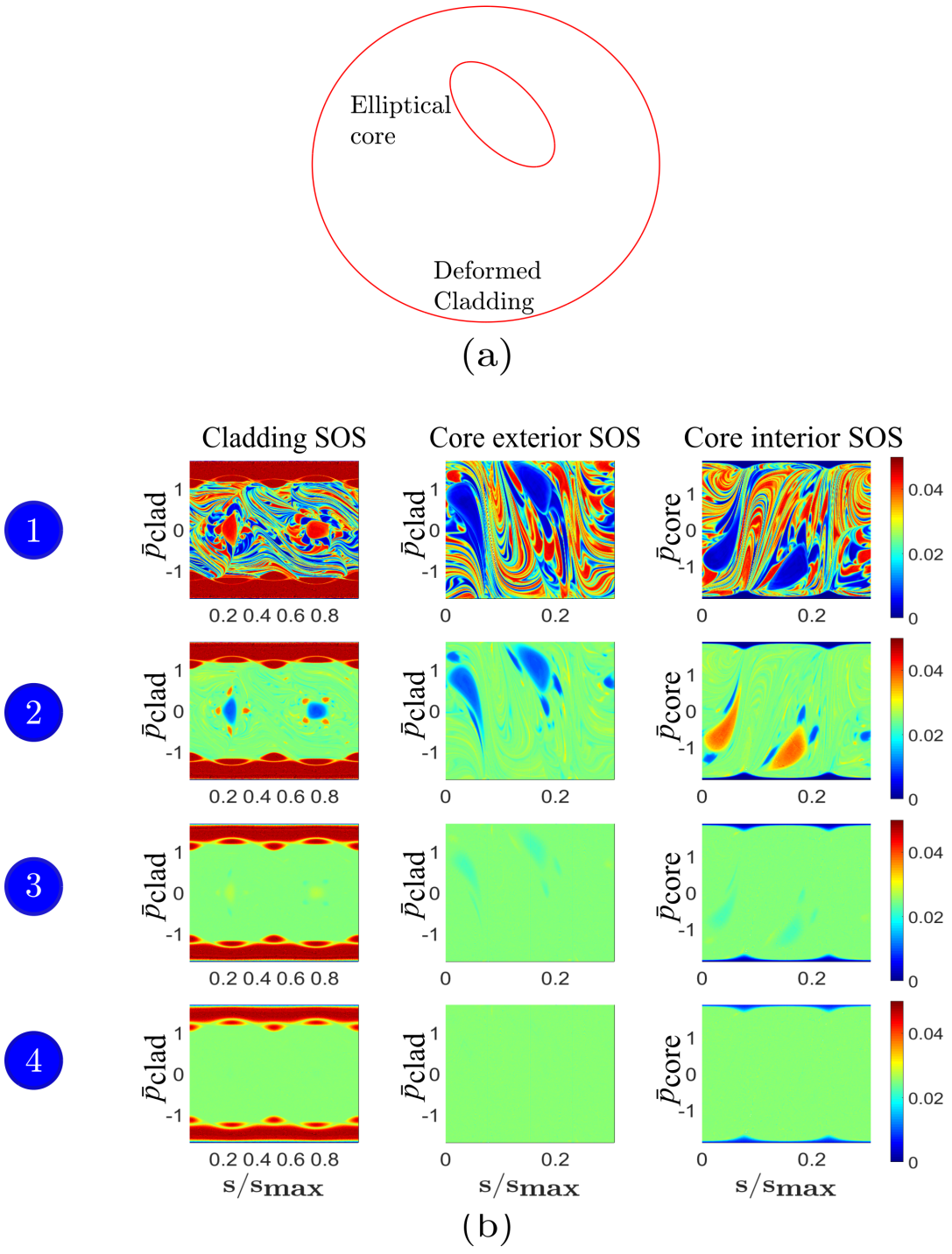


Figure 7.2: (a) A deformed SIF cross-section. (b) the evolution in the fiber of a uniform distribution launched from the cladding SOS. The SOS distributions are shown after (1) 30^{th}, (2) 100^{th}, (3) 450^{th}, and (4) 1000^{th} reflections.

are other regions in the SOSs occupied by various regular trajectories (shown in red in the cladding SOS, and in blue in the core interior SOS) for high $|\bar{p}_{\text{core}}|$. The light trapped in the regular regions of the cladding never hit the core, and likewise the regular regions of SOS(i) are not accessible to the trajectories arriving from the cladding. Therefore, no trajectories enter the regular region of the core interior boundary SOS as the initialization was only from SOS(c). Embedded in the middle of the chaotic sea are the short-lived leaky resonances where trajectories bounce in the SIF cross-section, around $s/s_{\max} = 0.25$ and $s/s_{\max} = 0.75$ and $\bar{p}_{\text{clad}} = 0$ and taking a path via the core medium. These pseudo-regular transient regions are scattered by weak reflections at the core cladding boundary and the intensity associated with them decays into the chaotic sea after successive reflections. By 450 reflections (marked as 3), the intensity trapped in leaky resonances has significantly relaxed into the chaotic sea, although some remnants still exist.

After 450 reflections, the transient dynamics in the SOSs have settled down, and distinct chaotic and regular regions have appeared. As the iterations are carried on further, for up to 1000 reflections (marked as 4), the edges of the regular regions are gradually starting to diffuse into the chaotic sea. Due to diffusion, the number of reflections performed by the finite operator must be truncated in order to prevent the leakage of power from the regular regions into the chaotic sea. In the following subsection, a quantitative measure of the rate of diffusion in the system is presented. The measurement is also essential to the aim of developing a method to obtain the net power accumulation in the core, which will be discussed in section 7.3.

7.2.3 2D net power accumulation in the core

The evolution of Φ_{2D}^{M} with M is shown in figure 7.3(a) for the benchmark problem of the SIF with circular core and cladding boundaries (the cross-section and the propagated light for this example was shown figure 7.1). It is seen that Φ_{2D}^{M} has effectively converged to its asymptotic value of $\Phi_{\text{2D}} \approx 0.146$ after the order of 100 reflections. Increasing pixel dimensions from $N = 200$ to $N = 1000$ leads to some convergence of this value towards a

limit, but does not qualitatively change the picture.

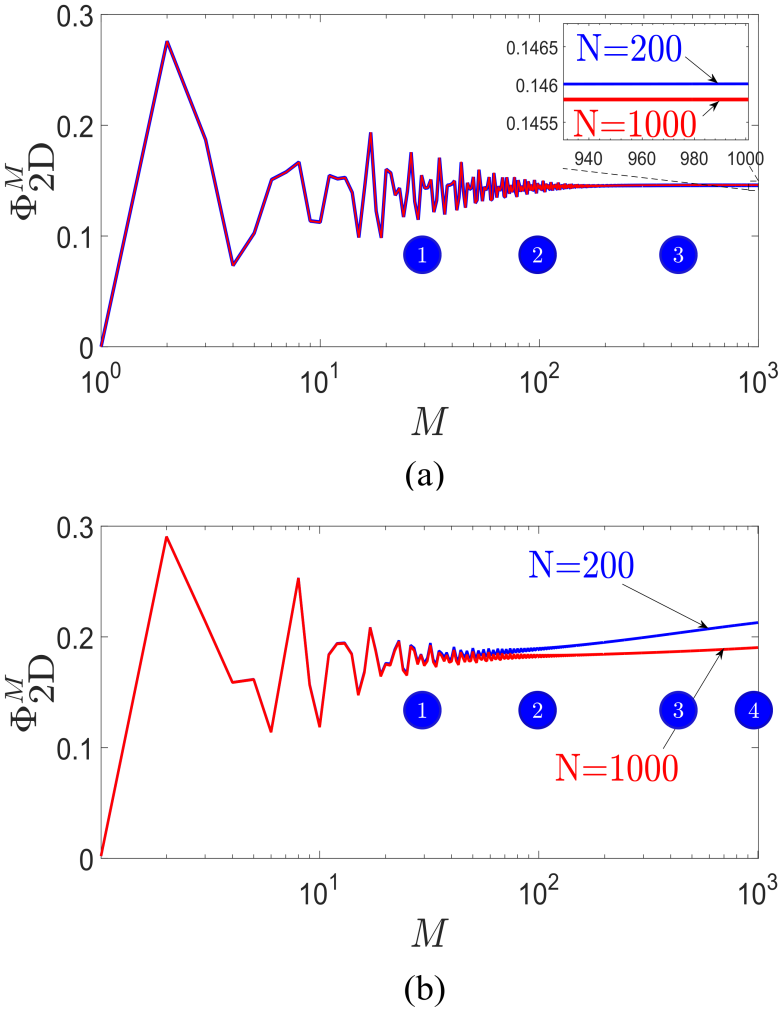


Figure 7.3: (a) Φ^M_{2D} calculated for SIF with circular core and cladding boundaries in figure 7.1.(b) Φ^M_{2D} calculated for the deformed SIF in figure 7.2

In figure 7.3(b) an equivalent calculation for a more generic example with deformed core and cladding is shown. Here the border between regular whispering gallery regions and chaotic regions is no longer horizontal in phase space (see Fig. 7.2) so there is diffusive transport between the two. Unlike for the benchmark problem, Φ^M_{2D} does not reach a simple plateau here, but continues to drift upwards even after the initial transients have died out for M between about 30 and about 100. Furthermore there is a marked difference between the calculations with $N = 200$ and with $N = 1000$, with the former showing significantly more drift. This is because diffusion due to pixelation allows power to enter the invariant and totally internally reflected whispering gallery regions. This is an non-physical effect which can be postponed to higher reflection numbers, but not eliminated,

by using finer pixelation. In practice, therefore, it is essential to restrict the calculations to values of M where these diffusion artefacts are not dominant. For the simulations illustrated in figure 7.3, calculations of flux become inaccurate once M is larger than a few hundred, for example.

7.3 The net power accumulation in the core in 3D

In this section, the net accumulation of power in the core is measured for light propagation in 3D SIFs. A simplified version of this calculation was shown in Sec. 7.2 which revealed that diffusion artefacts restricted the use of the iterated power distributions to within a few number of reflections. Therefore, it is required to establish methods to estimate the net accumulation of power in the core, along the entire fibre length, while being faced with this limitation. This is done first for a toy model and for the special case of the non-concentric circular core and cladding SIF geometry that are not significantly affected by such artefacts, allowing the illustration of the proposed truncation procedure in a benign setting before application to more general problems.

The net transfer of flux to the core over the fibre's entire length can be written in terms of the function w defined in (7.3) as

$$\Phi_{3\mathrm{D}} = \int_0^\infty \langle w, f(z)\rangle dz, \tag{7.7}$$

where arguments $(s, \bar{p}_i)$ in densities are suppressed such as $f(s, \bar{p}_i, z)$ in this section. In the Laplace domain,

$$\Phi_{3\mathrm{D}} = \lim_{\beta\to 0}\langle w, \bar{f}(\beta)\rangle.$$

Since only a finite number of reflections can be performed by the finite operator, it is necessary to define

$$\bar{\Phi}^M_{3\mathrm{D}}(\beta) = \sum_{m=0}^{M}\langle w, \bar{f}_m(\beta)\rangle,$$

and

$$\Phi_{3D}^{M} = \sum_{m=0}^{M} \int_{0}^{\infty} \langle w, f_m(z) \rangle \dot{z} \tag{7.8}$$

$$= \bar{\Phi}_{3D}^{M}(\beta)\big|_{\beta=0} \tag{7.9}$$

$$= \Phi_{2D}^{M}. \tag{7.10}$$

The last line states that for finite M the definition of Φ_{2D}^{M} given in (7.4) is recovered in the limit $\beta \to 0$. However, the distinction between 2D and 3D versions must be maintained because

$$\lim_{\beta\to 0} \lim_{M\to\infty} \bar{\Phi}_{3D}^{M}(\beta) \neq \lim_{M\to\infty} \lim_{\beta\to 0} \bar{\Phi}_{3D}^{M}(\beta).$$

In other words

$$\Phi_{3D} \neq \Phi_{2D}. \tag{7.11}$$

In practical terms, the importance of the order of limits means that, if M is truncated to make allowance for diffusion artefacts. It must be ensured that β remains sufficiently large so that the truncation does not matter, but at the same time small enough to approximate (7.7) sufficiently well. Such considerations are first applied to the toy model discussed in the following subsection. In subsection 7.3.2, Φ_{3D} will be calculated for the SIF with circular core and cladding boundaries where light propagation suffers minimally from diffusion. Finally, in subsection 7.3.3, the calculation will be applied to the deformed SIF where diffusion is very prevalent in the phase space and M-truncation is required.

7.3.1 A toy model

Using a toy model, the relevance of the order of limits in (7.11), and the corresponding impact of truncating M are illustrated. The transfer operator of the toy model is by definition a finite matrix and there is no diffusion mechanism.

The model consists of a 2D waveguide, illustrated in Fig. 7.4. The SOSs here are zero-dimensional, so there are no $(s, \bar{p}_i)$ coordinates and the entire boundary of core or cladding

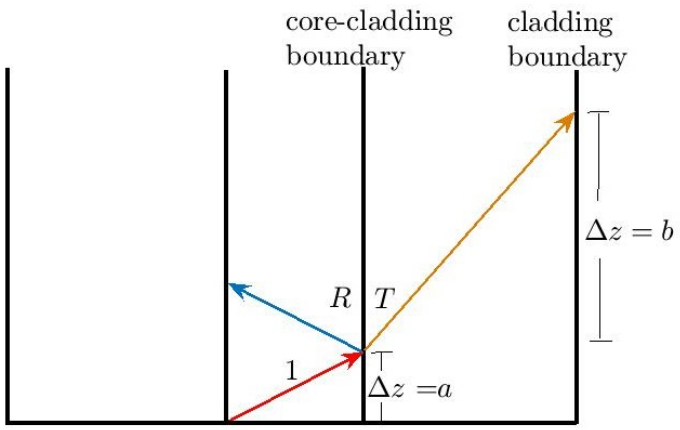


Figure 7.4: A toy model consisting of a 2D waveguide for z-propagation along the fibre.

is described by canonical coordinates (z, p_z). p_z is suppressed in the notations and, in addition, attention is given to densities that are symmetric about the middle axis of the waveguide so that the cross-sectional SOSs each consist of a single point. The transfer matrix reduces to the 3×3 matrix

$$\bar{T}_{3D}(\beta) \to \bar{T}_{\text{toy}}(\beta) = \begin{bmatrix} 0 & Re^{-\beta b} & Te^{-\beta b} \\ e^{-\beta b} & 0 & 0 \\ 0 & Te^{-\beta a} & Re^{-\beta a} \end{bmatrix}. \tag{7.12}$$

Here, T and R are respectively the reflectance and transmittance of a ray hitting the core-cladding boundary and $\Delta z = a$ and $\Delta z = b$ are the vertical displacements experienced of a ray traversing the core or the region between core and cladding. All of these would depend on p_z, but in all calculations performed, p_z is conserved and so they are effectively fixed for the rest of this discussion.

The net transfer of flux to the core is once again represented by (7.7) except that w is now a finite vector

$$w = \begin{bmatrix} 0 & T & -T \end{bmatrix}. \tag{7.13}$$

(The symbols such as Φ_{3D} and Φ_{2D} are reused here even though the underlying geometries are now respectively two-dimensional and one-dimensional.) Since there are no diffusion

artefacts in this model, the limit $M \to \infty$ may be passed directly, allowing the geometric sum to be written as

$$\Phi_{3\mathrm{D}} = \lim_{\beta \to 0} \langle w, \frac{1}{1 - \bar{T}_{\mathrm{toy}}(\beta)} \bar{f}_0 \rangle. \tag{7.14}$$

The gap between $\Phi_{3\mathrm{D}}$ and $\Phi_{2\mathrm{D}}$ in (7.11) is directly explained in this context by representing the right-hand side of (7.14) using a basis of eigenvectors of $\bar{T}_{\mathrm{toy}}(\beta)$. The gap is in particular determined by the leading eigenvector $\lambda_0(\beta)$, which has the limit

$$\lim_{\beta \to 0} \lambda_0(\beta) = 1. \tag{7.15}$$

It is noted that w is necessarily orthogonal to the corresponding eigenvector, denoted by $u_0(\beta)$, in this limit:

$$\lim_{\beta \to 0} \langle w, u_0(\beta) \rangle = 0. \tag{7.16}$$

Using l'Hôpital's rule, it is therefore found that the contribution of this leading eigenvector to (7.14) is of the form

$$\delta\Phi = \text{const.} \times \frac{\langle w, u_0'(0) \rangle}{\lambda_0'(0)},$$

where the primes indicate a derivative with respect to β, evaluated at $\beta = 0$. Note that in an analogous evaluation of the truncated sum $\Phi_{3\mathrm{D}}^M = \Phi_{2\mathrm{D}}^M$, there is no contribution from this leading eigenvector in the limit $\beta \to 0$, because of (7.16) (whereas all other eigenvectors contribute identically). Therefore this leading-eigenvector contribution is the origin on the gap

$$\Phi_{3\mathrm{D}} - \Phi_{2\mathrm{D}} = \delta\Phi$$

in (7.11) that arises from the exchange of limits $\beta \to 0$ and $M \to \infty$.

The ramifications of this gap will now be explored for calculations of the net transfer of flux when M is truncated. The concrete calculations are performed for the special case $\bar{f}_0 = [1, 0, 0]$, so that the initial distribution illuminates the cladding boundary only, and for $a = 0.2$, $b = 0.5$, $R = 0.7$ and $T = 0.3$. To reiterate, $\Phi_{3\mathrm{D}}$ denotes the plateau of $\bar{\Phi}_{3\mathrm{D}}^M$ reached when $M \to \infty$ first, before letting $\beta \to 0$. The limits taken the opposite way

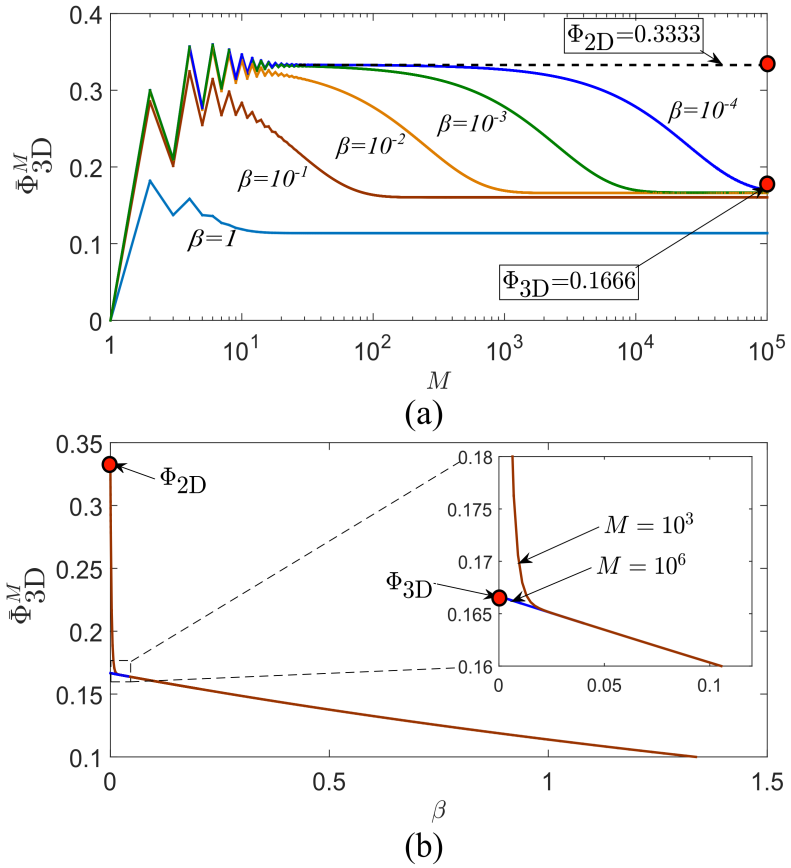


Figure 7.5: (a) Variation of Φ^M_{3D} with a finite M. Φ^M_{3D} converges to Φ_{3D} as β decreases, provided M is large enough. Otherwise it converges to Φ_{2D} as shown by the dashed line. (b) Variation of the converged Φ^M_{3D} with β where increasing M from 10^3 to 10^6 ensures convergence towards Φ_{3D} as $\beta \to 0$.

would result in $\bar{\Phi}^M_{3D}$ converging to Φ_{2D} instead. The procedure to obtain Φ_{3D} for finite M is shown in figure 7.5. Φ_{3D} in the toy model can be related to the distance traversed along the z-axis in the fibre and is equal to $a/(a+2b)$. This ratio is related to the width of the core medium compared to that of the cladding medium and is found by the Taylor series expansion of equation 7.14 after imposing the proper limits. However, $\Phi_{2D} = 1/3$ and results directly from the uniform leading eigenvector of $\bar{T}_{\text{toy}}$. Figure 7.5(a) shows the variation of Φ^M_{3D} for a finite but large M. $\bar{\Phi}^M_{3D}$ is calculated for ever decreasing β values while allowing M to be arbitrarily large as diffusion is not an issue here.

With $M = 10^5$, $\bar{\Phi}^M_{3D}$ converges to Φ_{3D} for $\beta = 10^{-1}, 10^{-2}$, and 10^{-3}. $\bar{\Phi}^M_{3D}$ does not converge to Φ_{3D} for too large β when $\beta = 1$, and on the other hand, for $\beta = 10^{-4}$ or less, M is required to be even larger to get to Φ_{3D}. Therefore, for a finite M, $\bar{\Phi}^M_{3D}$ would converge

towards Φ_{2D} instead of Φ_{3D} as β decreases as indicated by the dashed line. Figure 7.5(b) shows the variation of the converged $\bar{\Phi}_{3D}^{M}$ with the variation of β. As β decreases, the inset in figure 7.5(b) shows $\bar{\Phi}_{3D}^{M}$ rising up to Φ_{2D} and deviating from Φ_{3D} when M is not large enough. Increasing the order of M from 10^3 to 10^6 allows the proper convergence to occur to $\Phi_{3D} = 1/6$ instead.

7.3.2 Step index fibres with circular core and cladding boundaries

In this subsection, Φ_{3D} is obtained for light propagation in an SIF with circular core and circular cladding boundaries. The calculations here are carried forward for the example of the SIF with circular core and cladding discussed in subsection 7.2.1. In particular, $\Phi_{2D} = 0.1460$ was obtained as a plateau in figure 7.3(a) while discussing the effects of diffusion, and it was concluded that M could be made arbitrarily large as the SOSs of the circular SIF suffers minimally from diffusion. Owing to the pixelated SOSs, $\bar{T}_{3D}$ is a $3N^2 \times 3N^2$ matrix and quite a few of its leading eigenvalues in the complex plane are very close to the unit circle, including the maximum eigenvalue equal to one. This complicates the passing of the limit $M \to \infty$ directly and using equivalent expression like equation 7.6 as it becomes ill-conditioned even though diffusion is not significant here. Therefore, Φ_{3D} is calculated using the procedure laid out in the previous subsection for the toy-model allowing M to have finite values.

A similar result ensues and figure 7.6(a) shows $\bar{\Phi}_{3D}^{M}$ converging towards Φ_{3D} for $\beta = 10^{-1}$, 10^{-2}, 10^{-3}, and 10^{-4} when M is truncated at 10^5. Smaller β requires M to be set to a larger value, otherwise Φ_{3D}^{M} converges to Φ_{2D} as shown by the dashed line. Figure 7.6(b) shows the convergence of Φ_{3D}^{M} with different values of β. Increasing M allows Φ_{3D}^{M} to converge to Φ_{3D} as β decreases. As with the toy model, plots of $\Phi_{3D}(\beta)$ for fixed M appear to approach a value near $\Phi_{3D} = 0.0642$ as β decreases, but increase sharply towards $\Phi_{2D} = 0.1460$ for the very smallest values of β as the sum in equation 7.8 becomes sensitive to the truncation in M. The physical result is therefore calculated by extrapolating to

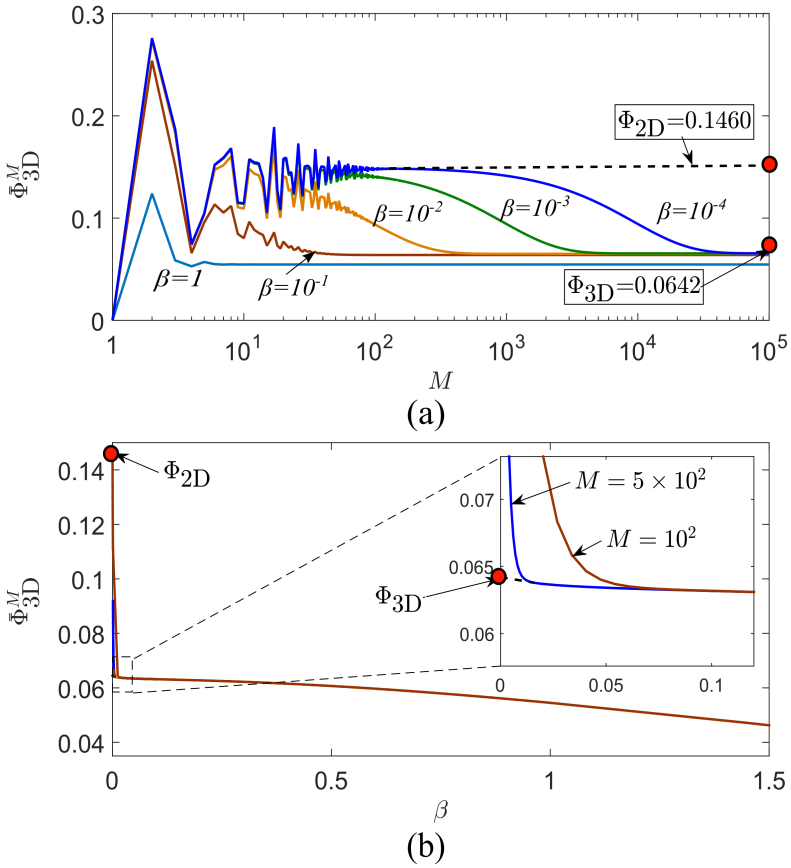


Figure 7.6: (a) $\bar{\Phi}^M_{3D}$ variation within a finite but large M in the SIF with circular core-cladding boundaries. (b) Variation in Φ^M_{3D} convergence as β is varied. Increasing M allows $\bar{\Phi}^M_{3D}$ to converge towards Φ_{3D} as $\beta \to 0$.

$\beta = 0$ from values of β that are large enough that equation 7.8 is insensitive to M.

7.3.3 Step index fibres with deformed core and cladding boundaries

Having established a procedure that enables, in problems without significant diffusion, to estimate Φ_{3D}, using moderate truncations in M, it is now applied to deformed SIFs, where diffusion is present. Plots of $\bar{\Phi}_{3D}(\beta)$, as a function of M for fixed β and as a function of β for fixed M, are shown in Fig. 7.7. This is the analogue of Figs. 7.5 and 7.6 for the deformed fibre geometry and initial condition illustrated in Fig. 7.2.

The main difference from previous calculations is that, because there is diffusion, there

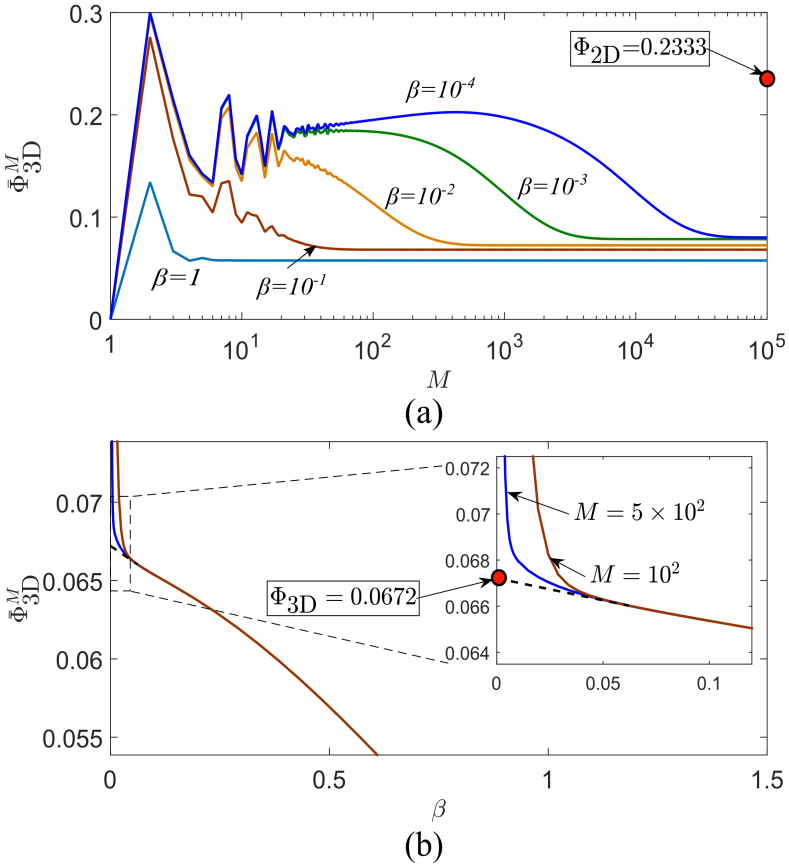


Figure 7.7: (a) Variation of Φ_{3D}^{M} with M. Diffusion creates upward slopping in the SOSs and requires M to be limited to a few hundreds of reflections. (b) Variation of Φ_{3D}^{M} with β, where M is limited to 5×10^2 as shown in the inset and Φ_{3D} is estimated using extrapolation as indicated by the dashed line.

is no clear asymptote to a fixed value Φ_{2D} as M increases for fixed values of β (see Fig. 7.7(a)). Instead $\bar{\Phi}_{3D}(\beta)$ continues to drift upwards as power diffuses out of the whispering gallery region of the cladding SOS and into the whispering gallery region of the core interior SOS. Nevertheless, the extrapolation procedure illustrated in Fig. 7.7(b) proceeds as in previous examples. M is fixed at values large enough that there is convergence to an effective steady state (as determined from Fig. 7.3, for example), but small enough that diffusion does not dominate. The value at $\beta = 0$ is extrapolated from values of β to that are moderately small but not so small that $\bar{\Phi}_{3D}(\beta)$ becomes sensitive to M. In the figure, the result is shown as an estimate $\Phi_{3D} = 0.0672$ for the power flux transferred to the core.

7.4 Chapter summary

A finite operator model has been used to model transport of power between core and cladding in optical step-index fibres. The model is based on a ray-tracing description of power transport and uses a coarse graining of phase space obtained by pixelating surfaces of section to reduce the problem to finite matrix calculations. By monitoring the transport of power flux across boundaries between core and cladding, the formalism can naturally be adapted to provide the net transfer of power between core and cladding, which is of prime interest in applications.

The method can in particular be applied to deformed geometries with chaotic ray dynamics and complex borders between trapped and mixing regions of phase space. In the general case, however, diffusion artefacts brought about by the coarse graining of phase space limit the accuracy of the simulation for a given pixel size. A procedure was established to extract physically realistic estimates of power transfer in the face of these limitations and this has been benchmarked using simpler geometries that are not diffusion dominated.

It is to be noted that, although applied to lossless, gainless models in this thesis, the

underlying formalism can be adapted to treat light propagation in fibres with gain and/or losses, and it offers a numerically robust basis in which to design optical fibres for amplifier and fibre sensing applications.

Chapter 8

Optimisation of step-index fibres for better power accumulation in the core.

8.1 Introduction

Having established the method to calculate the power accumulation in the core, Φ_{3D}, after propagation of arbitrary light distributions through deformed step-index fibres (SIFs), it is now possible to investigate how the calculation varies when the design of the fibre is changed. In addition to the fibre design, the input excitation is also varied to see the changes in Φ_{3D}.

In this chapter, the variation in the net accumulation of power in the core in the step-index fibres (SIFs) is investigated with the changes in the modelling parameters. The variations include, changing the position and the cross-sectional area of the core in the SIF, the refractive index contrast between core-cladding media, the input excitation, and the z-directional momentum component of the propagated light distribution, p_z. To see the changes in the net accumulation of power in the core as a result of such variations,

examples of SIFs with only circular core and cladding boundaries are chosen, so as to minimise the diffusion artefacts in the system.

8.2 Input excitations in the phase spaces

Two arbitrary light distributions in the SIF phase space are shown in figure 8.1. These excitations serve as the two extremes of the power distribution in the SIF, where, in figure 8.1(a), with I1, all the power is in the core initially, and in figure 8.1(b), with I2, there is no power initially in the core. With I1, power escapes partially from the core after propagation and the net power accumulation in the core, Φ_{3D}, represents the power that is remaining the core. After propagating I2, Φ_{3D} is the total transfer of power from the cladding medium to the core. Any other input distribution will be between the two such extremes. Note, that the propagation of I2 was shown in chapter 7 for SIFs with both circular and deformed core/cladding boundaries (see Fig. 7.1 and 7.2).

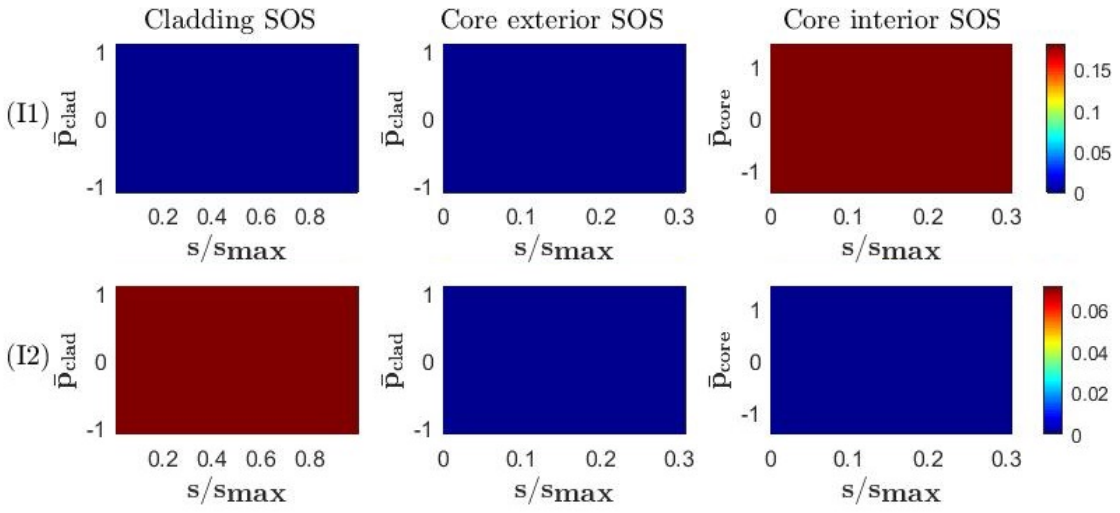


Figure 8.1: Initial arbitrary excitations in the phase space of SIFs. (a) An initial uniform excitation in the core interior SOS. (b) An initial uniform excitation in the cladding SOS. Any possible input excitation will be between these two extremes.

8.3 The net power accumulation in the core in the SIF

Having defined the two arbitrary input distributions in the previous section, the variation of power accumulation in the core with the design of SIFs, and with the variation in the propagated input distribution will now be discussed. In chapter 7, it was shown that the calculation of the power accumulated in the core can be done in both 2D and 3D settings. The 2D calculation was done only to investigate the effects of diffusion in the system. In this chapter, only SIFs with circular core and circular cladding boundaries will be investigated which are affected minimally from diffusion. This allows more flexibility with the modelling parameters and provides a dynamical system where the number of reflections carried out by the finite operator are not limited. Moreover, the variations investigated here also applies to SIFs with deformed boundaries. The discussion is started in the following subsection using the 2D setting, and the results are applied in the subsequent section for the full 3D analysis.

8.3.1 Calculations in 2D

As discussed in chapter 7, when $\bar{\Phi}^M_{\text{3D}}$ is calculated with $\beta = 0$, it converges to Φ_{2D}. An example of a circular core and cladding SIF was discussed in chapter 7 with core radius, $r_c = 0.2828$, and centred at $(0.1, 0.3)$ in a unit circular cladding, where the input excitation, I2, was propagated (see Fig. 7.1). Figure 7.3(a) showed the resulting Φ_{2D}, which is found to be invariant of any changes in the core/cladding refractive index contrast or changes in the z-component of the momentum of rays, p_z. However, when the input excitation is changed to I1 (see Fig. 8.1(a)), changes in the core/cladding dielectric properties affected the plateau value of Φ_{2D}. Figure 8.2(a) shows the changes in Φ_{2D} when the refractive index of the cladding is changed while keeping that of the core unchanged.

Since the total-internal reflection (TIR) region in the core, is within the range

$$n_{cl}\sqrt{1-p_z^2} \leq |\bar{p}_{\text{core}}| \leq n_c\sqrt{1-p_z^2}, \tag{8.1}$$

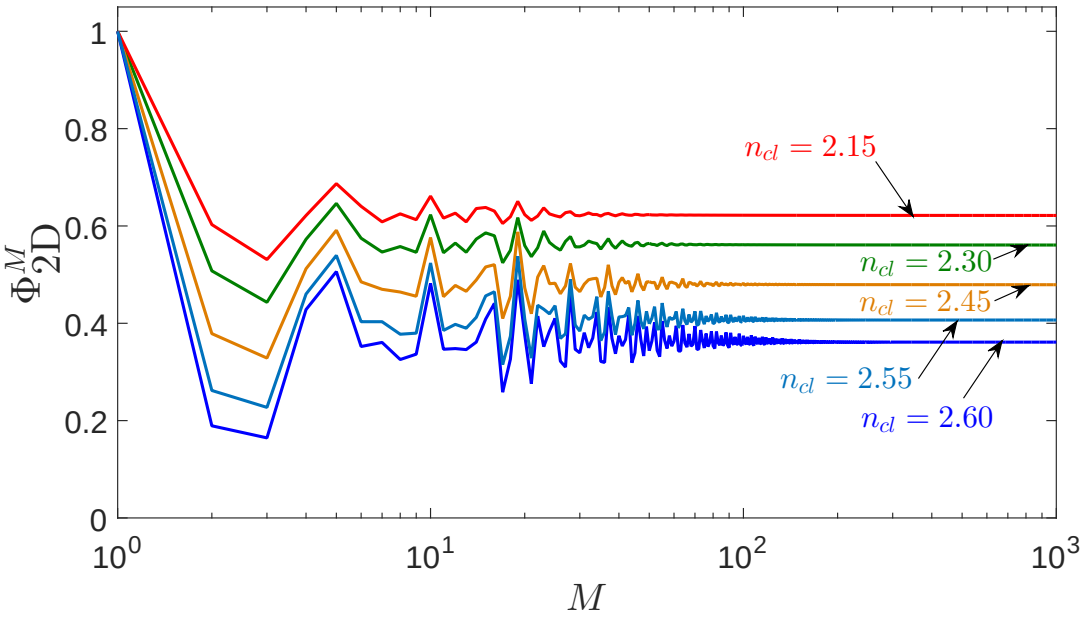
more power gets trapped in the TIR region in the core as n_{cl} decreases, and $Phi_{2\text{D}}$ plateau is seen to increase.

The properties of the dielectric boundary is also affected by p_z, which is the axial component of the momentum of rays in the fibre. Increasing p_z has the same effect on the calculated $\Phi_{2\text{D}}$, as shown in figure 8.2(b), although its effect is less prominent (because of the sq. root relation).

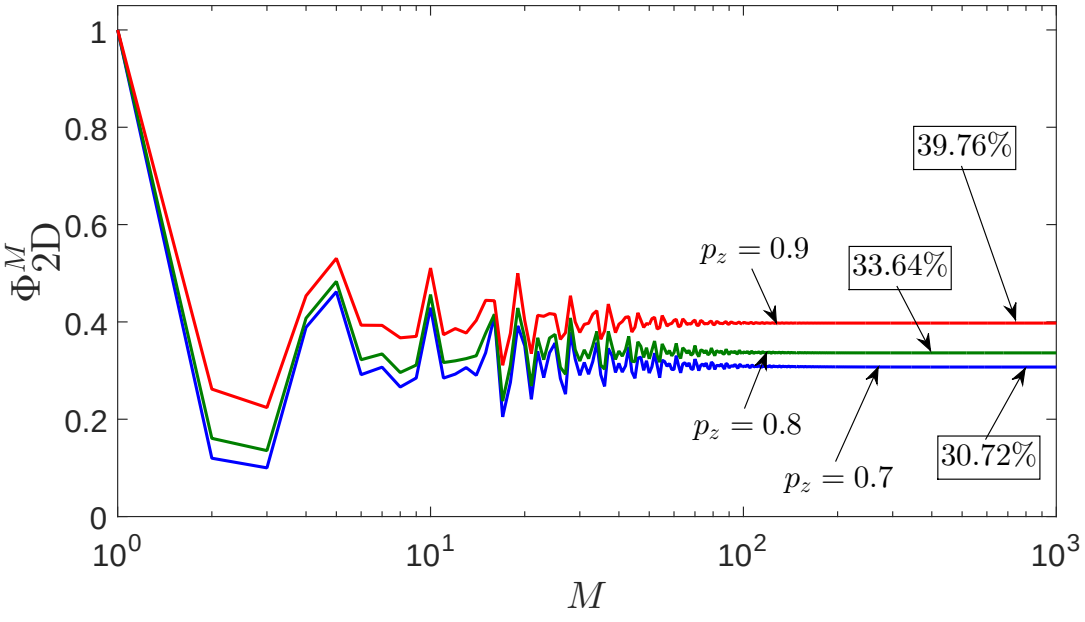
8.3.2 Calculations in 3D

The main objective is to obtain $\Phi_{3\text{D}}$ by propagating arbitrary input excitations in the SIF. The calculation of $\Phi_{2\text{D}}$ serves only as an indication of the diffusion effects (which is insignificant, in the case studied here), and shows the relative changes in the area of the TIR region of the core as n_{cl} and p_z are varied. Thus, $\Phi_{3\text{D}}$ is also calculated after propagating the input distributions, I1 and I2, and figure 8.3 shows the variation of $\bar{\Phi}_{3\text{D}}^{M}$ with β obtained after $M = 10^5$ iterations for each β. Here, $n_{cl} = 2.55$, and $p_z = 0.75$. It is calculated with a finite operator, $\bar{T}_{3D}$, after having the phase space pixelated with $N = N_e = N_i = 50$. The inset in figure 8.3 shows the deviation as $\bar{\Phi}_{3\text{D}}^{M}$ becomes sensitive to the finite value of M, as $\beta \to 0$.

Because of the deviation at $\beta \to 0$, special procedure was required to find $\Phi_{3\text{D}}$, as discussed in chapter 7. The cause of the deviation, as $\beta \to 0$ is also evident when the eigen-spectrum of the finite operator, $\bar{T}_{3D}$, is studied. Figure 8.4 shows the spectrum of the finite operator, $\bar{T}_{3D}$. The figure only shows the leading 20 eigenvalues of $\bar{T}_{3D}$ for non-zero β in the complex plane. All eigenvalues of the finite operator lie within the unit circle and, as the value of β decreases, the leading eigenvalues approach the unit circle. Figure 8.4(a) shows the eigenvalues of $\bar{T}_{3D}$ with $\beta = 1$, and the leading eigenvalue is $\lambda_{\text{max}} = 0.89$, as shown by



(a)



(b)

Figure 8.2: Variation in Φ_{2D} from input excitation I1 (see Fig. 8.1(a)), with the variation in the properties of the core-cladding dielectric boundary. (a) The TIR region of the core interior SOS expands when cladding refractive index decreases compared to that of the core, and more of the initial excitation gets trapped in the core during propagation. (b) The same trend is seen when the value of p_z of the input distribution is increased although the variation in the plateau is less prominent.

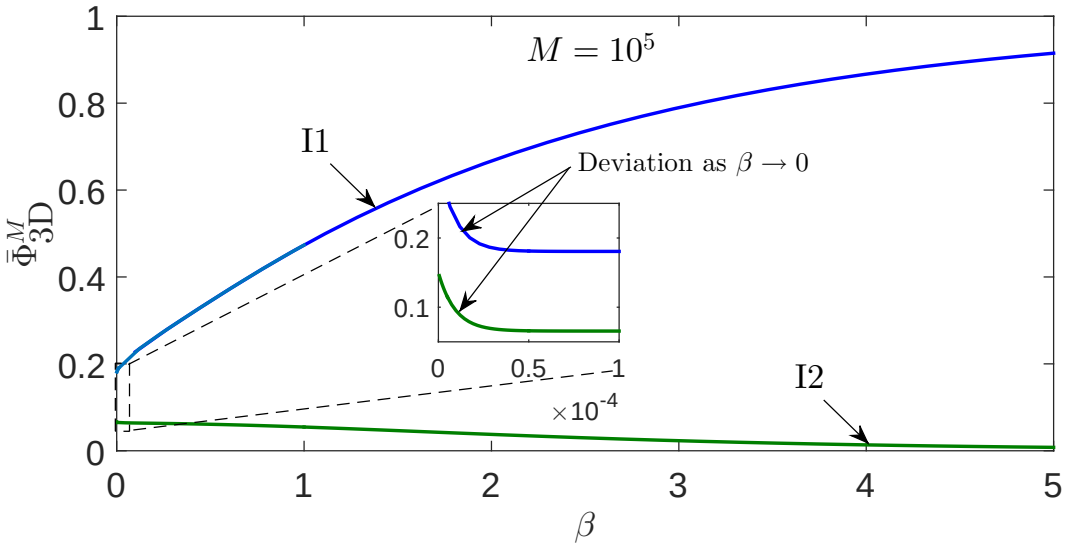
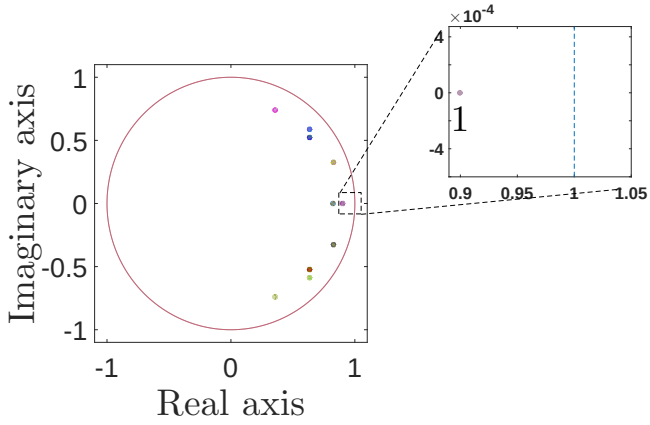


Figure 8.3: $\bar{\Phi}^M_{3D}$ variation with β, from initial excitations I1 and I2 (see Fig. 8.1). The circular boundaries of the core and cladding in the SIF allows M to be very large, and so here $M = 10^5$. The inset shows the sensitivity in $\bar{\Phi}^M_{3D}$ as β becomes small for having a finite M, and results in the deviation towards Φ_{2D} (Φ_{2D} is not shown in the inset).

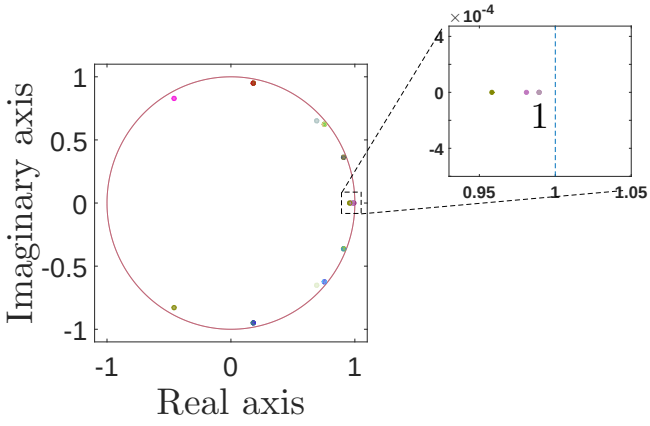
the inset. $\lambda_{\max}$, is well separated from the other eigenvalues in this case. In figure 8.4(b) the spectrum is shown with $\beta = 0.1$, and the inset shows three of the largest eigenvalues that have moved closer to the unit circle. In figure 8.4(c), with $\beta = 0.01$, the inset shows the leading eigenvalues coming very close to each other and with $\lambda_{\max}$ almost on the unit circle (here $\lambda_{\max} = 0.998$). The leading eigenvalue of $\bar{T}_{2D}$ is equal to one, and the figure suggests that as $\beta \to 0$, $\bar{T}_{3D}$ is essentially turned into $\bar{T}_{2D}$.

Variation of $\bar{\Phi}^M_{3D}$ with the pixel area

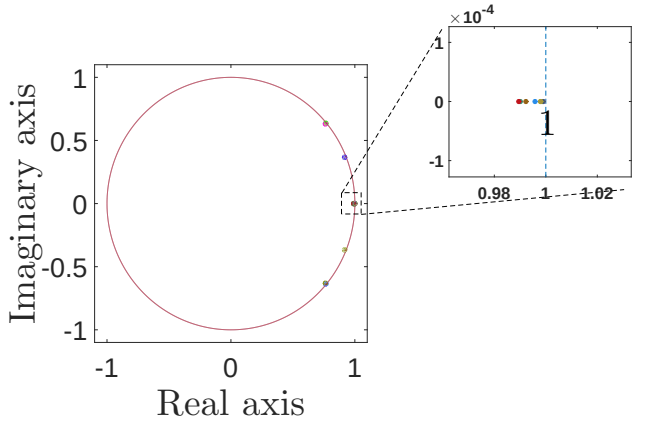
A finer pixelation allows a more accurate estimation of the captured core power after propagation. Figure 8.5 shows the calculation of the $\bar{\Phi}^M_{3D}$ with two different values of N. Figure 8.5(a) shows $\bar{\Phi}^M_{3D}$ calculated with $\beta = 0.04$, one curve for $N = 50$, and the other for $N = 1000$. Input distribution I2 was used, and the figure shows a small change in the plateau reached as a result of the change in pixelation. Figure 8.5(b) shows the variation of Φ^M_{3D} with β, plotted for each of the two values of N. The difference in the $\bar{\Phi}^M_{3D}$ between the two curves increases as the value of β decreases. The value of Φ_{3D} is estimated by the procedure described in chapter 7, and repeated here with the help of figure 8.5(c),



(a)



(b)



(c)

Figure 8.4: 20 leading eigenvalues of $\bar{T}_{3D}$, constructed for the SIF cross-section with circular core and cladding shown in figure 7.1(a), by pixelating the phase space with $N = N_e = N_i = 50$. In (a) $\beta = 1$, in (b) $\beta = 0.1$, and in (c) $\beta = 0.01$. As $\beta \to 0$ the leading eigenvalues of $\bar{T}_{3D}$ approaches the unit circle. The leading eigenvalue converging to unit causes the deviation in the calculated $\bar{\Phi}_{3D}$ as $\beta \to 0$.

when $N = 1000$. As β becomes smaller, the finite M causes the curve of $\bar{\Phi}_{3D}^{M}$ to deviate up towards Φ_{2D}. Increasing M causes this deviation to occur at smaller values of β, as shown by the curve with $M = 2 \times 10^4$, in comparison to the one with $M = 10^3$. The value of Φ_{3D} at $\beta = 0$ is obtained by extrapolation of the curve as shown by the dashed line and is equal to 6.464%.

Variation of $\bar{\Phi}_{3D}^{M}$ with refractive index contrast

Variation in the net power accumulation in the core, $\bar{\Phi}_{3D}^{M}$, is now investigated with the variation in the cladding refractive index. The excitation from the core interior SOS, I1 (see Fig. 8.1(a)), is used. Figure 8.6 shows the results, with $N = 50$, $p_z = 0.75$, and $n_c = 2.70$. Figure 8.6(a) shows $\bar{\Phi}_{3D}^{M}$ calculated with $\beta = 10^{-4}$, and varying n_{cl}. Compared to figure 8.2(a), the plots fall down and converge to Φ_{3D}, instead of Φ_{2D}, when non-zero values of β are used. $\bar{\Phi}_{3D}^{M}$ variation with β is also plotted in figure 8.6(b) where decreasing n_{cl} results in a larger Φ_{3D} at $\beta = 0$.

Variation of $\bar{\Phi}_{3D}$ with p_z

Next, p_z is varied while keeping other modelling parameters unchanged. Figure 8.7(a) shows the variation of $\bar{\Phi}_{3D}^{M}$ with the M for upto 10^5 reflections, with $\beta = 10^{-4}$. The dashed lines show the Φ_{2D} plateau that would have been reached if β was set to zero. With a non-zero value of β, the $\bar{\Phi}_{3D}^{M}$ converges to Φ_{3D} instead. Figure 8.7(b) shows the variation of $\bar{\Phi}_{3D}^{M}$ with β, where increasing p_z increases the TIR region of the core and allows the core to trap more power from the initial excitation.

8.3.3 Dependence on the cross-sectional area of the core

In this subsection, the variation in $\bar{\Phi}_{3D}^{M}$ is investigated with the variation in cross-sectional area of the core. The SIF boundaries investigated remain circular as before. In order to scatter more regular trajectories from the cladding SOS, the core is now placed very close

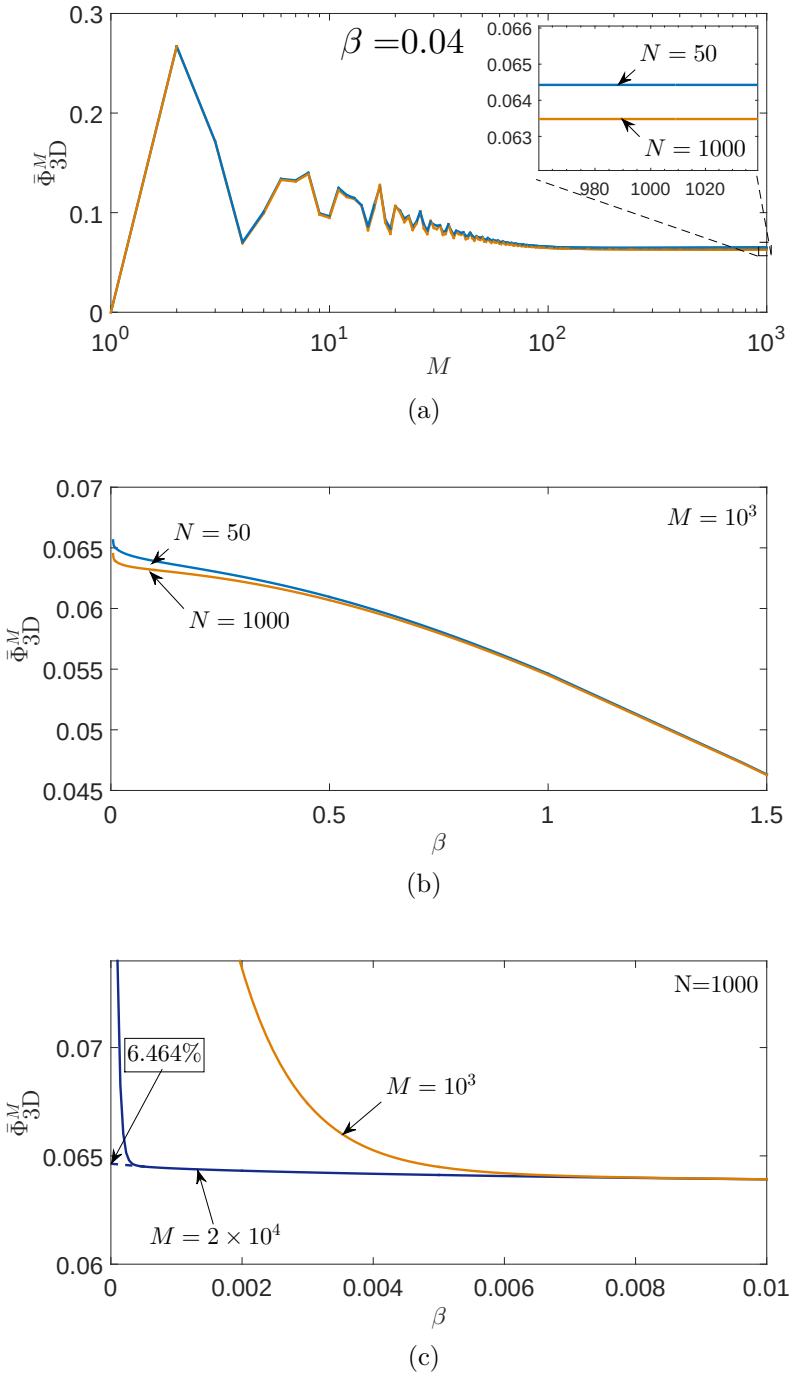
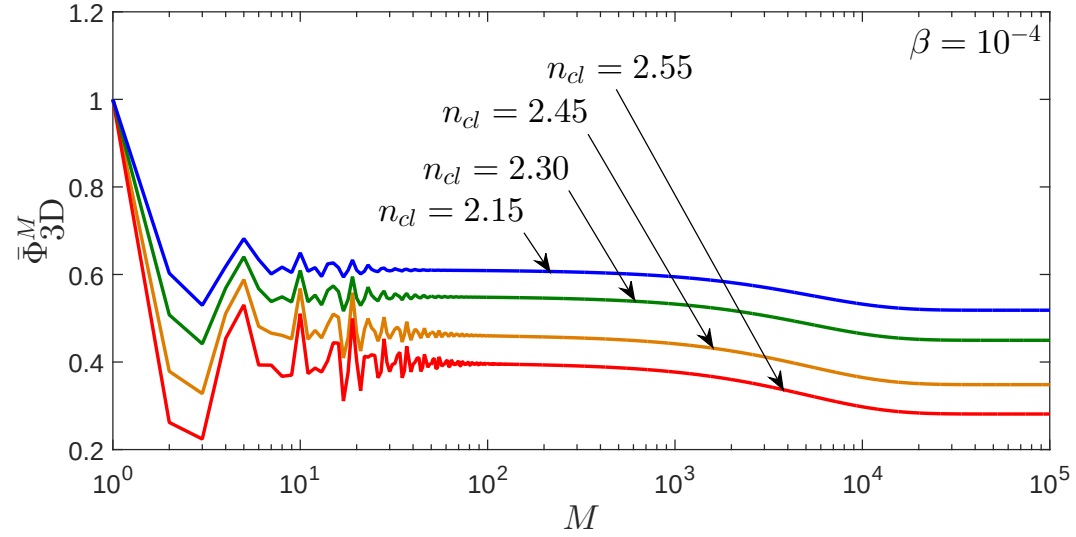
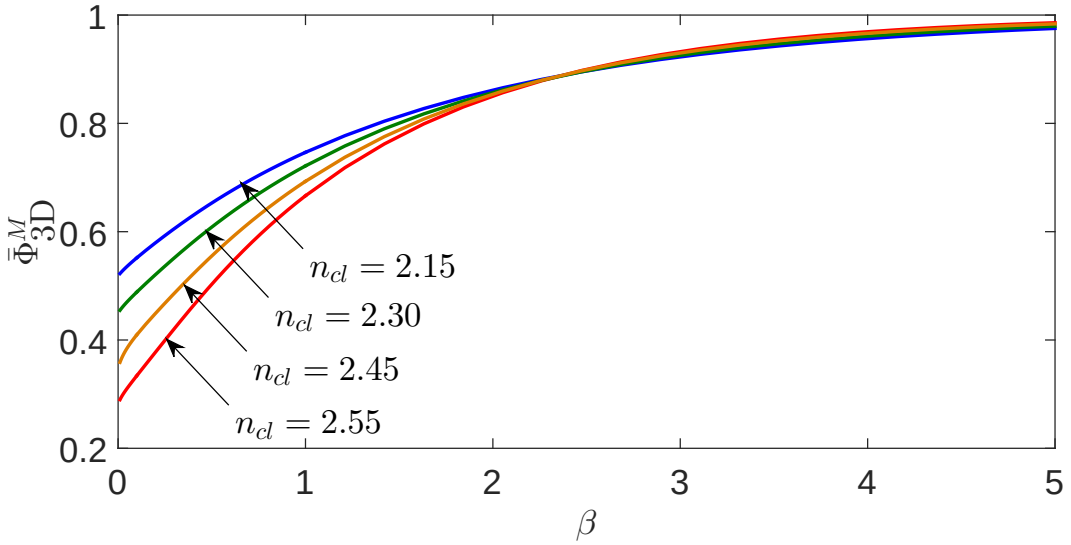


Figure 8.5: $\bar{\Phi}^M_{3D}$ variation in the SIF with circular core and cladding boundaries (see Fig. 7.1) with phase space pixelation. Here $n_{cl} = 2.55$, $n_c = 2.70$, $p_z = 0.75$, and the input excitation is I2 (see Fig. 8.1(b)). (a) $\bar{\Phi}^M_{3D}$ is calculated with a particular non-zero β ($\beta = 0.04$), where the converged value, at the end of $M = 10^3$ reflections, is slightly different for different N (lower for $N = 1000$, than that for $N = 50$). This variation is due to diffusion that exists minimally in the system. (b) Variation of $\bar{\Phi}^M_{3D}$ with the variation of β, showing the difference between the systems with two different pixlation increasing as *beta* decreases. (c) Φ_{3D} is calculated with the system with finer pixelation (with $N = 1000$), and for larger M, the deviation in $\bar{\Phi}^M_{3D}$ occurs for lower β ($\bar{\Phi}^M_{3D}$ deviating at $\beta \sim 0.06$ for $M = 10^3$, whereas it deviates at $\beta \sim 0.0005$ for $M = 2 \times 10^4$). Φ_{3D} is estimated by extrapolated dashed line.

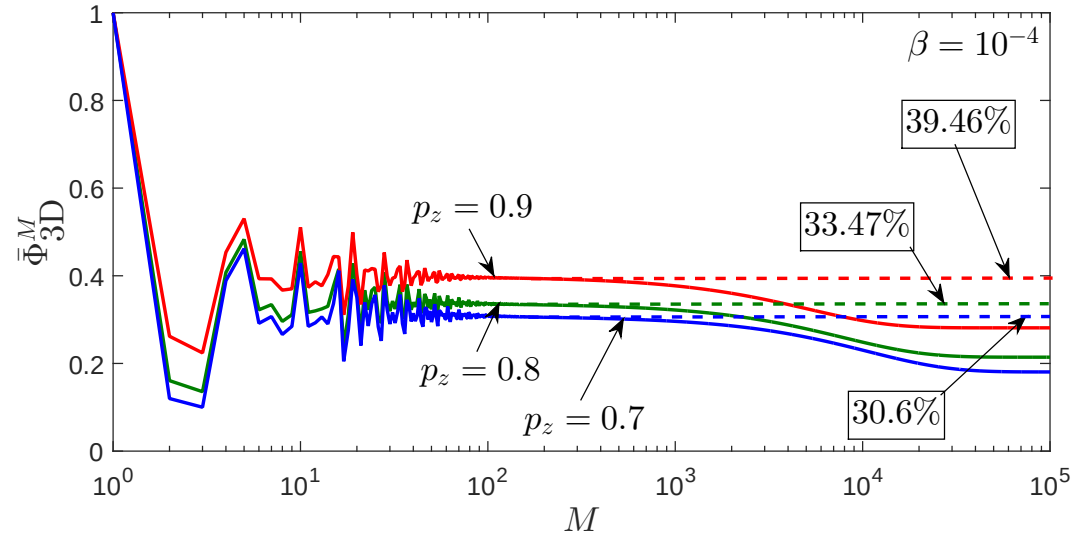


(a)

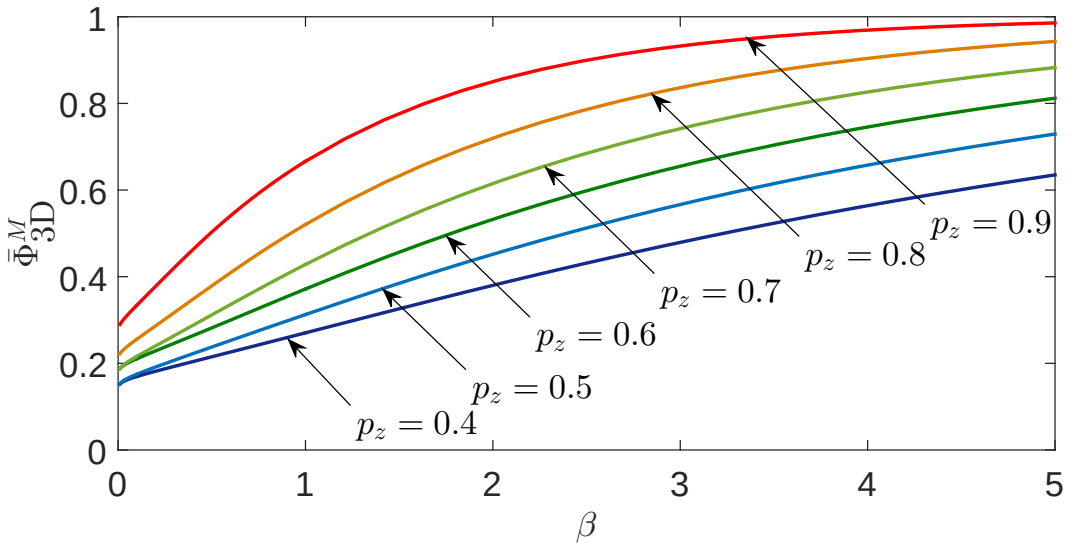


(b)

Figure 8.6: $\bar{\Phi}^M_{3D}$ evaluated for $\beta \neq 0$ when the fibre is excited with I1, and allowing the refractive index of the cladding, n_{cl}, to vary. (a) Variation in $\bar{\Phi}^M_{3D}$ for different values of n_{cl}, and $\beta = 10^{-4}$ (see Fig. 8.2(a) for the same plot, but with $\beta = 0$ instead). With decreasing n_{cl} the plateau of $\bar{\Phi}^M_{3D}$ increases. In (b) the variation of $\bar{\Phi}^M_{3D}$ is shown with the variation in β, where Φ_{3D} at $\beta = 0$ increases as n_{cl} decreases. A decrease in n_{cl} increases the area of the TIR region of the core and more power remains trapped in that region.



(a)



(b)

Figure 8.7: The variation in $\bar{\Phi}^M_{3D}$ with p_z. (a) $\bar{\Phi}^M_{3D}$ is evaluated for different values of p_z, with $\beta = 10^{-4}$ (see Fig. 8.2(b) for the same plot, but with $\beta = 0$ instead), when the fibre is excited with I1. (b) The variation of $\bar{\Phi}^M_{3D}$ with β is plotted for different p_z. As p_z increases the area of the TIR region of the core phase space increases and more power is trapped in the core.

to the cladding boundary in the SIF. The cross-sectional area of the core is varied and the core boundary is placed 0.05 units away from the cladding boundary as shown by figure 8.8(a). The cladding boundary is a unit circle, and the centre of the circular core is varied with the help of X_c along the x-axis, where $X_c = 1 - 0.05 - r_c$. Figure 8.8(a) shows three examples of non-concentric fibre cross-sections where the core radius is varied; $r_c = 0.3$ in (1), $r_c = 0.6$ in (2), and $r_c = 0.8$ in (3), and X_c changes accordingly. Figure 8.8(b) shows the resulting $\bar{\Phi}^M_{3D}$ calculated with a non-zero β ($\beta = 0.1$), from an excitation I2 (see Fig. 8.1). Since the excitation only enters the chaotic region of the core interior SOS, figure 8.8(b) shows $\bar{\Phi}^M_{3D}$ converging, in each case, to a value comparable to the cross-sectional area of the core. The difference is because of the TIR region in the core interior SOS that remains empty for any excitation from the cladding coming into the core. In addition to that, a thin layer of regular region in the cladding SOS remains as a result of whispering galleries that remain un-scattered by the core (the gap of 0.05 units between the core and the cladding boundary allows for this to happen; see Fig. 7.1). If the fibre allowed the propagated light distribution to be completely chaotic, then Φ_{3D} would converge to the cross-sectional area of the core. The converged value of $\bar{\Phi}^M_{3D}$ is taken in the limit $\beta \to 0$. Figure 8.8(c) shows the variation of $\bar{\Phi}^M_{3D}$ with β. It shows Φ_{3D} at $\beta = 0$ increasing according to the area of the core, indicating more power being accumulated in the larger core cross-section for a given propagation.

Figure 8.9 shows the variation of $\bar{\Phi}^M_{3D}$ in the limit $\beta \to 0$, for the changes in the modelling parameters, such as p_z, n_{cl}, and the cross-sectional area of the core. It shows the variations when the input excitation I2 is used, and summarises the analyses in this chapter. Figure 8.9(a) shows the variation of $\bar{\Phi}^M_{3D}$ with the core size as was investigated in this subsection, but with excitation I2 instead of I1. As the core cross-sectional area increases, the accumulated power in the core increases and an approximately linear relationship is observed. Next, the refractive index contrast between the core and the cladding is varied by changing n_{cl}, and it results in a decrease in Φ_{3D} as n_{cl} decreases when I2 is propagated, and is shown in figure 8.9(b). The area of the core is kept at 8% of the total cross-sectional area of the fibre. Next, the variation of $\bar{\Phi}^M_{3D}$ is observed by changing the position of the

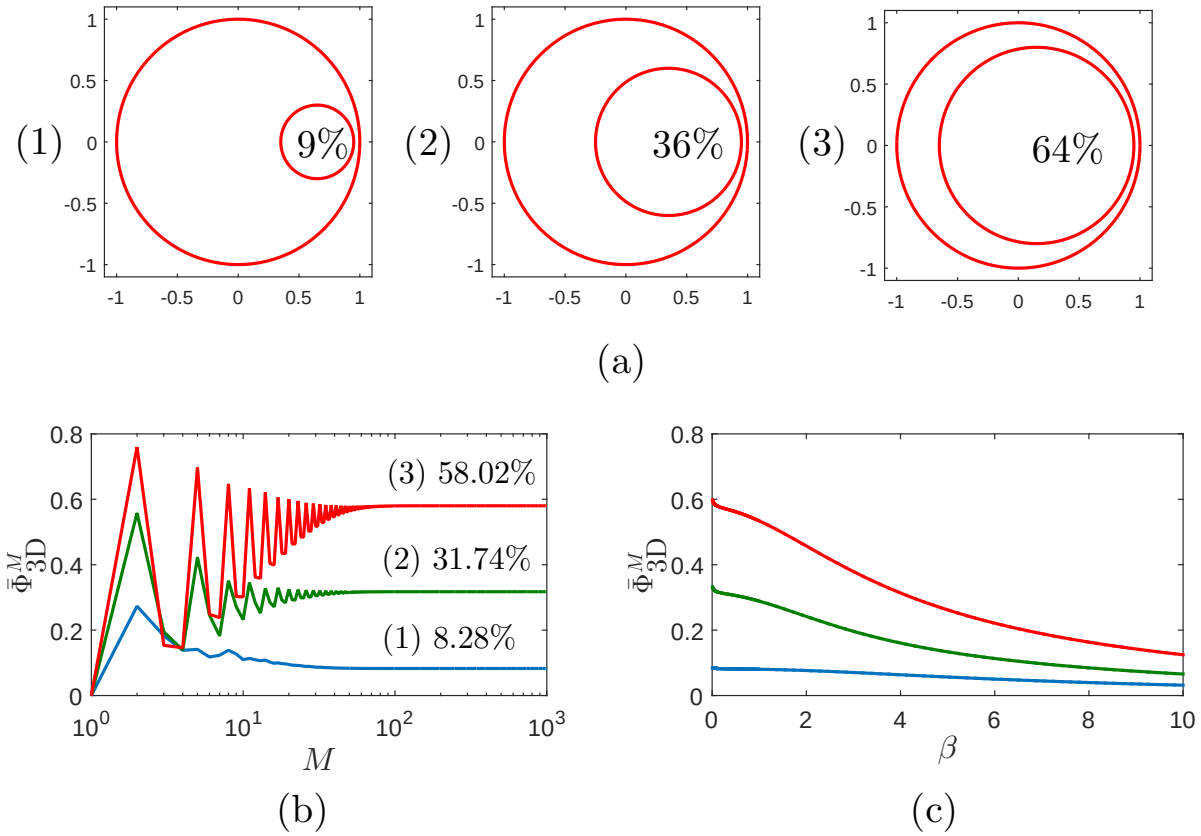


Figure 8.8: Variation in $\bar{\Phi}^M_{3D}$ with the cross-sectional area of the core. (a) The increase in core size relative to the fibre cross-section, where three cases are shown (9%, 36%, and 64%) (b) Variation in $\bar{\Phi}^M_{3D}$ with the cross-sectional area of the core, calculated with $\beta = 0.1$, and initial excitation I2 (see Fig. 8.1(b)). (c) $\bar{\Phi}^M_{3D}$ variation with β; Φ_{3D} at $\beta = 0$ are comparable to the area of the core in each case (8.28%, 31.74%, and 58.02% respectively).

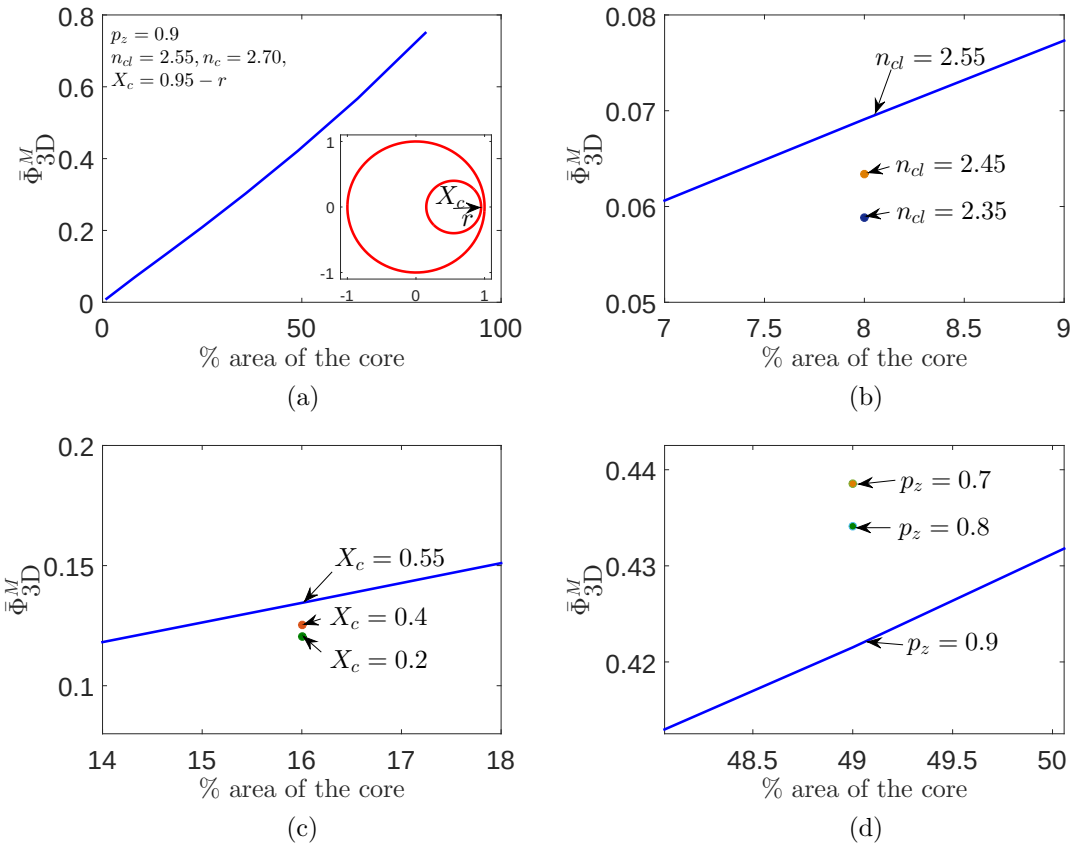


Figure 8.9: (a) Variation in Φ_{3D} with the cross-sectional area of the core. Φ_{3D} increases almost linearly with the core area. (b) With excitation I2, and increasing the refractive index of the cladding, n_{cl}, a decrease in Φ_{3D} is observed. (c) Moving the core closer to the cladding boundary, as X_c increases, the chaotic region expands and more power is accumulated in the core. (d) Increasing p_z has the same effect on Φ_{3D} as decreasing n_{cl}.

core. The cross-sectional area core in this case is kept at 16%, which is arbitrary. Figure 8.9(c), shows that, as the X_c increases, the origin of the core is moved closer to the boundary of the cladding. More rays are scattered by the core as a result and the area of the chaotic region increases. This results in more power being accumulated through the chaotic region in the core. Finally, figure 8.9(d) shows the variation in $\bar{\Phi}^M_{3D}$ with p_z, where an increase in p_z results in less power being accumulated by the core. This is due to the expansion of the TIR region of the core and shows the same effect as decreasing n_{cl}, although the change is less prominent because $\bar{p}_{\text{core}}$ has a square-root relationship with p_z.

8.4 Chapter summary

In this chapter, the finite operator model was applied to circular SIFs and variations in the power accumulated in the core, $\bar{\Phi}_{3D}^{M}$, was investigated by varying the modelling parameters. For a given SIF structure, the refractive index of the cladding medium was varied while that of the core medium remaining unchanged, to see the variation in the calculated Φ_{3D}. Also for the same SIF structure, different light excitations were propagated through the fibre, such as I1 and I2 as shown in figure 8.1, to see the variation in $\bar{\Phi}_{3D}^{M}$. $\bar{\Phi}_{3D}^{M}$ variation was also investigated with the variation in the momentum component of the rays along the fibre axis, p_z. In addition, the variation of $\bar{\Phi}_{3D}^{M}$ was also observed by varying the cross-sectional area of the core, and the position of core in the cladding medium. The analysis indicate that the area of the regular regions in the phase spaces of the SIF can be altered by the fibre design, and the excitation at the input can also be varied, to optimise the power accumulation in the core.

In the investigations carried out in this chapter, only circular-boundary-SIFs were chosen. So diffusion artefacts had minimal effect in light propagation, and there was isolation maintained between the chaotic and regular regions that was not affected by the number of reflections carried out. This allowed M to be set to large numbers, which is not possible for SIFs with deformed boundaries. However, for deformed SIFs, the variations in $\bar{\Phi}_{3D}^{M}$ with the design parameters of the fibre still applies.

Chapter 9

Conclusions and suggestions for future work

9.1 Summary of thesis achievements

A finite operator model has been proposed in this thesis to propagate light in deformed optical fibres. The model incorporates ray-dynamical systems which were investigated using the surfaces of section method. A method to extend and discretise mixed phase spaces in any SIF was developed to account for rays bouncing around in different core-cladding boundaries and different propagating media. Using the finite operator method, the power accumulated in the core was obtained after light propagation in an infinite length of the fibre in SIFs with both circular and deformed boundaries. It was found that the diffusion artefacts due to the discretisation of the phase space imposed an upper limit on the number of reflections that could be performed on any given light distribution in deformed SIFs. The diffusion artefacts were a direct consequence of the leading eigenvector of the finite operator, and it made an offset in the total accumulated power calculations. So the calculations were made by eliminating the contributions of the leading eigenvector from the overall modelled light propagation. The results were benchmarked using well-understood equivalent dynamical systems where diffusion artefacts weren't an

issue.

9.2 Applications

The finite operator model was developed here to help design fibre lasers, sensors and amplifiers operating in the MIR frequencies, as discussed in chapter 2. In chapter 7, results indicate that even with passive media simply applying slight deformations in the fibre resulted in a better accumulation of power in the core in optical step-index fibres, owing to the chaotic dynamics uniformly distributing the power in the fibre. The chaotic propagation can be smoothly controlled using the boundary deformations.

SIFs, with asymmetric cross-sections but longitudinally invariant structures, having mixed phases were studied in this thesis. Experiments can be designed where the propagation of light launched from the input end of the fibre can be controlled using the numerical aperture (NA), similar to those carried out by Mortensen [88] and based on modelling results by Doya [3] in addition to Kouznetsov *et al* [53, 54]. NA is controlled by the parameter p_z in the finite operator method. Depending on its value, rays will propagate either chaotically or periodically and this can be verified by looking at the intensity profile captured at the output end. The measurement of the power captured in the core will prove whether the chaotic propagation will improve the pump power efficiency in active deformed air-clad step-index fibres and double-clad fibres.

The finite operator model can also be used to calculate the length of propagation of light along the fibre. In experiments involving photoluminescence (PL) emissions from RE-ions doped in fibre, such measurements can facilitate the modelling of "settling down" distances. In the finite operator method, the measurement of the steady state distribution is made in terms of the number of reflections it takes for the phase space transients to settle down, and therefore, parameters such as p_z, and distances traversed along the direction of propagation, Δz after each reflection can be used to obtain the distances propagated by the emitted light distribution along the fibre.

In addition, the method can also be used to model active fibres. Selective gain can be introduced in the propagating media to model the amplification of the propagating trajectories. This will help design RE-ion doped fibre lasers by optimising pump power absorption in the core. The model incorporates uniformly distributed chaotic trajectories, and structural deformations in the fibre can be deliberately imposed to improve the pump power absorption. Investigation of active fibres is left for future work but is outlined briefly in the following section.

9.3 Future work with active optical fibres

The finite operator model developed here provides a template for modelling SIFs with gain. Amplification of the light propagating in the core medium could be applied, and the model could be used to study the effects of changing the fibre deformation, complex refractive indices (also representing loss and/or gain), and input light distribution on the propagated distribution. Figure 9.1 shows the core interior SOS of a deformed SIF where the light distribution in the elliptical core is amplified as it propagates along the fibre. The example used here is of the deformed SIF cross-section shown in figure 7.2, but with the refractive index of the cladding set to 1.8 (although the fibre is impractical to fabricate, the TIR region of the core is exaggerated as a result and the example serves to illustrate where the gain takes place most predominantly).

The propagated light distribution having the longest path through the total internal reflection (TIR) region in the core experiences the largest gain. In other words, a narrow band of trajectories having the lowest momenta inside the TIR region is amplified and the leading eigenvector of the finite operator, $\bar{T}_{3D}$ reflects this phenomenon as illustrated in figure 9.1. Therefore, the finite operator model offers a numerically robust method to model optical fibre amplification and could potentially be used to design optimised fibre sensors and amplifiers.

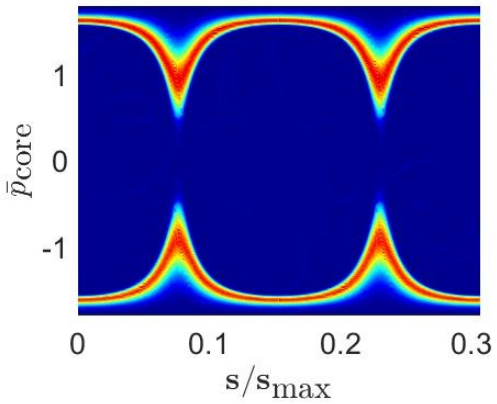


Figure 9.1: Introducing a gain medium in the core boundary causes amplification of a whispering gallery band in core interior SOS.

References

[1] A. B. Seddon, "A prospective for new mid-infrared medical endoscopy using chalcogenide glasses," *International Journal of Applied Glass Science*, vol. 2, no. 3, pp. 177–191, 2011. [Online]. Available: http://dx.doi.org/10.1111/j.2041-1294.2011.00059.x

[2] H. Poincare, "New methods of celestial mechanics," *Transl. NASA, Washington DC*, vol. 3, 1967.

[3] V. Doya, O. Legrand, F. Mortessagne, and C. Miniatura, "Speckle statistics in a chaotic multimode fiber," *Phys. Rev. E*, vol. 65, p. 056223, May 2002. [Online]. Available: https://link.aps.org/doi/10.1103/PhysRevE.65.056223

[4] A. Zakery and S. Elliott, "Optical properties and applications of chalcogenide glasses: a review," *Journal of Non-Crystalline Solids*, vol. 330, no. 1, pp. 1 – 12, 2003. [Online]. Available: http://www.sciencedirect.com/science/article/pii/S0022309303006379

[5] S. Hocdé, C. Boussard-Plédel, G. Fonteneau, and J. Lucas, "Chalcogens based glasses for IR fiber chemical sensors," *Solid State Sciences*, vol. 3, no. 3, pp. 279 – 284, 2001. [Online]. Available: http://www.sciencedirect.com/science/article/pii/S1293255800011353

[6] A. J. Kreisler and A. Gaugue, "Recent progress in high-temperature superconductor bolometric detectors: from the mid-infrared to the far-infrared (THz) range," *Superconductor Science and Technology*, vol. 13, no. 8, p. 1235, 2000. [Online]. Available: http://stacks.iop.org/0953-2048/13/i=8/a=321

[7] J. S. Sanghera, V. Q. Nguyen, P. C. Pureza, R. E. Miklos, F. H. Kung, and I. D. Aggarwal, "Fabrication of long lengths of low-loss IR transmitting $As_{40}S_{(60-x)}Se_x$ glass fibers," *Journal of Lightwave Technology*, vol. 14, no. 5, pp. 743–748, 1996.

[8] J. S. Sanghera, L. B. Shaw, L. E. Busse, V. Q. Nguyen, P. C. Pureza, B. C. Cole, B. B. Harrison, I. D. Aggarwal, R. Mossadegh, F. Kung, D. Talley, D. Roselle, and R. Miklos, "Development and infrared applications of chalcogenide glass optical fibers," *Fiber and Integrated Optics*, vol. 19, no. 3, pp. 251–274, 2000. [Online]. Available: http://dx.doi.org/10.1080/01468030050058811

[9] J. S. Sanghera, L. B. Shaw, and I. D. Aggarwal, "Chalcogenide Glass-Fiber-Based Mid-IR Sources and Applications," *IEEE Journal of Selected Topics in Quantum Electronics*, vol. 15, no. 1, pp. 114–119, 2009.

[10] H.-Y. N. Holman, M. C. Martin, and W. R. McKinney, "Tracking chemical changes in a live cell: Biomedical applications of SR-FTIR spectroscopy," *Spectroscopy*, vol. 17, no. 2, pp. 139–159, 2003. [Online]. Available: http://content.iospress.com/articles/spectroscopy/spe136

[11] G. R. Lloyd and N. Stone, "Method for identification of spectral targets in discrete frequency infrared spectroscopy for clinical diagnostics," *Applied Spectroscopy*, vol. 69, no. 9, pp. 1066–1073, 2015. [Online]. Available: https://doi.org/10.1366/14-07677

[12] C. R. Petersen, N. Prtljaga, M. Farries, J. Ward, B. Napier, G. R. Lloyd, J. Nallala, N. Stone, and O. Bang, "Mid-infrared multispectral tissue imaging using a chalcogenide fiber supercontinuum source," *Opt. Lett.*, vol. 43, no. 5, pp. 999–1002, Mar 2018. [Online]. Available: http://ol.osa.org/abstract.cfm?URI=ol-43-5-999

[13] Z. Tang, V. S. Shiryaev, D. Furniss, L. Sojka, S. Sujecki, T. M. Benson, A. B. Seddon, and M. F. Churbanov, "Low loss Ge-As-Se chalcogenide glass fiber, fabricated using extruded preform, for mid-infrared photonics," *Opt.*

Mater. Express, vol. 5, no. 8, pp. 1722–1737, 2015. [Online]. Available: http://www.osapublishing.org/ome/abstract.cfm?URI=ome-5-8-1722

[14] Z. Tang, D. Furniss, M. Fay, H. Sakr, L. Sójka, N. Neate, N. Weston, S. Sujecki, T. M. Benson, and A. B. Seddon, "Mid-infrared photoluminescence in small-core fiber of praseodymium-ion doped selenide-based chalcogenide glass," *Optical Materials Express*, vol. 5, no. 4, pp. 870–886, 2015.

[15] H. Sakr, D. Furniss, Z. Tang, L. Sojka, N. A. Moneim, E. Barney, S. Sujecki, T. M. Benson, and A. B. Seddon, "Superior photoluminescence (PL) of Pr^{3+}-In, compared to Pr^{3+}-Ga, selenide-chalcogenide bulk glasses and PL of optically-clad fiber," *Opt. Express*, vol. 22, no. 18, pp. 21 236–21 252, Sep 2014. [Online]. Available: http://www.opticsexpress.org/abstract.cfm?URI=oe-22-18-21236

[16] B. J. Eggleton, "Chalcogenide photonics: fabrication, devices and applications Introduction," *Optics Express*, vol. 18, no. 25, p. 26632, 2010. [Online]. Available: https://www.osapublishing.org/oe/abstract.cfm?uri=oe-18-25-26632

[17] H. G. Dantanarayana, N. Abdel-Moneim, Z. Tang, L. Sojka, S. Sujecki, D. Furniss, A. B. Seddon, I. Kubat, O. Bang, and T. M. Benson, "Refractive index dispersion of chalcogenide glasses for ultra-high numerical-aperture fiber for mid-infrared supercontinuum generation," *Opt. Mater. Express*, vol. 4, no. 7, pp. 1444–1455, Jul 2014. [Online]. Available: http://www.osapublishing.org/ome/abstract.cfm?URI=ome-4-7-1444

[18] C. R. Petersen, U. Møller, I. Kubat, B. Zhou, S. Dupont, J. Ramsay, T. Benson, S. Sujecki, N. Abdel-Moneim, Z. Tang, D. Furniss, A. Seddon, and O. Bang, "Mid-infrared supercontinuum covering the $1.4 - 13.3\mu$m molecular fingerprint region using ultra-high NA chalcogenide step-index fibre," *Nature Photonics*, vol. 8, no. 11, pp. 830–834, 2014. [Online]. Available: http://www.nature.com/doifinder/10.1038/nphoton.2014.213

[19] R. R. Gattass, L. B. Shaw, V. Nguyen, P. Pureza, I. D. Aggarwal, and J. S. Sanghera, "All-fiber chalcogenide-based mid-infrared supercontinuum source," *Optical Fiber Technology*, vol. 18, no. 5, pp. 345 – 348, 2012, fiber Supercontinuum sources and their applications. [Online]. Available: http://www.sciencedirect.com/science/article/pii/S1068520012000727

[20] G. Steinmeyer and J. S. Skibina, "Supercontinua: Entering the mid-infrared," *Nat Photon*, vol. 8, no. 11, pp. 814–815, 2014. [Online]. Available: http://dx.doi.org/10.1038/nphoton.2014.254 http://10.0.4.14/nphoton.2014.254

[21] U. Møller, Y. Yu, I. Kubat, C. R. Petersen, X. Gai, L. Brilland, D. Méchin, C. Caillaud, J. Troles, B. Luther-Davies, and O. Bang, "Multi-milliwatt mid-infrared supercontinuum generation in a suspended core chalcogenide fiber," *Opt. Express*, vol. 23, no. 3, pp. 3282–3291, Feb 2015. [Online]. Available: http://www.opticsexpress.org/abstract.cfm?URI=oe-23-3-3282

[22] Y. Yu, B. Zhang, X. Gai, C. Zhai, S. Qi, W. Guo, Z. Yang, R. Wang, D.-Y. Choi, S. Madden, and B. Luther-Davies, "1.8-10μm mid-infrared supercontinuum generated in a step-index chalcogenide fiber using low peak pump power," *Opt. Lett.*, vol. 40, no. 6, pp. 1081–1084, Mar 2015. [Online]. Available: http://ol.osa.org/abstract.cfm?URI=ol-40-6-1081

[23] A. B. Seddon, Z. Tang, D. Furniss, S. Sujecki, and T. M. Benson, "Progress in rare-earth-doped mid-infrared fiber lasers," *Optics Express*, vol. 18, no. 25, pp. 26 704–26 719, 2010. [Online]. Available: http://www.opticsexpress.org/abstract.cfm?URI=oe-18-25-26704

[24] H.-J. Stöckmann and J. Stein, "Quantum chaos in billiards studied by microwave absorption," *Phys. Rev. Lett.*, vol. 64, pp. 2215–2218, May 1990. [Online]. Available: https://link.aps.org/doi/10.1103/PhysRevLett.64.2215

[25] E. J. Heller, "Wavepacket dynamics and quantum chaology," *Session LII-Chaos and quantum physics (Les Houches, France, 1989)*, 1991.

[26] M. C. Gutzwiller, "Resource letter ICQM-1: The interplay between classical and quantum mechanics," *American Journal of Physics*, vol. 66, no. 4, pp. 304–324, 1998. [Online]. Available: https://doi.org/10.1119/1.19065

[27] B. Eckhardt, "Periodic Orbit Theory," in *Nonlinear Sciences - Chaotic Dynamics eprint arXiv:chao-dyn/9303015*, 1993.

[28] E. P. Wigner, "Characteristics vectors of bordered matrices with infinite dimensions II," *Annals of Mathematics*, vol. 65, no. 2, pp. 203–207, 1957.

[29] M. J. Giannoni, A. Voros, and J. Zinn-Justin, "Chaos and quantum physics," *Les Houches, Session LII (North-Holland, Amsterdam, 1991)*, 1989.

[30] F. L. Moore, J. C. Robinson, C. Bharucha, P. E. Williams, and M. G. Raizen, "Observation of dynamical localization in atomic momentum transfer: A new testing ground for quantum chaos," *Phys. Rev. Lett.*, vol. 73, pp. 2974–2977, Nov 1994. [Online]. Available: https://link.aps.org/doi/10.1103/PhysRevLett.73.2974

[31] T. Rees, "Chladni plates: The first step towards visualising sound," *Explore Whipple Collections, Whipple Museum of the History of Science*, 2009. [Online]. Available: http://www.hps.cam.ac.uk/whipple/explore/acoustics/ernstchladni/chladniplates/

[32] J. U. Nöckel, A. D. Stone, and R. K. Chang, "Q spoiling and directionality in deformed ring cavities," *Opt. Lett.*, vol. 19, no. 21, pp. 1693–1695, Nov 1994. [Online]. Available: http://ol.osa.org/abstract.cfm?URI=ol-19-21-1693

[33] G. E. Mitchell, A. Richter, and H. A. Weidenmüller, "Random matrices and chaos in nuclear physics: Nuclear reactions," *Rev. Mod. Phys.*, vol. 82, pp. 2845–2901, Oct 2010. [Online]. Available: https://link.aps.org/doi/10.1103/RevModPhys.82.2845

[34] L. P. Kouwenhoven, C. M. Marcus, P. L. McEuen, S. Tarucha, R. M. Westervelt, and N. S. Wingreen, *Electron Transport in Quantum Dots*. Dordrecht: Springer Netherlands, 1997.

[35] M. Lakshmanan and K. Ganesan, "Rydberg atoms and molecules testing grounds for quantum manifestations of chaos," *Current Science*, vol. 68, no. 1, pp. 38–44, 1995. [Online]. Available: http://www.jstor.org/stable/24096169

[36] C. F. Bharucha, J. C. Robinson, F. L. Moore, B. Sundaram, Q. Niu, and M. G. Raizen, "Dynamical localization of ultracold sodium atoms," *Phys. Rev. E*, vol. 60, pp. 3881–3895, Oct 1999. [Online]. Available: https://link.aps.org/doi/10.1103/PhysRevE.60.3881

[37] J. de Rosny, A. Tourin, and M. Fink, "Coherent backscattering of an elastic wave in a chaotic cavity," *Phys. Rev. Lett.*, vol. 84, pp. 1693–1695, Feb 2000. [Online]. Available: https://link.aps.org/doi/10.1103/PhysRevLett.84.1693

[38] A. Richter, *Playing Billiards with Microwaves — Quantum Manifestations of Classical Chaos*, D. A. Hejhal, J. Friedman, M. C. Gutzwiller, and A. M. Odlyzko, Eds. New York, NY: Springer New York, 1999.

[39] A. Kudrolli, M. C. Abraham, and J. P. Gollub, "Scarred patterns in surface waves," *Phys. Rev. E*, vol. 63, p. 026208, Jan 2001. [Online]. Available: https://link.aps.org/doi/10.1103/PhysRevE.63.026208

[40] R. L. Weaver and O. I. Lobkis, "Ultrasonics without a source: Thermal fluctuation correlations at mhz frequencies," *Phys. Rev. Lett.*, vol. 87, p. 134301, Sep 2001. [Online]. Available: https://link.aps.org/doi/10.1103/PhysRevLett.87.134301

[41] K. J. Vahala, "Optical microcavities." *Nature*, vol. 424, no. 6950, pp. 839–846, 2003.

[42] J. U. Noeckel and A. D. Stone, "Ray and wave chaos in asymmetric resonant optical cavities," *Nature*, vol. 45, p. 4, 1998. [Online]. Available: http://arxiv.org/abs/chao-dyn/9806017

[43] G. Casati, B. V. Chirikov, I. Guarneri, and D. L. Shepelyansky, "Dynamical stability of quantum "chaotic" motion in a hydrogen atom," *Phys. Rev. Lett.*, vol. 56, pp. 2437–2440, Jun 1986. [Online]. Available: https://link.aps.org/doi/10.1103/PhysRevLett.56.2437

[44] C. Gmachl, F. Capasso, E. E. Narimanov, J. U. Noeckel, A. D. Stone, J. Faist, D. L. Sivco, and A. Y. Cho, "High-power directional emission from microlasers with chaotic resonators," *Science*, vol. 5, no. 1998, pp. 1556–1564, 1998. [Online]. Available: http://arxiv.org/abs/cond-mat/9806183

[45] J. U. Nöckel, A. D. Stone, G. Chen, H. L. Grossman, and R. K. Chang, "Directional emission from asymmetric resonant cavities," *Optics Letters*, vol. 21, no. 19, p. 1609, oct 1996. [Online]. Available: https://www.osapublishing.org/abstract.cfm?URI=ol-21-19-1609

[46] A. Mekis, J. U. Nöckel, G. Chen, A. D. Stone, and R. K. Chang, "Ray chaos and Q spoiling in lasing droplets," *Phys. Rev. Lett.*, vol. 75, pp. 2682–2685, Oct 1995. [Online]. Available: https://link.aps.org/doi/10.1103/PhysRevLett.75.2682

[47] W. F. Brinkman, T. L. Koch, D. V. Lang, and D. P. Wilt, "The lasers behind the communications revolution," *Bell Labs Technical Journal*, vol. 5, no. 1, pp. 150–167, 2002. [Online]. Available: http://ieeexplore.ieee.org/lpdocs/epic03/wrapper.htm?arnumber=6770546

[48] S. Boriskina and A. Nosich, "Radiation and absorption losses of the whispering-gallery-mode\dielectric resonators excited by a dielectric waveguide," *IEEE Transactions on Microwave Theory and Techniques*, vol. 47, no. 2, pp. 224–231, 1999.

[49] S. V. Boriskina, T. M. Benson, P. Sewell, and A. I. Nosich, "Tuning of elliptic Whispering-Gallery-Mode microdisk waveguide filters," *Journal of Lightwave Technology*, vol. 21, no. 9, pp. 1987–1995, 2003.

[50] V. Doya, O. Legrand, and F. Mortessagne, "Optimized absorption in a chaotic double-clad fiber amplifier." *Optics letters*, vol. 26, no. 12, pp. 872–874, 2001.

[51] P. Leproux, S. Février, V. Doya, P. Roy, and D. Pagnoux, "Modeling and pptimization of double-dlad fiber amplifiers using chaotic propagation of the pump," *Optical Fiber Technology*, vol. 7, no. 4, pp. 324–339, 2001. [Online]. Available: http://linkinghub.elsevier.com/retrieve/pii/S106852000190361X

[52] L. Philippe, V. Doya, R. Philippe, P. Dominique, M. Fabrice, and L. Olivier, "Experimental study of pump power absorption along rare-earth-doped double clad optical fibres," *Optics Communications*, vol. 218, no. 4-6, pp. 249–254, 2003.

[53] D. Kouznetsov, J. V. Moloney, and E. M. Wright, "Efficiency of pump absorption in double-clad fiber amplifiers. I. Fiber with circular symmetry," *J. Opt. Soc. Am. B*, vol. 18, no. 6, pp. 743–749, Jun 2001. [Online]. Available: http://josab.osa.org/abstract.cfm?URI=josab-18-6-743

[54] D. Kouznetsov and J. V. Moloney, "Efficiency of pump absorption in double-clad fiber amplifiers. II. Broken circular symmetry," *J. Opt. Soc. Am. B*, vol. 19, no. 6, pp. 1259–1263, Jun 2002. [Online]. Available: http://josab.osa.org/abstract.cfm?URI=josab-19-6-1259

[55] E. Snitzer, H. Po, F. Hakimi, R. Tumminelli, and B. McCollum, "Double clad, offset core Nd fiber laser," *Optical Fiber Sensors*, p. PD5, 1988. [Online]. Available: http://www.osapublishing.org/abstract.cfm?URI=OFS-1988-PD5

[56] M. V. Berry, "Regular and irregular semiclassical wavefunctions," *Journal of Physics A: Mathematical and General*, vol. 10, no. 12, p. 2083, 1977. [Online]. Available: http://stacks.iop.org/0305-4470/10/i=12/a=016

[57] E. J. Heller, "Bound-state eigenfunctions of classically chaotic Hamiltonian systems: Scars of periodic orbits," *Physical Review Letters*, vol. 53, no. 16, pp. 1515–1518, 1984.

[58] H. Waalkens, J. Wiersig, and H. R. Dullin, "Elliptic quantum billiard," *Annals of Physics*, vol. 260, no. 1, pp. 50 – 90, 1997. [Online]. Available: http://www.sciencedirect.com/science/article/pii/S0003491697957158

[59] J. P. Bird, R. Akis, D. K. Ferry, J. Cooper, K. Ishibashi, Y. Ochiai, Y. Aoyagi, and T. Sugano, "Intrinsic stable orbits in open quantum dots," *Semiconductor Science and Technology*, vol. 13, no. 8A, pp. A4–A6, 1998.

[60] I. V. Zozoulenko and K.-F. Berggren, "Quantum scattering, resonant states, and conductance fluctuations in an open square electron billiard," *Phys. Rev. B*, vol. 56, pp. 6931–6941, Sep 1997. [Online]. Available: https://link.aps.org/doi/10.1103/PhysRevB.56.6931

[61] R. V. Jensen, M. M. Sanders, M. Saraceno, and B. Sundaram, "Inhibition of quantum transport due to "scars" of unstable periodic orbits," *Phys. Rev. Lett.*, vol. 63, pp. 2771–2775, Dec 1989. [Online]. Available: https://link.aps.org/doi/10.1103/PhysRevLett.63.2771

[62] C. Michel, V. Doya, O. Legrand, and F. Mortessagne, "Selective amplification of scars in a chaotic optical fiber," *Physical Review Letters*, vol. 99, no. 22, pp. 1–4, 2007.

[63] C. Michel, S. Tascu, V. Doya, O. Legrand, and F. Mortessagne, "Gain-controlled wave chaos in a chaotic optical fiber," *Journal of the European Optical Society: Rapid Publications*, vol. 4, p. 09020, 2009. [Online]. Available: https://hal.archives-ouvertes.fr/hal-00433001

[64] C. Michel, V. Doya, S. Tascu, W. Blanc, O. Legrand, and F. Mortessagne, "Controlled excitation of scar modes in passive and active multimode chaotic fiber," *Appl. Opt.*, vol. 48, no. 31, pp. G163–G168, Nov 2009. [Online]. Available: http://ao.osa.org/abstract.cfm?URI=ao-48-31-G163

[65] C. Michel, M. Allgaier, and V. Doya, "Regular modes in a mixed-dynamics-based optical fiber," *Phys. Rev. E*, vol. 93, p. 022201, Feb 2016. [Online]. Available: https://link.aps.org/doi/10.1103/PhysRevE.93.022201

[66] M. Brin and G. Stuck, *Introduction to dynamical systems*. Cambridge: Cambridge Univ. Press, 2002. [Online]. Available: http://cds.cern.ch/record/712862

[67] S. Ulam, " A Collection of Mathematical Problems, In: Interscience Tracts in Pure and Applied Mathematics," *Interscience, New York*, p. 73, 1960.

[68] O. Perron, "Zur theorie der matrices," *Mathematische Annalen*, vol. 64, no. 2, pp. 248–263, Jun 1907. [Online]. Available: https://doi.org/10.1007/BF01449896

[69] K. M. Frahm and D. L. Shepelyansky, "Ulam method for the Chirikov standard map," *European Physical Journal B*, vol. 76, no. 1, pp. 57–68, 2010.

[70] G. Froyland, "Ulam's method for random interval maps," *Nonlinearity*, vol. 12, no. 4, pp. 1029–1051, 1999. [Online]. Available: http://stacks.iop.org/0951-7715/12/i=4/a=318?key=crossref.62ac9ead490dea61e597ab351ac48aea

[71] L. Ermann and D. L. Shepelyansky, "The Arnold cat map, the Ulam method and time reversal," *Physica D: Nonlinear Phenomena*, vol. 241, no. 5, pp. 514–518, 2012.

[72] A. Lasota, J. A. Yorke, M. Society, and V. Dec, "On the Existence of Invariant Measures for Piecewise Monotonic Transformations," *Transactions of the American Mathematical Society*, vol. 186, pp. 481–488, 1973.

[73] P. Szépfalusy and T. Tél, "New approach to the problem of chaotic repellers," *Physical Review A*, vol. 34, no. 3, pp. 2520–2523, 1986.

[74] J. Ding, Q. Du, and T. Y. Li, "The spectral analysis of Frobenius-Perron Operators," *Journal of Mathematical Analysis and Applications*, pp. 285–301, 1993.

[75] J. Ding and A. Zhou, "Finite approximations of Frobenius-Perron operators: A solution of Ulam's conjecture to multi-dimensional transformations," *Physica D: Nonlinear Phenomena*, vol. 92, no. 1-2, pp. 61–68, 1996.

[76] J. Ding, T. Y. Li, and A. Zhou, "Finite approximations of Markov operators," *Journal of Computational and Applied Mathematics*, vol. 147, no. 1, pp. 137–152, 2002.

[77] T. Y. Li, "Finite approximation for the Frobenius-Perron operator. A solution to Ulam's conjecture," *Journal of Approximation Theory*, vol. 17, no. 2, pp. 177–186, 1976.

[78] Z. Kovács and T. Tél, "Scaling in multifractals: Discretization of an eigenvalue problem," *Phys. Rev. A*, vol. 40, pp. 4641–4646, Oct 1989. [Online]. Available: https://link.aps.org/doi/10.1103/PhysRevA.40.4641

[79] J. Weber, F. Haake, P. A. Braun, C. Manderfeld, and P. Seba, "Resonances of the Frobenius-Perron operator for a Hamiltonian map with a mixed phase space," *Journal of Physics A: Mathematical and General*, vol. 34, no. 36, p. 7195, 2001. [Online]. Available: http://stacks.iop.org/0305-4470/34/i=36/a=306

[80] J. Kullig and J. Wiersig, "Frobenius-Perron eigenstates in deformed microdisk cavities: Non-Hermitian physics and asymmetric backscattering in ray dynamics," *New Journal of Physics*, vol. 18, no. 1, p. 15005, 2016. [Online]. Available: http://dx.doi.org/10.1088/1367-2630/18/1/015005

[81] E. G. Altmann and T. Tél, "Poincaré recurrences from the perspective of transient chaos," *Physical Review Letters*, vol. 100, no. 17, pp. 2–5, 2008.

[82] G. D. Birkhoff, "On the periodic motions of dynamical systems," *Acta Math.*, vol. 50, pp. 359–379, 1927. [Online]. Available: https://doi.org/10.1007/BF02421325

[83] H. Tureci, H. Schwefel, a. Stone, and E. Narimanov, "Gaussian-optical approach to stable periodic orbit resonances of partially chaotic dielectric micro-cavities." *Optics express*, vol. 10, no. 16, pp. 752–776, 2002.

[84] H. Türeci, H. Schwefel, P. Jacquod, and A. D. Stone, "Modes of wave-chaotic dielectric resonators," in *Progress in Optics*, 2005, vol. 47, pp. 75–137. [Online]. Available: http://linkinghub.elsevier.com/retrieve/pii/S007966380547002X

[85] G. D. Chern, H. E. Tureci, A. D. Stone, R. K. Chang, M. Kneissl, and N. M. Johnson, "Unidirectional lasing from InGaN multiple-quantum-well spiral-shaped micropillars," *Applied Physics Letters*, vol. 83, no. 9, pp. 1710–1712, 2003.

[86] H. G. L. Schwefel, H. E. Tureci, A. D. Stone, and R. K. Chang, "Progress in asymmetric resonant cavities: using shape as a design parameter in dielectric microcavity lasers," *Optical Microcavities*, pp. 415–495, 2004.

[87] *Markov Chains*. Retrieved February 14, 2019. [Online]. Available: https://brilliant.org/wiki/markov-chains/

[88] N. A. Mortensen, "Air-clad fibers: pump absorption assisted by chaotic wave dynamics?" *Opt. Express*, vol. 15, no. 14, pp. 8988–8996, Jul 2007. [Online]. Available: http://www.opticsexpress.org/abstract.cfm?URI=oe-15-14-8988